A DIAGNOSTIC IMAGING TECHNIQUE FOR IDENTIFICATION OF STRUCTURAL DAMAGE USING HYBRID FEATURES OF LAMB WAVE SIGNALS

ZHOU CHAO

Ph.D

The Hong Kong Polytechnic University

2011

The Hong Kong Polytechnic University

Department of Mechanical Engineering

A Diagnostic Imaging Technique for Identification of Structural Damage Using Hybrid Features of Lamb Wave Signals

ZHOU Chao

A thesis submitted in partial fulfilment of the requirements for the degree of Doctor of Philosophy

January 2011

CERTIFICATE OF ORIGINALITY

I hereby declare that this thesis is my own work and that, to the best of my knowledge and belief, it reproduces no material previously published or written, nor material that has been accepted for the award of any other degree or diploma, except where due acknowledgement has been made in the text.

_____ _____ (Signature)

_____ Chao ZHOU_____ (Name of student)

ABSTRACT

Diagnostic imaging using Lamb waves, such as Lamb wave tomography, has been attracting increasing preference because it yields an easily interpretable and intuitional quantitative map concerning the overall 'health' state of the structure under inspection. It is however envisaged that to construct a tomogram is often at the expenses of using a large number of sensors to scan the entire area carefully, therefore limiting its application for online structural health monitoring (SHM). To enhance the practicality of Lamb-wave-based SHM in conjunction with use of imaging techniques, alternative methods have been actively explored, exemplified by a recent technical breakthrough: probability-based diagnostic imaging (PDI). A PDI method attempts to describe a damage event using a binary grey-scale image. The field value at a particular pixel of the image is linked with the probability of damage presence at the spatial point of the monitored structure that corresponds to this pixel. Presenting damage in terms of its presence probability is an improvement over traditional nondestructive evaluation (NDE) or SHM which has an ultimate goal to define damage with deterministic parameters (*e.g.*, location coordinates, size or length). That is because the underlying concept of '*probability*' is more consistent with the implication of '*predicting*' or '*estimating*' damage. Nevertheless majority of the current PDI approaches, substantially based on canvassing changes in temporal information such as time-of-flights (ToFs) extracted from captured wave signals, fail to portray damage quantitatively including its orientation, shape and size, because difference in damage orientation, shape and size would not lead to pronounced changes in temporal information.

In addition, when dealing with orientation-specific or sharp-angled damage featuring a dominant size in a particular dimension (*e.g.*, a crack or a notch), a challenging issue is that such sort of damage often exerts strong directivity to wave propagation. As a result, information associated with damage may not be efficiently extracted from signals captured by sensors at certain locations, in the absence of prior knowledge of damage shape. Further down to a fine level, the periphery of structural damage such as delamination can be described as the continuum of a number of cracks with various lengths which shape the damage, although macroscopically the damage often presents relatively smooth boundaries. That implies ascertainment of orientation of individual cracks can facilitate depiction of damage shape and further severity. The effectiveness of most existing damage identification approaches has been verified by identifying singular damage in a structure. However, in practice an engineering structure is likely to evidence multiple instances of damage simultaneously. Rather than being a simple expansion from the approaches developed for singular damage, qualitative or quantitative identification of multiple damages is another tanglesome issue.

In this thesis work, a novel PDI approach was developed with an aim to circumvent the above-addressed deficiencies of current NDE and SHM. Systematic investigations were divided into the following three parts:

First, three fundamental issues relevant to Lamb-wave-based-PDI were interrogated: a) effect of the orientation of damage with sizable length in a particular dimension (orientation-specific damage) on Lamb wave propagation, b) attenuation of Lamb wave as propagation and its compensation, and c) influential area of damage on wave

sensing path. Both finite element (FE) simulation and experimental validation were conducted and results were compared. Results arising from these fundamental studies served as the knowledge basis to develop PDI approach in this study.

Second, based on the correlations established in the above fundamental studies between (1) damage location and ToFs extracted from signals, and (2) intensity of signal energy scattered by damage and damage orientation, a PDI approach was developed, in conjunction with use of an active sensor network in conformity to a pulse-echo configuration. Relying on signal features including both the temporal information and signal intensity, and with the assistance of a two-level synthetic image fusion scheme, such an imaging approach was capable of indicating clearly the orientation of individual damage edges and further the shape of damage. The effectiveness of this approach was demonstrated by predicting selected orientation-specific damage including a triangular through-thickness hole (through FE simulation) and a through-thickness crack (through experiment) in aluminium plates. Nevertheless, as observed, when applied to detection of damage consisting of multiple edges of different orientations, this approach became unwieldy.

Last, to overcome the deficiency of the above PDI approach using sole pulse-echo configuration (*e.g.* not capable of depicting damage of different orientations), improvement was made using hybrid signal features extracted from both the pulse-echo and pitch-catch configurations in the active sensor network. To supplement the possible insufficiency of signal features for high-precision identification, a novel concept of '*virtual sensing*' was established, facilitating extraction of rich signal features. A hybrid image fusion scheme was developed, able to enhance the tolerance

of the PDI approach to measurement noise and possible erroneous perceptions from individual sensing paths. The approach was validated by predicting representative damage scenarios including L-shape through-thickness crack (strong orientation-specific damage), polygonal damage (multi-edge damage) and multi-damage in aluminium plates.

Accurate identification results for typical damage cases have demonstrated the effectiveness of the developed PDI approaches in quantitatively visualising structural damage, regardless of its shape and number, by highlighting its individual edges in an easily interpretable binary image.

LIST OF PUBLICATIONS

Refereed Journal Papers

1. **Zhou, C.**, Su, Z. and Cheng, L. 2011. 'Quantitative evaluation of orientation-specific damage using elastic waves and probability-based diagnostic imaging', *Mechanical Systems and Signal Processing*, (**in press**).

2. **Zhou, C.**, Su, Z. and Cheng, L. 2010. 'Probability-based diagnostic imaging (PDI) using hybrid features extracted from ultrasonic Lamb wave signals', *Smart Materials and Structures* (submitted).

3. Su, Z., Cheng, L., Wang, X., Yu, L. and **Zhou, C**. 2009. 'Predicting delamination of composite laminates using an imaging approach', *Smart Materials and Structures*, **18**(7):074002 (8pp).

Refereed International Conference Papers

4. **Zhou, C.**, Su, Z. and Cheng, L. 'Characterising fatigue crack in an aluminium plate using guided elastic waves', in *Proceedings of SPIE Conference on Smart Structures/NDE (Sensors and Smart Structures Technologies for Civil, Mechanical and Aerospace Systems (Conference 7981))*, Mar. 2011, San Diego, CA., USA.

5. **Zhou, C.**, Su, Z. and Cheng, L. 'Damage characterisation using pulse-echo and pitch-catch active sensor network', in *Proceedings of the 3rd Asia Pacific Workshop on Structural Health Monitoring*, Nov. 2010, Komaba, Meguro-ku, Tokyo, Japan.

6. **Zhou, C.**, Su, Z. and Cheng, L. 'A probability-based diagnostic imaging approach using an active sensor network based on hybrid pulse-echo and pitch-catch configurations', in *Proceedings of the 5th European Workshop on Structural Health Monitoring*, Jun. 2010, Sorrento, Naples, Italy.

7. **Zhou, C.**, Su, Z. and Cheng, L. 'Quantifying orientation-specific damage using diagnostic imaging', in *Proceedings of the 7th International Workshop on Structural Health Monitoring*, Sept. 2009, Stanford, CA., USA.

ACKNOWLEDGMENT

First and foremost, I owe my deepest gratitude to my supervisors, Prof. Li CHENG and Dr. Zhongqing SU, who have provided me with most valuable guidance in every stage of my postgraduate study. No matter what difficulties I have met, they never hesitated to give me strongest support, which really means a lot to me. Their unassuming, meticulous and rigorous scholarship enlightens me a lot in the development of my future career.

During my study in the Department of Mechanical Engineering (ME), the Hong Kong Polytechnic University (HK POLYU), it is very lucky for me to work with many nice people. My sincere gratitude is given to all of them. Particular thanks go to Mr. Jiangang Chen, Mr. Hao Xu, Dr. Long Yu, Dr. Rongping Fan, Mr. Zhenbo Lu, Mr. Zhengang Liu, who have provided me with valuable assistance in the whole process of my study.

Last but not least, I would like to thank my parents and my wife for their greatest support all the time. It is their self-giving love that encourages me eternally.

TABLE OF CONTENTS

LIST OF FIGURES

LIST OF TABLES

NOMENCLATURE

General Symbols

S_0	Fundamental symmetric Lamb wave mode
A_0	Fundamental anti-symmetric Lamb wave mode
S_i	Symmetric Lamb modes (*i*=0, I, II, III, *etc.*)
A_i	Anti-symmetric Lamb modes (*i*=0, I, II, III, *etc.*)
μ	Shear modulus
λ	Lamé constant
ν	Poisson's ratio
ρ	Mass density
ϕ	Scalar potential
ψ	Vector potential
c_L	Velocity of longitudinal wave
c_T	Velocity of shear wave
ω	Circular frequency
k	Wavenumber
λ_{wave}	Wavelength
c_p	Phase velocity
c_g	Group velocity
$f(t)$	Time domain signal

$H(t)$	Hilbert transform of $f(t)$
$F(\omega)$	Fourier transform of $f(t)$
$W(a,b)$	Wavelet coefficient at scale a and translational value b
ρ_{XY}	Correlation coefficient between *X* and *Y*
C_{XY}	Covariance of *X* and *Y*
Ξ	Intensity of signal energy
$I(x_m, y_n)$	Field value at pixel (x_m , y_n)
σ	Standard deviation
η	Mean
θ	Angle of wave incidence
$I_i'\big\vert_I$	Source image established using first genre of field value
$I_i\big\vert_{II}$	Source image established using second genre of field value

Abbreviations

NDE:	Nondestructive evaluation
SHM:	Structural health monitoring
PZT:	Piezoelectric lead zirconate titanate
PVDF:	Polyvinylidene fluoride
MFC:	Macro fibre composite
FBG:	Fibre Bragg gratings
2D:	Two-dimensional
3D:	Three-dimensional
HT:	Hilbert transform

FT:	Fourier transform
FFT:	Fast Fourier transform
STFT:	Short-time Fourier transform
WT:	Wavelet transform
CWT:	Continuous wavelet transform
DWT:	Discrete wavelet transform
ToF:	Time-of-flight
PDI:	Probability-based diagnostic imaging
SNR:	Signal-to-noise ratio
FE:	Finite element
DI:	Damage index

CHAPTER 1 Introduction

1.1 Research Background

Many industrial assets including aircraft, civil infrastructure and pressure vessels serve in adverse working conditions and thus are prone to various types of damage such as cracks and corrosion in metallic structures or delamination in composite laminates. The presence of damage can significantly impair the structural integrity, jeopardise the operational efficiency, and potentially lead to catastrophic failure of these structures. As a miserable example, a China Airlines Boeing 747 experienced a mid-air disintegration and crashed into the ocean near Penghu Islands in Taiwan strait on 25 May 2002, killing all 225 people on board. The investigation report attributes this accident to the metal fatigue damage. Working in very harsh flight environment with large variations in pressure, speed and loading conditions, the fatigue crack in tail of the airframe, initially small in size, started developing and finally causing the crash of the plane. Another tragedy due to structural damage is the disintegration of Columbia Shuttle on 1 February 2003. According to NASA's investigation report, the

cause of this accident was an impact puncture sustained in the leading edge of the left wing introduced during the launch of the shuttle. The impact puncture impaired Columbia's thermal protection system, and during re-entry, high temperature atmosphere pierced into the shuttle and finally incurred the disaster. Similar tragedies befall every year, causing vast money loss and even depriving numerous lives.

With safety being the paramount priority for all engineering structures, reliability, integrity and durability criteria must be strictly met. Such requirement has motivated intensive research activities towards the development of nondestructive evaluation (NDE) and structural health monitoring (SHM) techniques, aimed at detecting structural damage in its initial forming stage and thus providing early warning before the damage jeopardises the safety of the structures.

1.1.1 Nondestructive Evaluation (NDE)

NDE refers to a wide range of techniques applied to evaluate possible damage in a certain engineering structure or asset nondestructively. Upon intensive research over half a century, NDE is becoming a mature technology field and playing an important role in maintaining structural integrity and enhancing system safety in various application areas such as mechanical engineering, civil engineering, electrical engineering, medicine, *etc*..

There is a large variety of NDE techniques, most typified by ultrasonic scanning [1-4], eddy current [5-9], radiography [10-13], infrared thermography [14, 15], shearography [16], dye penetrant testing [17], magnetic resonance imagery [18] and acoustic holography [19], *etc.*. Amongst these methods, several representative techniques were reviewed as follows:

Ultrasonic scanning, as one of the most versatile NDE techniques, is applied to test a variety of materials, *e.g.* metals, composites, concrete, and woods [1-4]. In ultrasonic scanning, ultrasonic elastic waves in the ultrasonic frequency range are emitted to interrogate a test specimen. The presence of flaws in the specimen can modulate the ultrasonic wave field, accompanied by wave reflection, scattering and mode conversion, and this serves as the premise of ultrasonic wave-based damage detection. Generally, ultrasonic probes are used to generate and acquire ultrasonic waves, as typified by wedge, comb, and Hertzian contact probes (Fig. 1.1). To inject ultrasound into the specimen, a couplant is often required to obtain a good coupling between probes and the test specimen since ultrasonic waves could hardly transmit through air. Integration of transition media (couplant) may affect operational efficiency. Accordingly, innovative probes operating in a non-contact mode have been developed, including air-coupled transducers, electromagnetic acoustic transducers (EMAT), and laser induced ultrasound [20-22]. In brief, ultrasonic scanning is accurate, safe, and highly sensitive to different types of flaws, although there are several limitations in

applications such as time-consuming (the probes have to be moved back and forth alone the specimen surface) and removal of parts from a main structure for probe accessing.

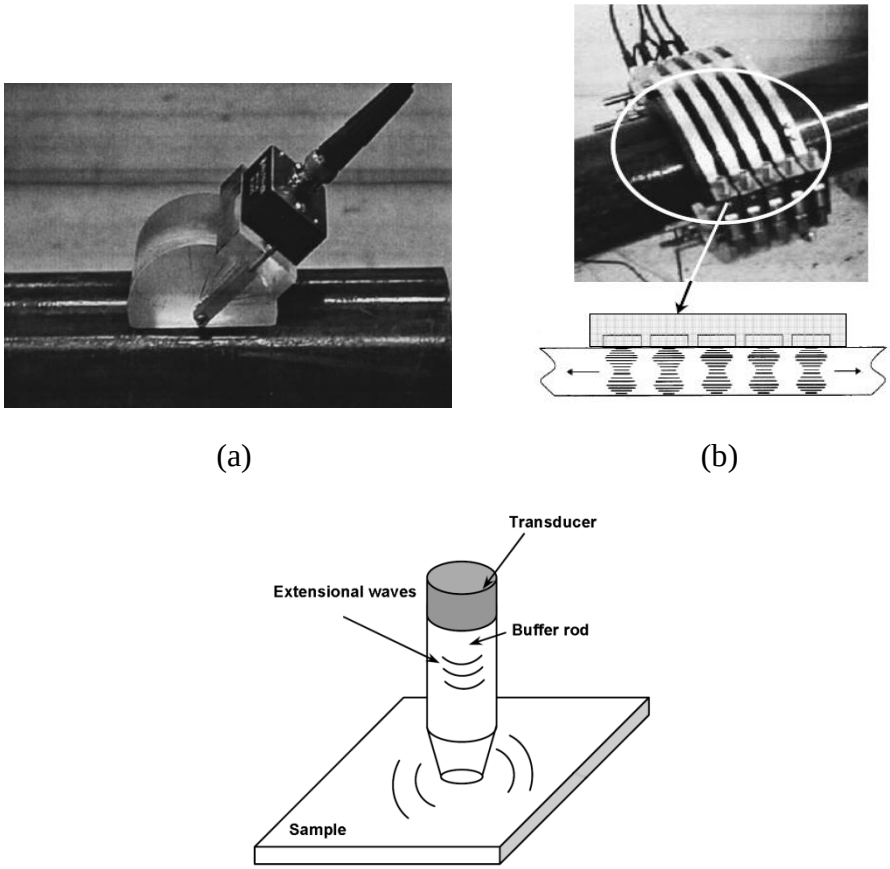

(a) (b)

(c)

Fig. 1.1. Typical ultrasonic probes: (a) perspex wedge-coupled angle adjustable ultrasonic probe; (b) comb ultrasonic probe; and (c) Hertzian contact probe [1, 2]

Eddy current [5-9] works in such a way that when a changing magnetic field is imposed to a specimen under inspection which is conductive, eddy currents, *i.e.* circulating flow of currents, will be produced inside the specimen, in accordance with electromagnetic induction. The presence of any damage can result in variations in the

electrical conductivity or magnetic permeability of the specimen, thus giving rise to a change in the eddy current flow, which can inversely be utilised for damage detection. Eddy current testing presents prominent performance for crack detection. Nevertheless, only conductive materials can be inspected with this method.

Radiography, using radial rays such as X-ray is widely used in medicine and engineering [10-13]. X-rays, as a type of electromagnetic radiation with high energy, can penetrate into a variety of materials. During inspection, X-rays from a generator is projected into a test specimen. A portion of X-rays is absorbed by the specimen, while the remaining portion passes through and is acquired by a detector. By virtue of X-ray absorptivity of different transects, abnormality inside the specimen can be identified. Radiography can provide an intuitive and accurate image for damage interpretation. But strong radiation is hazardous to the operators and may limit its applications.

Thermography and shearography are relatively new NDE techniques [14-16]. Thermography is to inspect materials, structures or systems by means of mapping of thermal patterns at their surfaces. The presence of flaws can affect thermal conductivity, emissivity or impedance of a test specimen, therefore resulting in variations in thermal patterns. Merits of thermography include contactless, fast, safe and sensitive to different damage types such as corrosion. Shearography, an optical method, uses a laser interferometric system to measure out-of-plane deformation of a test specimen under

a small amount of load. Abnormality in the specimen can cause stress concentration and result in unique deformation, which can inversely be utilized for damage identification. Shearography has been attracting increasing attention in recent years due to the outstanding capability to inspect a large area in a relatively short time.

NDE techniques are of increasing importance in terms of system reliability, integrity and efficiency. Nevertheless, there still exist some limitations of traditional NDE techniques. Most prominently, NDE techniques require downtime to conduct regular scheduled test, and cannot operate when the inspected structure is in its normal service. They may even require disassembly of the part to be inspected from main system, which is costly and may be impractical in some cases. Therefore, sole application of traditional NDE techniques is under challenge for detection of structural damage in a fast and efficient manner.

1.1.2 Structural Health Monitoring

Envisaging the above deficiencies of traditional NDE techniques, structural health monitoring (SHM) has emerged as a new technological breakthrough to revamp conventional NDE philosophy, motivated by the rapid development of sensor technology, electronics, signal processing, manufacturing, electronic packaging, material science and applied mechanics. Unlike conventional NDE techniques which

require downtime of the structure or system under inspection for regular scheduled inspection, a SHM technique uses permanently installed sensors for real-time surveillance of the overall health status of a structure. Successful implementation of such a technique can substantially enhance operational efficiency of an engineering system, drive down maintenance costs, improve safety and reliability, and extend the residual lifespan of aged structures.

Intensive research and development activities have been directed to the field of SHM [23-28]. Representatively, Ihn and Chang [23] developed an elastic-wave-based diagnostic approach for on-line health monitoring of fatigue crack growth. Giurgiutiu *et al.* [24] applied piezoelectric wafer active sensors for health monitoring of aging aircraft panels in light of electro-mechanical impedance and elastic wave propagation techniques. Sohn *et al.* [25] proposed a reference-free structural health monitoring technique on the concept of time reversal acoustics. Due to the extensive research work, some of the developed diagnostic techniques have been commercialised and put into real engineering applications. As a typical example, Boeing Corporation developed a Structural Usage Monitoring System (SUMS) for inspecting critical parts on MH-47E helicopter including bearing, rotor shafts, bolts *etc.* The SUMS can evaluate current health status of the helicopter and further predict the remaining useful life of concerned parts [26]. Iglesias and Palomino [27] discussed the health monitoring system applied in Euro-fighter-18. The health monitoring system conducted onboard measurements of

crucial information such as strain, acceleration, air speed and roll rate. Crucial information was processed, analysed, and finally used to predict the remaining fatigue life of the aircraft. Apart from various mechanical structures, SHM has been applied in civil infrastructures, one typical example as wind and structural health monitoring system for bridges in Hong Kong (WASHMS) [28]. The WASHMS has employed approximately 900 sensors including strain gauges, accelerometers, displacement transducers, temperature sensors, anemometers and level sensing stations to monitor the working condition and health status of bridges across Hong Kong including the Tsing Ma, Ting Kau and Kap Shui Mun bridges. WASHMS, as an integrated system consisting of sensory systems, data acquisition systems, local and global computer systems, can provide early warning and ensure the safety and comfort of bridge users.

A SHM system usually involves a sensory system, a data acquisition system, a data management and interpretation system [28]. The critical elements for a sensory system are transducers broadly including both actuators and sensors. To satisfy SHM applications, transducers in a sensor system should ideally be a part of the structure under inspection. This poses additional requirement on transducers: an ideal transducer for SHM should be small in size and light in weight, and easily to be embedded into or surface-mounted onto the structure. In this aspect, piezoelectric wafers and optic fibres are two kinds of transducers widely used for developing sensory systems for SHM (to be detailed in Section 1.2.2). Small and light, a piezoelectric wafer can has wide

frequency responses with low power consumption and cost (for example, for a piezoelectric wafer measuring 7 mm × 7 mm × 0.2 mm, it weighs less than 70 mg and costs US$ 15, contrasting to a conventional NDE ultrasound wedge probe weighing 25 g, measuring 40 mm × 30 mm × 40 mm and costing US$ 400 [29]). Piezoelectric wafers are very suitable for integration into host structures, serving as good candidates for build-in actuators and sensors in a sensory system. On the other hand, optic fibres feature wide bandwidth, good compatibility, immunity to electromagnetic interference, long service life, low power consumption, and in particular light weight and tiny volume [30, 31]. All of these features also make optic fibres suitable for SHM purposes.

A number of mechanisms can be utilised to develop various SHM techniques, as typified by static-parameter-based, vibration-based and elastic-wave-based SHM [32-37]. The basics of these techniques are the presence of damage can cause variations in either global or local properties of the structure under inspection, and in turn these changes can be manifested in the captured global vibration or local wave signals. Specifically, static-parameter-based techniques rely on static parameters such as strain or static deflection, but one-order static deflection is relatively insensitive to damage. Vibration-based techniques focus on the variations in the structural dynamic characteristics due to structural damage. The structure under inspection can be taken as a dynamic system with stiffness, mass and damping. Structural damage will change structural parameters, and further the frequency-response function and modal

parameters of the structural system. Accordingly, the change in modal parameters such as natural frequencies, mode shapes and modal damping indicates presence of damage in the structure. Representatively, Yan *et al.* [38] have given a detailed literature review on vibration-based damage detection. Nevertheless, vibration-based techniques are often insensitive to small damage since damage is a local event and it would not significantly modulate global properties of the structure. Last but not the least, elastic-wave-based techniques actively excite elastic waves to interrogate the structure under inspection. With very fast velocity, elastic waves can examine the structure within seconds, where and when required. In terms of wave scattering effects such as reflection, transmission and mode conversion due to interaction of elastic waves with structural damage, elastic-wave-based methods are able to estimate the location, severity and type of damage. Moreover, working in a high frequency range, elastic waves can detect damage in early stage of development. In the thesis, major attention is directed to elastic-wave-based SHM.

1.2 Lamb-wave-based Damage Identification

Elastic waves have been attracting considerable attention due to their attractive properties for SHM applications [29, 36, 37, 39, 40]. Elastic waves refer to mechanical waves that propagate in elastic or viscoelastic media [41]. In an infinite medium, elastic waves can be classified as two most basic modes: longitudinal waves, *i.e.* particles

motion in a direction the same with the direction of energy transfer, and transverse waves, *i.e.* particles motion in a direction perpendicular to the direction of energy transfer. While in a bounded medium, multiple wave reflections from boundaries modulate the wave fields, and thus more complex wave patterns appear, in particular guided waves. Guided waves are confined inside a waveguide, *i.e.* a structure that guides the propagation of elastic waves. For instance, Rayleigh waves, Stoneley waves and Love waves are guided waves that constrained to structural surface, material interface and layered materials, respectively [29]. Of particular interest are Lamb waves, the modality of guided waves confined inside thin plate- or shell-like structures (with planar dimensions being far greater than that of the thickness and with the wavelength being of the order of the thickness). As an elastic disturbance disseminated omnidirectionally, Lamb waves possess the capability of interrogating a large area of a structure in a prompt manner. Operated in an ultrasonic frequency range, their short wavelengths in the order of a few millimetres endow Lamb waves to access damage of very small dimension. For completeness of the thesis, fundamentals of Lamb waves were briefly reviewed in the following section.

1.2.1 Fundamentals of Lamb Waves

In 1917, the British mathematician Horace Lamb published his classic mathematical description of a sort of elastic waves captured in plates [42]. In

recognition of his contribution, such waves were named after him as *Lamb waves*. Following Lamb's work, Mindlin [43] provided a comprehensive solution to Lamb waves in 1950, and Gazis [44] analysed the dispersive properties of Lamb waves in 1958. In parallel with theoretical work, Worlton [45] was among the first to produce Lamb waves experimentally. Viktorov [46] brought Lamb waves into ultrasonic testing and recognised a good potential of such waves for NDE application. All of these studies substantially contributed to the foundation of Lamb-wave-based damage detection.

Generally speaking, merits of Lamb waves for damage inspection include:

(1) the ability to interrogate a large area using only few transducers because of fast propagation velocity;

(2) the capacity to test inaccessible or hidden components because of its omnidirectional propagation in the specimen under inspection;

(3) high sensitivity to different types of damage because of small wavelength in the order of few hundred micrometers up to few millimetres;

(4) propagation over long distances because of relatively low attenuation;

(5) the potential to be used for on-line SHM techniques in real-time manner; and

(6) low energy consumption with cost-effectiveness.

Nevertheless, a captured Lamb wave signal usually appears complex due to the multiple wave modes, wave dispersion, boundary reflection, interference of

measurement noise, *etc.*, and all of these create much difficulty in signal interpretation, entailing sophisticated signal processing tools (to be detailed in Section 1.2.3).

Although relevant literatures exist addressing Lamb waves, it is important to address the fundamentals and basic theory of Lamb waves here before we proceed to their applications in damage identification. Considering a thin isotropic plate as shown in Fig. 1.2, the governing equation of motion of elastic disturbance including Lamb waves can be given in a form of *Cartesian* tensor notation as [41],

$$\mu \cdot u_{i,jj} + (\lambda + \mu) \cdot u_{j,ji} + \rho \cdot f_i = \rho \cdot \ddot{u}_i \qquad (i, j = 1, \quad 2, \quad 3) \qquad \textbf{(1.1)}$$

where μ is the shear modulus, $\lambda = \dfrac{2\mu\nu}{1-2\nu}$ (ν is the Poisson's ratio), ρ is the mass density, u_i and f_i are the displacement and body force in x_i direction, respectively.

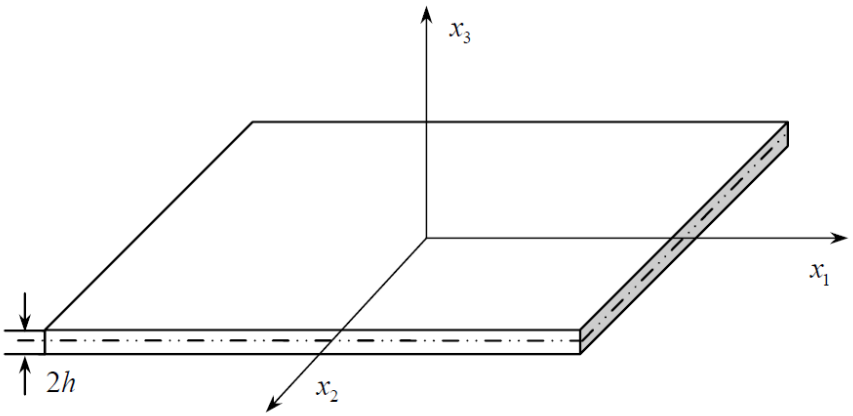

Fig. 1.2. A thin plate of 2h in thickness

The most efficient method to solve the equation above is the *displacement potentials method.* In this method, the displacement can be split into the scalar and vector potentials upon *Helmholtz decomposition*. In the absence of body forces, and in light of plane strain assumption, Eq. 1.1 can be decomposed into two uncoupled parts, which govern longitudinal waves and transverse waves, respectively, as,

$$\frac{\partial^2\phi}{\partial x_1^2}+\frac{\partial^2\phi}{\partial x_3^2}=\frac{1}{{c_L}^2}\frac{\partial^2\phi}{\partial t^2} \qquad \textit{governing longitudinal wave modes} \qquad \textbf{(1.2a)}$$

$$\frac{\partial^2\psi}{\partial x_1^2}+\frac{\partial^2\psi}{\partial x_3^2}=\frac{1}{{c_T}^2}\frac{\partial^2\psi}{\partial t^2} \qquad \textit{governing transverse wave modes} \qquad \textbf{(1.2b)}$$

where ϕ and ψ are scalar and vector potentials, respectively. $c_L=\sqrt{\frac{\lambda+2\mu}{\rho}}$ and $c_T=\sqrt{\frac{\mu}{\rho}}$ are the velocities of longitudinal and transverse modes, respectively.

Upon solving Eq. 1.2 in the case of plane strain with traction-free boundary conditions at both the upper and lower surfaces, the general description of Lamb waves can be obtained,

$$\frac{\tan(qh)}{\tan(ph)}=-\frac{4k^2qp}{(k^2-q^2)^2} \qquad \text{for symmetric modes} \qquad \textbf{(1.3a)}$$

$$\frac{\tan(qh)}{\tan(ph)}=-\frac{(k^2-q^2)^2}{4k^2qp} \qquad \text{for anti-symmetric modes} \qquad \textbf{(1.3b)}$$

$$p^2=\frac{\omega^2}{{c_L}^2}-k^2,\quad q^2=\frac{\omega^2}{{c_T}^2}-k^2,\quad k=\frac{2\pi}{\lambda_{wave}}$$

where h, ω, k and λ_{wave} are the half-thickness of the plate, wave circular frequency, wavenumber and wavelength of the wave, respectively. Eq. 1.3(a) and 1.3(b) are known as the Rayleigh-Lamb equations.

As defined by Eq. 1.3, Lamb waves include two types of modes, *i.e.* symmetric modes and anti-symmetric modes with the schematic of particle motion for two wave modes shown in Fig. 1.3. Each type of mode consists of a fundamental modality and a series of higher-order modalities. For brevity, symbols S_i and A_i ($i = 0,\ I,\ II,\ III, \cdots$) hereinafter stand for the symmetric and anti-symmetric modes, respectively, with the subscript being the order. S_i and A_i modes dominate the in-plane and out-of-plane motion of the particles in the plate, respectively.

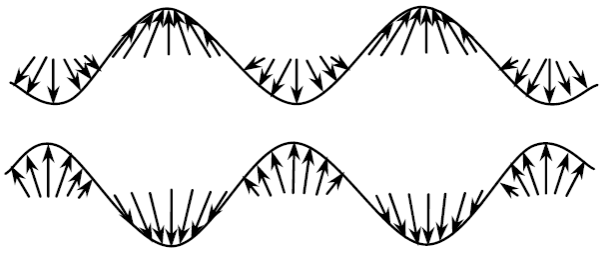

(a)

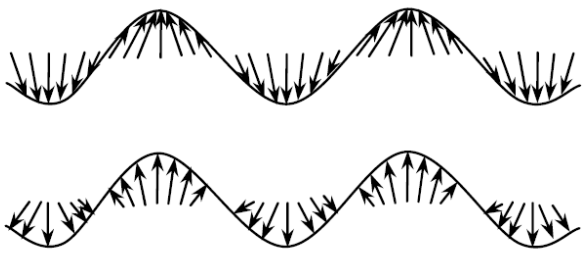

(b)

Fig. 1.3. Schematic of particle motion of (a) symmetric and (b) anti-symmetric Lamb modes

Although Rayleigh-Lamb equations appear simple, they can only be solved using numerical methods. Mathmatically, at a given circular frequency ω, wavenumber k can be determined in an iterative way, to further determine the phase and group velocities. Phase velocity refers to the propagation velocity of the wave phase of a specific frequency, while group velocity is the propagation speed of the overall shape or energy of the wave, and both of them are related to wavenumber k (for phase velocity, $c_p = \frac{\omega}{k}$; for group veclocity, $c_g = \frac{\partial \omega}{\partial k}$). As a representative example, the correlation between the group velocity and frequency-thickness product in an aluminium plate is exhibited in Fig. 1.4. It is observed that wave velocity varies with frequency-thickness product, to say that Lamb waves are dispersive (*i.e.* wave proapgation velocities are dependent on wave frequencies and geometric features of the medium). These curves are also known as dispersion curves.

As shown in dispersion curves in Fig. 1.4, there exist an infinite number of Lamb wave modes. The multimodal nature of Lamb waves complicates interpretation of captured wave signals. To benefit practical implementation and signal interpretation, the excitation frequency of Lamb waves should ideally be selected to be lower than the cut-off thresholds of higher-order Lamb modes, where only the lower modes are available. Another problem that affects Lamb-wave-based damage detection refers to the wave dispersion aforementioned. As a result of the dispersion, a Lamb wave signal spreads out in time domain as propagation. This phenomenon causes an increase in

time duration of a captured wave packet and makes signal interpretation challenging. In practice, there are generally two methods to minimise the effect of Lamb wave dispersion [47]: a) a less-dispersive region is often selected where the excitation frequencies are lower than cut-off frequncies of higher wave modes and only fundamental wave modes S_0 and A_0 are available travelling at almost constant velocities, respectively, as seen the encircled rectangle in Fig. 1.4; b) an excitation signal with limited bandwidth is selected as diagnostic signal to confine the input energy in a narrow frequency range such as Hanning-window-modulated sine tonebursts.

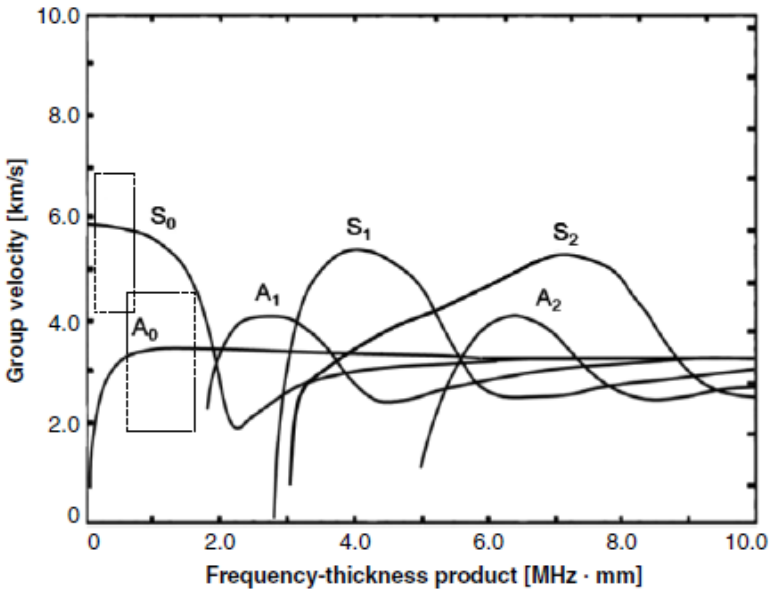

Fig. 1.4. Dispersion curves of Lamb waves in an aluminium plate [48]

1.2.2 Activating and Receiving Lamb Waves

Ultrasonic probe is among those most commonly used transducers to generate and receive Lamb waves [1, 2]. Traditional ultrasonic probes include angled piezoelectric wedge transducers, comb transducers, and Hertzian contact transducers. One significant advantage of these transducers is the ability to selectively produce a pure Lamb mode. Without the complexity of multiple modes, captured wave signals can be readily interpreted. But traditional probes require a couplant (such as oil) to transfer Lamb waves into a structure, which may affect their operational efficiency. Accordingly, innovative non-contact transducers are increasingly introduced such as air-coupled, fluid-coupled transducers and electromagnetic acoustic transducers (EMATs) [20, 21]. In general, ultrasonic probes are highly sensitive and accurate, safe to operation, and conducive to estimate the location and severity of various types of damage. Nevertheless, although effective and powerful for damage detection, ultrasonic probes are not compact enough to be permanently installed into a structure under inspection, and therefore can hardly be used for online SHM purposes. This is especially true for aircraft structures, where the mass and space of installed transducers should be minimal.

Piezoelectric Elements

The most popular transducers that can potentially be used for SHM applications are piezoelectric elements, as typified by piezoelectric lead zirconate titanate (PZT) wafers, polyvinylidene fluoride (PVDF) piezoelectric polymer film and piezocomposite transducers (as seen in Fig. 1.5(a)). They are light in weight, small in size, and affordable in price, and thus particularly suitable to be embedded in or surface-mounted onto a structure for health monitoring. Piezoelectric elements are operated in accordance with the dual piezoelectric effect, *i.e.* direct (applied mechanical force producing an electric charge) and converse (applied electric field generating mechanical strain) piezoelectric effect, which causes the acquisition and generation of Lamb waves, respectively. Specifically, an alternating electrical voltage is imposed onto a piezoelectric element, which surface-bonded to a mechanical structure. As a result of the converse piezoelectric effect, mechanical deformation is created, which causes the generation and propagation of Lamb waves inside the structure under inspection. The waves that carry structural information are subsequently collected by another piezoelectric element, which converts the mechanical strain into electric charges, due to direct piezoelectric effect.

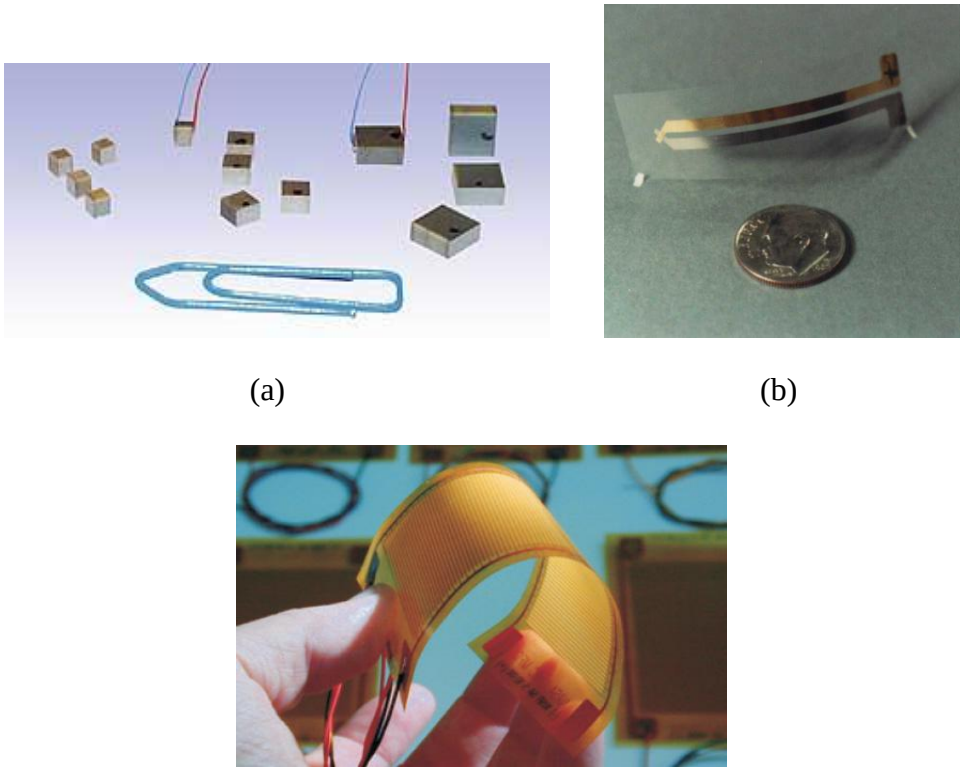

(a) (b)

(c)

Fig. 1.5. Typical piezoelectric elements: (a) PZT wafers in various sizes; (b) a PVDF piezoelectric polymer film; and (c) an MFC transducer [39]

PZT is one of the most prominent piezoelectric materials [49-54]. Merits of PZT wafers include high performance in both the wave generation and acquisition, good mechanical strength, easy integration into a host structure, low power consumption, low cost, and wide frequency response. Nonetheless, PZT-induced Lamb waves usually include multiple modes without appropriate handling, therefore posing certain difficulties in signal interpretation. In addition, PZTs are quite brittle and may not be easy to be attached to a curved shell structure. PVDF is another piezoelectric material popular in SHM applications [55-57], as one example shown in Fig. 1.5(b). Compared

with PZTs, PVDFs are very flexible in deformation, and thus can be shaped to deal with curved surfaces. Nevertheless, PVDFs generally serve as sensors due to their weak converse piezoelectric properties. Moreover, PVDFs are not often used to be inserted into a composite structure as they may lose their piezoelectric properties during curing process. Piezocomposites are another kind of innovative transducers for the generation and collection of Lamb waves [58-60]. Piezocomposites combine the piezoelectric efficiency of a PZT with the flexibility of polymer films by integrating piezoelectric powder and piezoceramic fibre into an epoxy resin. As a representative piezocomposite transducer, macro fibre composite (MFC), in Fig. 1.5(c), can provide better piezoelectric performance than a PZT wafer of same size in terms of actuation efficiency [39].

Fibre-optic Sensors (Reception Only)

Optical fibre, a transparent fibre that guides light along a specific path as seen in Fig. 1.6, is a type of material suitable for SHM applications, because of its light weight, small size, good flexibility, long life, low power consumption and good immunity to electromagnetic interference in particular [30, 31, 36, 61]. In comparison with traditional piezoelectric elements, fibre-optic sensors hold a rather higher bandwidth capability (up to 25 MHz) as a result of the absence of mechanical resonances [61]. Fibre-optic sensors usually work in three manners, *i.e.* on the basis of light intensity

variation, interferometry, and fibre Bragg gratings (FBG) techniques. In particular, FBG sensors are attracting increasing attention in the community due to their high sensitivity to elastic wave disturbance [62-64]. Unlike a circular PZT wafer that senses Lamb wave omnidirectionally, a FBG sensor is orientation-dependent, *i.e.* the amplitude of a Lamb wave signal captured in the direction parallel to the wave propagation can be 100 times larger than that measured in the direction perpendicular to the wave propagation [64]. Such strong directivity of a FBG sensor may reduce its efficiency in capturing Lamb wave signals. Another disadvantage of such a sensor is the relatively high cost of the associated support equipment.

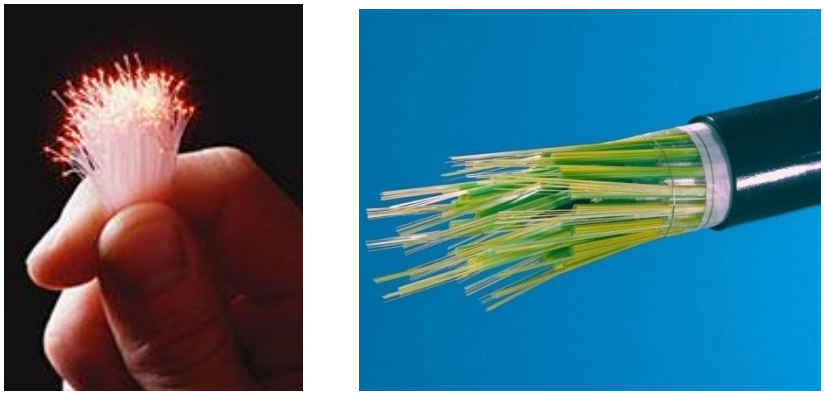

Fig. 1.6. Fibre-optic sensors

Sensor Network Technology

A single sensor provides very limited information. To enrich information for damage detection, a number of actuators/sensors are usually employed to configure a

sensor network. By communicating with each other, sensors in the network can provide abundant information for evaluating structural damage, therefore increasing identification confidence, minimising dependence of identification on a particular sensor and improving tolerance to measurement noise. Generally speaking, the resolution or identification capability of a sensor network is subject to the density of transducers employed. However, a very dense sensor network will cause a great cost and is impractical for engineering application. In practice, practicability and resolution have to be compromised to design an appropriate sensor network towards a specific application. Because of the ability to interrogate a large area from a single transducer position, Lamb waves are preferred to perform cost-effective SHM, whereby a relatively sparse network of transducers (*e.g.* PZT wafers) are often employed [65-67]. As a well commercialised example, SMART Layer (Stanford Multi-Actuator-Receiver Transduction Layer) integrates a series of PZT elements into a dielectric film to form a sensor network [67]. Such a thin and flexible layer can either be surface mounted or embedded into a structure with little intrusion to the host structural integrity. In addition, the layer can be customised to different shapes for various applications [66, 68, 69].

1.2.3 Processing of Lamb Wave Signals

As commented previously, captured raw Lamb wave signals often present rather complex appearance due to the existence of various measurement noise, wave

dispersion, multiple wave modes, mode conversion, multiple wave reflection from structural boundaries. Signal processing is an effective way to screen these unwanted signal components and subsequently extract key information useful for damage identification from the raw signals. Generally, signal processing methods can be divided into three categories, *i.e.* time-domain analysis, frequency-domain analysis and joint time-frequency domain analysis.

Time-domain

A collected Lamb wave signal is usually presented in the time-domain, providing information such as time-of-flight (ToF), signal magnitude, signal energy and signal phase. Time-domain analysis aims at extracting useful signal features and applying them to damage identification. One typical time-domain analysis tool refers to Hilbert transform (HT). HT is a type of integral transform with the purpose of canvassing a wave signal in terms of its energy distribution in the time-domain [70-72]. For an arbitrary Lamb wave signal $f(t)$, the Hilbert transform is defined as [73],

$$H(t) = \frac{1}{\pi} \int_{-\infty}^{+\infty} \frac{f(\tau)}{t-\tau} \mathrm{d}\tau \qquad \textbf{(1.4)}$$

The Hilbert transform (Eq. 1.4) performs a $90\,°$ phase-shift to construct an analytic signal $Z(t)$,

$$Z(t) = f(t) + iH(t) \quad \textbf{(1.5)}$$

whose real part and imaginary part are the original signal $f(t)$ and its Hilbert transform $H(t)$, respectively. The module of the analytic signal, *i.e.* $e(t) = \sqrt{f^2(t) + H^2(t)}$, depicts the energy distribution of $f(t)$ in the time domain.

Frequency-domain

Sole time-domain analysis may be insufficient to extract rich signal features due to the interference of various noise. With a view to substantially reduce noise, a captured Lamb wave signal can be converted into the frequency domain. Low-pass filter and high-pass filter can subsequently be applied to help suppress unwanted frequency bands. As a result, only frequency band of interest is retained. This serves the fundamental of frequency-domain analysis. In this aspect, Fourier transform (FT) is an effective tool. Given an arbitrary Lamb wave signal $f(t)$, FT converts it into the frequency domain through [74],

$$F(\omega) = \int_{-\infty}^{+\infty} f(t) e^{-j\omega t} \mathrm{d}t \ , \quad \textbf{(1.6)}$$

where ω and j are the angular frequency and unit complex, respectively. $F(\omega)$ is the Fourier counterpart of $f(t)$. Upon application of Eq. 1.6, the time-domain signal $f(t)$ is decomposed into a series of components of different frequencies. In practice,

Fast Fourier Transform (FFT) is more often used to calculate frequency spectrum instead of FT due to the distinct improvement in calculation speed. Although with good capacity to de-noise, FFT-based frequency-domain analysis may cause loss of temporal information.

Joint Time-frequency Domain

Frequency-domain analysis applies FFT to get the frequency spectrum of an acquired Lamb wave signal. But it does not provide visualization about the instant of time at which a wave component of specific frequency arrives. Time-frequency domain analysis is thus introduced to deploy a time-domain signal into a time-frequency space, from which signal features concerning 'when' (time) and 'who' (a specific frequency component) are presented simultaneously. Short-time Fourier transform (STFT) and wavelet transform (WT) are two common time-frequency domain analysis tools [75-79].

Compared with FFT, STFT delivers good performance in processing non-stationary signals, Lamb wave signals as examples. To perform STFT, a captured time-domain signal is multiplied by a window function (commonly a Hanning or Gaussian window) with regard to a short period of time. Then traditional FT is conducted as the short time window sliding along the time axis, resulting in a time-frequency representation of the

signal [74]. Representatively, Ihn and Chang [75] utilised STFT to convert raw Lamb wave signals to time-frequency domains, from which frequency component whose central frequency is the same as excitation frequency was extracted. Key features of this component were subsequently applied for damage identification, *e.g.* time-of-flight. Likewise, Ostachowicz [47] used STFT to get spectrogram of Lamb wave signals, *i.e.* 2D representation of the frequency content energy of a signal as it changes over time. The wave component corresponding to the excitation frequency was extracted for further analysis.

WT is another powerful tool for signal processing. Unlike FT decomposing a time-dependent signal into a series of sine and cosine, WT decomposes a signal into a series of wavelets, *i.e.* a waveform with limited duration whose average amplitude equals zero. Upon WT, a wave signal is transformed into a 2D representation with regard to scale and time. Fundamentally, WT of an arbitrary Lamb wave signal $f(t)$, at a scale a and translational value b, is defined as [76],

$$W(a,b) = \frac{1}{\sqrt{a}} \int_{-\infty}^{+\infty} f(t) \psi^*(\frac{t-b}{a}) \mathrm{d}t \,, \tag{1.7}$$

where $W(a,b)$ is wavelet coefficient. $\psi(t)$ is a basic wavelet function, while $\psi^*(t)$ is the complex conjugate of $\psi(t)$. Scale is inversely proportional to frequency as [76],

$$F_a = \frac{F_c}{a \cdot \Delta} \,, \tag{1.8}$$

where a, Δ, F_c, and F_a are scale, sampling period, the centre frequency of a wavelet, and the frequency corresponding to the scale a. In light of Eq. 1.7 and 1.8, the captured time-domain signals are transformed into a 2D time-frequency space.

Compared with STFT, WT offers a better signal representation as a result of deployment of the signal with multiresolution [76]. Two types of WT are available: continuous wavelet transform (CWT, defined by Eq. 1.7) and discrete wavelet transform (DWT). Generally speaking, CWT is particularly effective for signal energy visualization and feature extraction; and DWT is more efficient for signal de-noising, filtration, compression. Both of them have been extensively used for signal processing in damage identification exercises. Representatively, Su *et al.* [77] applied DWT to process Lamb wave signals captured from PZT sensors surface-mounted on composite materials. Sohn [78] utilised CWT to extract damage-sensitive features from raw Lamb wave signals for the detection of delamination. Paget *et al.* [79] designed a new wavelet base and employed it to decompose Lamb wave response into wavelet coefficients. The changes in wavelet coefficients were subsequently used to detect impact damage in aerospace composites. Generally speaking, applied with WT, raw captured signals are filtered and refined, and thus well suited for further feature extraction and interpretation.

1.3 Diagnostic Imaging

Damage identification is like detective work to catch the damage in a structure. This process is a typical inverse problem, *i.e.* we attempt to infer the reason (damage) from the outcome (damage-scattered Lamb wave signal), which is often ill-posed and difficult to solve using purely rational and logical means. Algorithms to solve such a problem have been extensively examined over the years. As one of recent research focuses, imaging-based identification has been more and more preferred from the community [36, 47, 75]. The ultimate output of the imaging-based identification is an easily interpretable and intuitional image reflecting damage details or the overall 'health' status of the structure under inspection. Often operated in an automatic manner, this approach can efficiently minimise the dependence of identification results on subject interpretation.

As a traditional imaging technique, tomography has gained maturity in the past several decades [80-82]. Fig. 1.7(a) shows the scanning geometry for a typical tomography configuration: parallel-projection tomography. In the example, the structure under inspection is carefully scanned with a pair of transducers (one serves as actuator, the other as sensor) moving along a certain angle. Once the measurement is done by this angle, the sample is rotated with a very tiny angular increment and measurement is repeated. Thanks to the high ray density (due to the very tiny angular increment), tomography presents accurate diagnostic results (as shown in Fig. 1.7(b)).

However, traditional imaging-based approach, typified by Lamb wave tomography, is often at the cost of a large number of sensors to produce dense wave paths for tomographic reconstruction. This results in either rotation of the object under inspection by very tiny increments or the consumption of a large number of deliberately allocated transducers, fairly narrowing the application domain of imaging-based approach for online SHM.

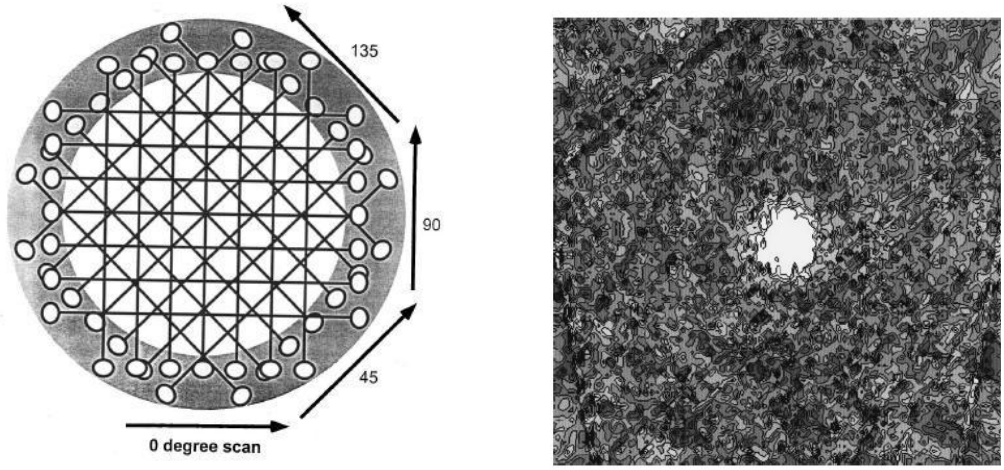

(a) (b)

Fig. 1.7. (a) the scanning geometry for parallel-projection tomography and (b) a typical tomographic reconstruction contour for detecting a flat-bottom hole [80]

Aimed at circumventing such a deficiency, novel diagnostic imaging using very limited number of sensors has been developed with assistance of efficient fusion algorithms, by taking full advantage of active sensor networks. The pivotal step for a diagnostic imaging approach is to link the extracted signal features, such as

time-of-flight and signal correlation coefficient, with damage parameters, such as damage position and severity. In light of such correlations, a grey-scale image can be developed capable of indicating the possibility of damage presence in the structure.

Generally speaking, a diagnostic imaging can be grouped into one of the following three categories in terms of different mechanisms, *i.e.* time-of-flight-based, signal correlation-based and phased-array-based diagnostic imaging.

1.3.1 Time-of-flight-based

As a type of most crucial and straightforward signal feature, time-of-flight (ToF) is the time consumed for a wave to travel a certain distance [36]. Considering an actuator-sensor pair, $S_i - S_j$ ($i, j = 1,\ 2,\ \cdots,\ N$, but $i \neq j$), a local coordinate system can be established for this sensing path as shown schematically in Fig. 1.8, where actuator S_i is at the origin, sensor S_j is at (x_j, y_j) and the centre of the damage is presumed to be at (x_D, y_D). Supposing wave velocity V is constant, a set of nonlinear equations can thus be established for individual actuator-sensor pairs, as

$$(\frac{L_{S_i-D}}{V} + \frac{L_{D-S_j}}{V}) - \frac{L_{S_i-S_j}}{V} = \Delta t_{i-j} \qquad (i, j = 1,\ 2,\ \cdots,\ N \text{, but } i \neq j), \qquad \textbf{(1.9)}$$

where

$$L_{S_i-D} = \sqrt{x_D^{\,2} + y_D^{\,2}}, \qquad L_{D-S_j} = \sqrt{(x_D - x_j)^2 + (y_D - y_j)^2}, \qquad L_{S_i-S_j} = \sqrt{x_j^{\,2} + y_j^{\,2}}.$$

In the above, Δt_{i-j} is the difference between (i) ToF for the incident wave to propagate from actuator S_i to the damage and then to sensor S_j, and (ii) ToF for the incident wave to propagate directly from S_i to S_j. L_{S_i-D}, L_{D-S_j} and $L_{S_i-S_j}$ represent the distances between S_i at $(0,0)$ and the damage centre (x_D, y_D), the damage centre and S_j at (x_j, y_j), and S_i and S_j, respectively. Eq. 1.9 depicts a series of ellipse-like loci with S_i and S_j being two foci.

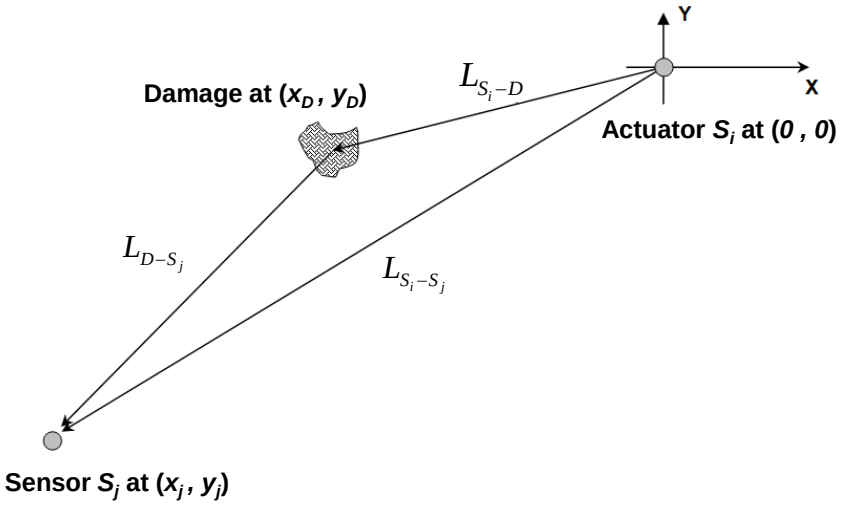

Fig. 1.8. Relative positions among actuator S_i, sensor S_j and damage in the local coordinate system for sensing path $S_i - S_j$

Upon Eq. 1.9, temporal information of captured wave signals is converted to spatial loci indicating possible damage locations. Traditional ToF-based identification attempts to determine damage position by seeking intersections of multiple spatial loci, which is often problematic due to pseudo intersections and limited to the accuracy of mathematic calculation. Unlike traditional method, ToF-based diagnostic imaging

utilises the correlations between the distance of a spatial position to a root locus and probability of damage presence at that location, which gives rise to a source image reflecting the perception as to the damage. Subsequently, upon developed image fusion schemes, source images are appropriately aggregated, leading to a resultant image indicating health status of the structure under inspection.

Using such a philosophy, Ihn and Chang [75], Michaels [83, 84], Wang *et al.* [85], Konstantinidis *et al.* [86] and Su *et al.* [87, 88] developed various ToF-based diagnostic imaging to quantify damage location and size by analysing the ToFs of waves scattered by structural flaws. In most studies, the damage-scattered wave packets (residual signal) are extracted by comparing a current signal (captured from the structure under inspection) with a baseline signal (captured from the benchmark counterpart). ToF of the damage-scattered wave packets are further determined. It is noted that, to enhance the recognisability of the damage-scattered wave signals, novel signal processing tools such as STFT [75], WT [87] and HT [86] are often employed as auxiliary tools. A typical diagnostic image following the above ToF-based principle is shown in Fig. 1.9. In the image, the lighter the pixels, the greater the probability of damage exists there. The solid circle indicates actual delamination, while dotted circle indicates predicted delamination if 80% of the maximum of value of probability is set as a threshold. It can be seen that the predicted damage matching well with the actual one.

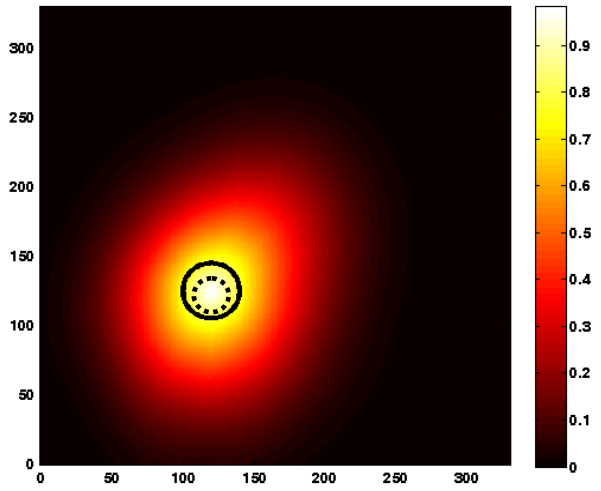

Fig. 1.9. One typical resultant probability image for the detection of a delamination in a composite laminate [88]

1.3.2 Signal Correlation-based

As an important signal feature, the correlation coefficient between the captured wave signals $X = \{x_1, x_2, ..., x_n\}$ (current signal) and its corresponding baseline signal $Y = \{y_1, y_2, ..., y_n\}$ can also be used to developed various diagnostic imaging approaches. In this aspect, the correlation coefficient is defined as,

$$\rho_{XY} = \frac{C_{XY}}{\sigma_X \sigma_Y} \tag{1.10}$$

where C_{XY} is the covariance of *X* and *Y*, σ_X and σ_Y are the standard deviations of *X* and *Y*, respectively. In the case that damage right locates on or very close to a particular actuator-sensor sensing path via which the current signal is captured, the current signal

is expected to change significantly compared with its corresponding baseline signal, leading to a relatively small correlation coefficient. The signal change would decrease if the damage is away from the actuator-sensor path, resulting in a large correlation coefficient. Therefore, correlation coefficient between the current and baseline signals serves as an indication of the overall change due to the damage in the structure.

The correlation coefficient has been proven to be in particular susceptible to changes in signal phase as well as local signal amplitude [89], advantageous over other signal features in terms of the sensitivity to phase delay (leading to changes in ToF) and reduction in signal amplitude (leading to changes in intensity of signal energy). Representatively, Zhao *et al.* [90] introduced a correlation analysis-based technique for health monitoring of an aircraft wing. The developed method showed good performance in detecting simulated cracks and corrosion. Hay *et al.* [91] employed fan-beam tomography and signal-correlation-based diagnostic imaging to detect material loss on aircraft components, to conclude that the latter showed better performance for damage identification in the case that the same number of sensors were used (as compared in Fig. 1.10). Likewise, Wang *et al.* [92] developed a probabilistic diagnostic imaging based on correlation analysis and employed it to inspect a stiffened composite plate of aging aircraft. Nevertheless, despite its ability of delivering good property in damage identification, signal-correlation-based diagnostic imaging usually requires a relatively large number of actuator-sensor paths to cover the inspection area.

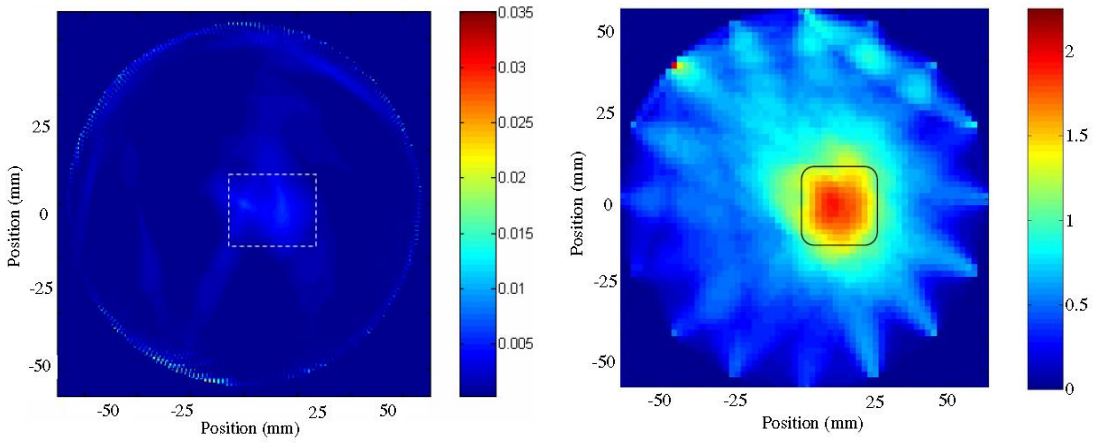

(a) (b)

Fig. 1.10. Reconstructed diagnostic image using (a) fan-beam tomography and (b) signal-correlation-based diagnostic imaging [91]

1.3.3 Phased-array-based

Phased-array is a device consisting of a series of transducer elements (usually piezoelectric elements) which can be sequentially activated with programmable time delays. By adjusting the spacing and/or phasing between the transducer elements, generated Lamb waves can be focused in a specific direction (*i.e.* beamforming) and by changing the direction the whole interest area can be inspected.

Consider a phased array consisting of N piezoelectric elements, Fig. 1.11. The piezoelectric elements in the array are spaced at a distance d, which is much smaller

than the distance from the array to a generic far-distance point, *P*, of the structure under inspection, denoted by *r*. Since $d << r$, the activated waves coming from the array to point *P* can be assimilated with a parallel fascicle, of azimuth ϕ. Because of the array spacing, the distance between one array element and the generic point *P* will be different from the distance between another array element and *P*. For the n^{th} element, the distance will be shortened by $n(d\cos\phi)$. If the elements are fired with a time delay, δ_n, $n = 0, 1, \cdots, N-1$, then the resulting signal arriving at *P*, $f_P(t)$, is [93]

$$f_P(t) = \frac{1}{\sqrt{r}} \sum_{n=0}^{N-1} f_T(t - \frac{r}{c} + \frac{n(d\cos\phi)}{c} - \delta_n) \qquad (n = 0, \quad 1, \quad \cdots, \quad N-1), \quad \textbf{(1.11)}$$

where $\frac{1}{\sqrt{r}}$ represents the decrease in the wave amplitude due to wave attenuation, and $\frac{r}{c}$ is the time for the wave to travel the distance *r*. $f_T(t)$ is the signal generated by each array element, having the same waveform but with different phase delay. If we set $\delta_n = \frac{n(d\cos\phi)}{c}$, the above equation can be simplified as,

$$f_P(t) = N \cdot \frac{1}{\sqrt{r}} f_T(t - \frac{r}{c}) \qquad \textbf{(1.12)}$$

The resulting signal, $f_P(t)$, is then can be seen to be enhanced *N* times in magnitude in a specific direction, ϕ (also along $-\phi$), in comparison with the signal activated by a single actuator, $f_T(t)$.

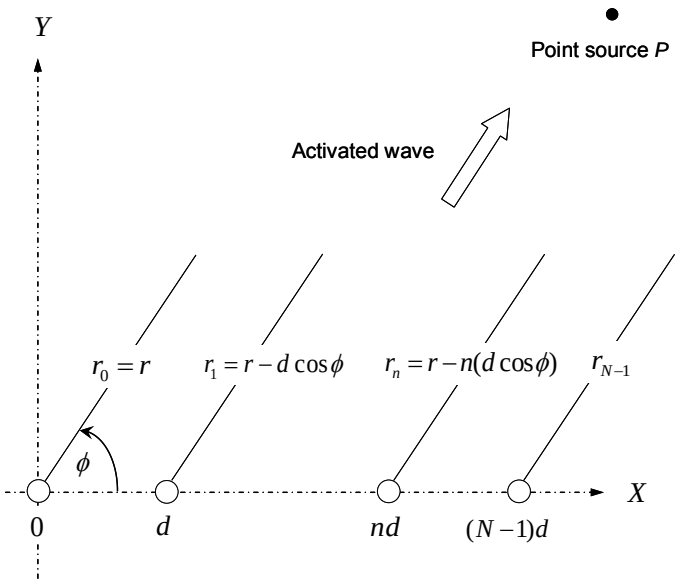

Fig. 1.11. Principle of transmitter beamforming [93]

In light of the above principle, a large region of a structure can be scanned by steering the resulting waves in different directions (with intensified signal energy and therefore improved SNR), whereby structural damage, if any, can be highlighted according to damage-scattered wave. A number of studies have been directed to this aspect. Most representatively, Giurgiutiu and Bao [93] introduced a novel phased-array technique, embedded-ultrasonics structural radar (EUSR), for detection of cracks in an aluminium plate (the reconstructed diagnostic image is shown in Fig. 1.12). It has been demonstrated in that work that the developed phased-array method can substantially enhance a captured wave signal and thus improve identification accuracy. Ostachowicz *et al.* [47] employed the phased-array-based diagnostic imaging to inspect an aluminium sheet, and three artificially made dents were successfully localised by the means of phased-array. Likewise, Sundararaman *et al.* [94] employed the phased-array

method to inspect steel and composite plates, and in particular an L-shape array was designed to improve inspection precision. Though promising, there exist several disadvantages for the phased-array-based diagnostic imaging including insensitivity to areas close to the transducer array and structural boundary, negative effect of grating/side lobes on the resulting beam, and need of a large number of signals for processing. In addition, distance between two neighbouring transducers must be precisely chosen and time-delay must be deliberately designed, resulting in certain challenge in practical implementation of such a technique.

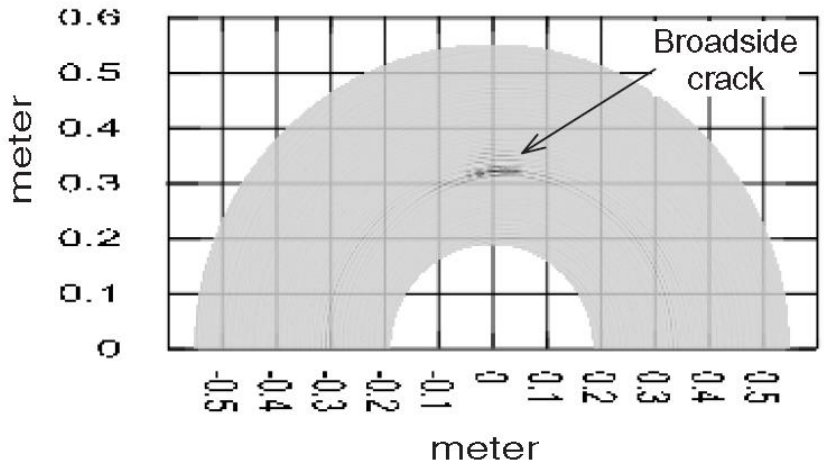

Fig. 1.12. EUSR mapping result for the detection of a broadside crack [93]

1.4 Current Challenges, Objectives and Scope of the Thesis

In the past two decades, there has been increasing awareness of developing various SHM techniques and introducing them to different industrial sectors. Successful implementation of SHM can help increase operational efficiency, improve reliability, reduce exorbitant maintenance costs and prolongate the lifespan of an industrial asset under monitoring. In this aspect, Lamb waves serve as a prominent option to develop SHM techniques. Although remarkable progress has been made towards Lamb-wave-based SHM, there still exist some challenging issues for future development of such a technique, and some of them are briefed as below:

(1) as commented in Section 1.3, diagnostic imaging has been attracting a great deal of attention in recent years. Nevertheless it is yet envisaged that majority of the current diagnostic imaging approaches, substantially based on canvassing changes in temporal information such as time-of-flights (ToFs) extracted from captured wave signals, fail to portray damage quantitatively including its orientation, shape and size, because difference in damage orientation, shape and size would not lead to pronounced changes in temporal information. It should be addressed that damage orientation/shape is a very important parameter for damage evaluation. For example, it's more dangerous if a structure bear a fatigue crack than a circular hole. Accordingly, it is of significance to characterise damage orientation/shape in SHM, especially using very few sensors.

(2) when dealing with orientation-specific or sharp-angled damage featuring a dominant size in a particular dimension (*e.g.*, a crack or a notch), a challenging issue is that such sort of damage often exerts strong directivity to wave propagation. It is largely different from those damage types with relatively smooth boundaries or edges such as a through-thickness hole or delamination which scatters elastic waves omnidirectionally. As a result, information associated with damage may not be efficiently extracted from signals captured by sensors at certain locations, in the absence of prior knowledge of damage shape. Further down to a fine level, the periphery of structural damage such as delamination can be described as the continuum of a number of cracks with various lengths which shape the damage, although macroscopically the damage often presents relatively smooth boundaries. That implies ascertainment of orientation of individual cracks can facilitate depiction of damage shape and further severity. Allowing for this it is of necessity to calibrate the influence of damage orientation on Lamb wave propagation, a prerequisite to develop a quantitative Lamb-wave-based damage identification approach for damage of arbitrary shape.

(3) detection of multiple damage is another issue worthy of investigation. The use of Lamb waves seems more viable than other NDE or SHM tools because of their exclusive responses to different damage status. More complex scattering phenomena complicate the interpretation of Lamb wave signals, and distinguishing of different

wave components in a captured signal scattered by different damage sources remains problematic. Although there are some recent publications addressing this issue, it is still a challenging issue in Lamb-wave-based SHM, especially when only few sensors are used.

It is the above-addressed three deficiencies of current SHM techniques that have motivated the present study. The objectives of this study are proposed as below:

(1) to develop a synthetic imaging identification approach based on Lamb wave propagation that is capable to collectively process the sensor network data in order to quantitatively identify structural damage;

(2) to be able to detect orientation-specific (such as cracks) and multiple damage instances in structures;

(3) to design an efficient sensor network with significantly reduced actuator/sensor consumption in comparison with traditional imaging approaches such as Lamb wave tomography;

(4) to present structural damage in an intuitive manner using probability-based diagnostic imaging;

(5) to experimentally validate the developed approach and system (both hardware and software) by identifying various damage scenarios (including notches, polygonal hole and multi-damage) through experiments and numerical simulations.

This thesis is organised as follows. In Chapter 2, three fundamental studies were performed: (i) influence of crack orientation on Lamb wave propagation; (ii) attenuation of Lamb wave propagation; and (iii) influential area of damage on a particular wave sensing path. In Chapter 3, based on the fundamental studies (i) and (ii), a probability-based diagnostic imaging (PDI) approach using sole pulse-echo configuration was developed. Effectiveness of the developed approach was demonstrated by FE simulation and experiments. In Chapter 4, based on the fundamental studies (i), (ii) and (iii), an enhanced PDI approach using hybrid pulse-echo and pitch-catch configurations was developed. The improved diagnostic results from experiments demonstrated the importance of integrating more signal features for damage identification. In Chapter 5, concluding remarks arising from this work were presented and future work was recommended.

CHAPTER 2 Fundamental Investigation

2.1 Introduction

Diagnostic imaging based on Lamb waves has attracted increasing attention because it yields an easily interpretable and intuitional quantitative map concerning the 'health' state of the structure under inspection. Despite the fact that most approaches in this field have the capacity of locating damage, quantitative depiction of damage including its shape and size is still among those highly challenging tasks. This difficulty is particularly accentuated for orientation-specific damage of sizable length in a particular dimension (*e.g.*, a crack or a notch) because such sort of damage exerts strong directivity to wave propagation and as a consequence the damage-scattered waves may not be captured efficiently at certain sensing locations in the absence of prior knowledge on damage orientation.

To tackle the above problems and revamp existing techniques, three fundamental studies were performed, which served as knowledge basis for developing an enhanced diagnostic imaging technique. They are:

(i) influence of crack orientation on Lamb wave propagation;

(ii) attenuation of Lamb wave propagation; and

(iii) influential area of damage on a particular wave sensing path.

On the basis of these three fundamental studies, a novel probability-based diagnostic imaging (PDI) approach was developed with the capability of quantitatively depicting the location, shape, and the size of the single or multiple structural damage.

2.2 Design of Diagnostic Signal

Activation of a diagnostic Lamb wave signal with an *appropriate* mode in an *appropriate* waveform and of an *appropriate* frequency is crucial for any Lamb-wave-based damage identification exercise. In general, a proper diagnostic Lamb wave should feature (i) non-dispersion, (ii) high sensitivity (iii) easy excitability, and (iv) low attenuation.

2.2.1 Selection of Lamb Wave Mode

Dispersion curves of Lamb waves propagating in an aluminium plate with a thickness of 1.5 mm (all aluminium plates used in this study were 1.5 mm thick) were calculated and exhibited in Fig. 2.1. To reduce the effect of multi-mode, the selected

excitation frequency is lower than the A_1 cut-off threshold, whereby only the fundamental Lamb modes S_0 and A_0 co-exist. Both S_0 and A_0 Lamb modes have often been employed for developing various SHM and damage identification techniques [36]. In this study, A_0 was preferred because it, in comparison with its symmetric counterpart, S_0, has (i) a shorter wavelength at a given excitation frequency and therefore higher sensitivity to damage of smaller size, and (ii) higher sensitivity to surface damage such as corrosion and surface cracks.

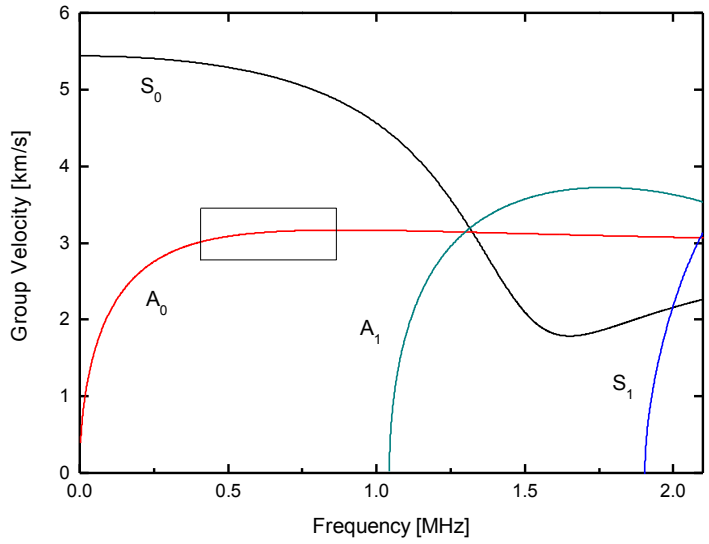

Fig. 2.1. Dispersion curves of Lamb waves in an aluminium plate with the thickness of 1.5 mm

To selectively generate a particular Lamb mode (A_0 in this study), some theoretical models were introduced to predict the appropriate frequency bands where a certain Lamb mode is particularly strong while the other modes are substantially weak. Giurgiutiu [95] conducted an analysis on the PZT actuator-structure interaction using a

space-domain Fourier transform. Upon the Lamb modes tuning, a 'Sweet spot' could be determined where a particular Lamb mode (S_0 or A_0) dominates overall energy of the signal. But, without considering the effect of the bonding layer between PZT wafers and the host structure, this model seems to be insufficient to depict such phenomena, because the adhesive stiffness and the thickness of the bonding layer considerably affect the coupling. Although some recent studies well attended the effect of bonding layer [53, 54, 96], accurate prediction of such a 'Sweet spot' is still a challenging issue. In this study, experimental tuning was conducted instead of complicated theoretical work (to be detailed in Section 3.5.3). Through experimental tuning, an input frequency of 450 kHz was selected, whereby the S_0 mode was substantially suppressed, while A_0 mode stood out.

2.2.2 Design of Waveform

In most existing studies, to reduce the effect of dispersion, i) a less-dispersive region was often selected where A_0 mode travels at almost constant velocities, such as the region highlighted by the rectangle in Fig. 2.1; and ii) an excitation signal with limited bandwidth was selected to concentrate input energy into a narrow frequency range. Allowing for the fact that the smaller the bandwidth the less the dispersion is, whereby the input waveform can keep its shape when propagating in the medium, windowed sinusoidal tonebursts at a particular excitation frequency, rather than a

broadband pulse was employed as the diagnostic input signal. In this aspect, Ostachowicz *et al.* [47] compared different types of modulation windows including rectangular, triangular and Hanning windows *etc.*, and found that Hanning window has lower magnitude of side lobes in comparison with others. Ihn and Chang [23] concluded that the increase in the number of cycles can narrow the bandwidth, resulting in less dispersion and benefiting signal interpretation. However, a large number of cycles of the windowed tonebursts can reduce the time resolution since different wave components, such as incident and reflected waves, may overlap with each other. Therefore, there is always a trade-off between a good dispersion characteristic and time resolution.

In consideration of the above, a five-cycle Hanning-window-modulated sinusoidal toneburst at a central frequency of 450 kHz was used as the input signal in this study (shown in Fig. 2.2).

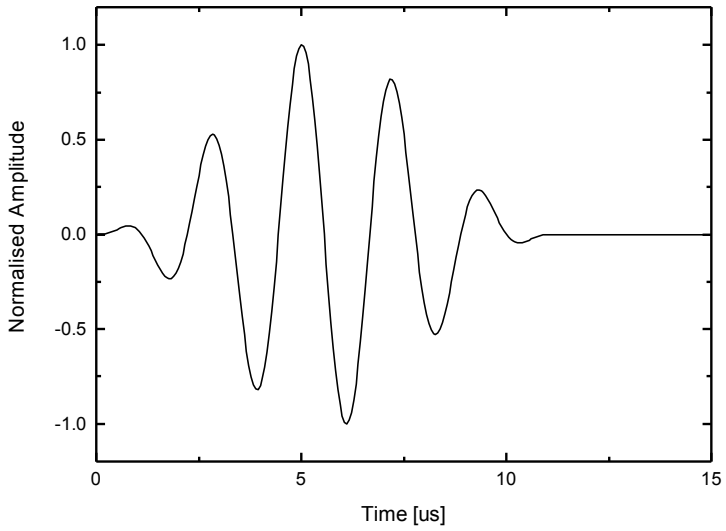

(a)

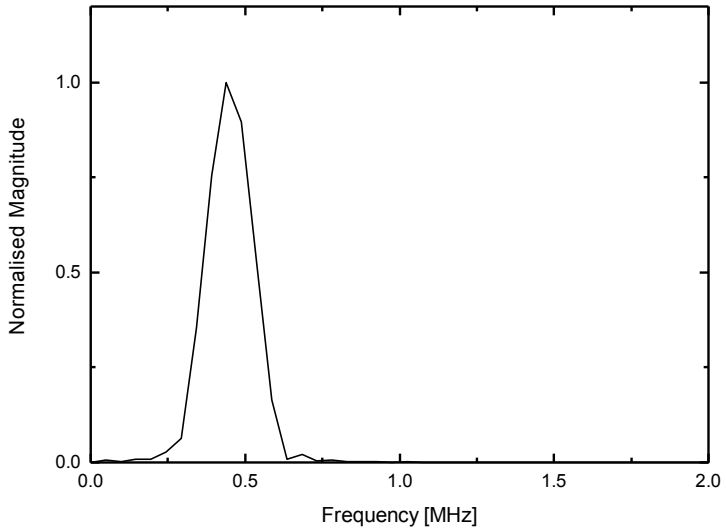

(b)

Fig. 2.2. Input excitation signal in: (a) time-domain; and (b) frequency-domain

2.3 Influence of Crack Orientation on Lamb Wave Propagation

Interaction of elastic waves with structural damage can significantly modulate their propagation characteristics, accompanied by wave scattering effects such as reflection, transmission and mode conversion; and different locations and severity of damage cause unique scattering phenomena. The above serves as the premise of the elastic-wave-based damage identification. In the case that damage features relatively smooth edges such as a through-hole or delamination, the scattered waves could be considered to propagate omnidirectionally. It is however not the case for an orientation-specific or sharp-angled damage (*e.g.*, a crack or notch). Under such circumstance the scattered waves present strong directivity and may not be captured efficiently by sensors at certain locations. Further down to a fine level, the periphery of structural damage can be described as the continuum of a number of cracks with various lengths which shape the damage. That implies ascertainment of orientation of individual cracks can facilitate depiction of damage shape and further severity. It is therefore of great interest to explore the influence of crack orientation on the propagation characteristics of Lamb waves, so as to quantitatively describe structural damage.

Some studies have been carried out to address this issue. Representatively, Lowe *et al*. [97, 98] examined the reflection of fundamental Lamb waves from a series of

surface-breaking rectangular notches with different widths and depths. An approach based on low and high frequency asymptotic analyses was used to investigate the nature of reflected waves. Ihn and Chang [23] developed a piezoelectric-based built-in diagnostic technique for monitoring fatigue crack growth. They designed a damage index and correlated the index with the progress of fatigue crack growth. Tua *et al*. [99] contributed a method to evaluate cracks, and in this method the crack orientation was determined by observing the strength of crack-scattered wave. Lu *et al*. [100] explored the effect of crack orientation on wave propagation and quantitatively evaluated the crack in terms of ascertained reflection and transmission coefficients.

Though some efforts available, quantitative evaluation of orientation-specific damage yet remains challenging. In the following sections, both finite element (FE) simulation and experimental validation were carried out to investigate and calibrate the influence of crack orientation on Lamb wave propagation.

2.3.1 FE Simulation

A thin aluminium plate measuring 600 mm × 600 mm × 1.5 mm with encastre boundary conditions was considered, as shown schematically in Fig. 2.3. A through-thickness crack, 16 mm long and 0.64 mm wide, was assumed in the plate in parallel with the lower edge of the plate, with its centre being 250 mm away from the

lower and right edges of the plate. 14 circular PZT elements, 5 mm in diameter each, were allocated on the plate, half of which served as actuators to generate elastic waves, denoted by A_i ($i = 1,\ 2,\ \cdots,\ 7$) in what follows, while the rest as sensors to capture wave signals reflected from the crack, denoted by S_i ($i = 1,\ 2,\ \cdots,\ 7$). Each PZT actuator, A_i, and its contiguous sensor, S_i (the one located on the line connecting A_i and crack centre), 7 mm apart from each other, formed an actuator-sensor pair (or a sensing path) in a pulse-echo configuration, denoted by $A_i - S_i$. Featuring the same distance of 100 mm between the actuator and crack centre, these sensing paths provided seven different angles of wave incidence (θ) relative to the crack orientation, varying from 0^0 to 90^0 with an increment of 15^0.

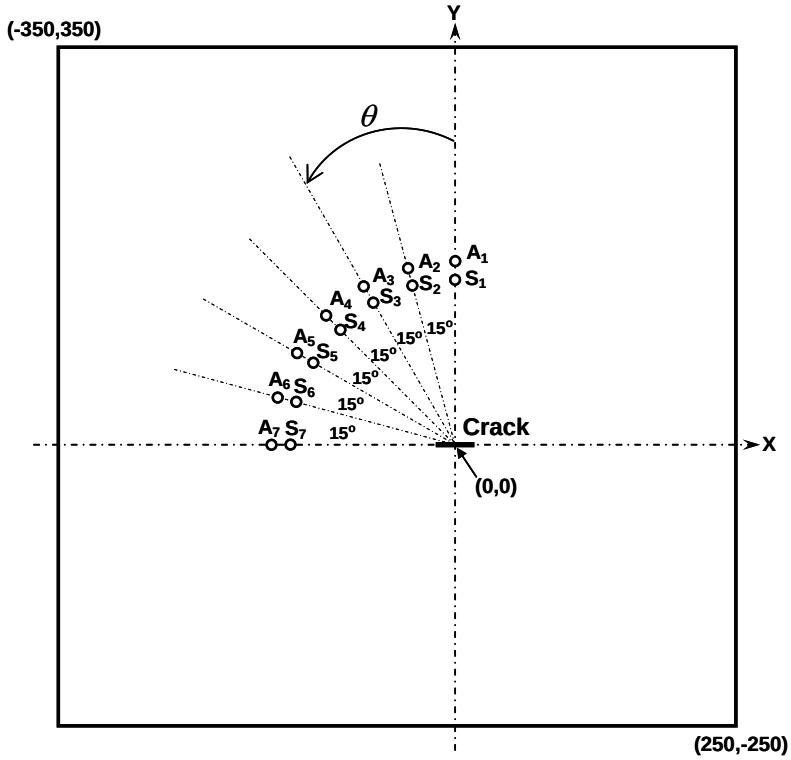

Fig. 2.3. An aluminium plate containing a through-thickness crack and seven actuator-sensor pairs (unit: mm)

The plate was modelled using three-dimensional eight-node brick elements. The crack was formed by removing associated FE elements from the plate model, in Fig. 2.4(a).A five-cycle *Hanning*-window-modulated sinusoid tonebursts at a central frequency of 450 kHz was used as the input excitation signal as explained in Section 2.2 (shown in Fig. 2.2). To ensure the dominance of the A_0 mode in signal energy, uniform out-of-plane (z-axis) displacement constraints were applied on FE nodes of the upper and lower surfaces of the PZT actuator model, as shown in Fig. 2.4(b), in recognition of the fact that the A_0 mode is dominated by the out-of-plane displacement of particles. Dynamic simulation was carried out using commercial FE package ABAQUS®/EXPLICIT due to its good property in simulating wave propagation. The crack-reflected wave signals were captured by calculating the strains at places where sensors were located. To ensure simulation accuracy, the largest dimension of FE elements was set as 0.6 mm, guaranteeing that at least ten elements were allocated per wavelength of the A_0 mode, resulting in over 1 million elements in total. The step of calculation time was controlled to be less than the ratio of the minimum distance of any two adjacent FE nodes in the model to the maximum velocity of all involved wave modes in the signal.

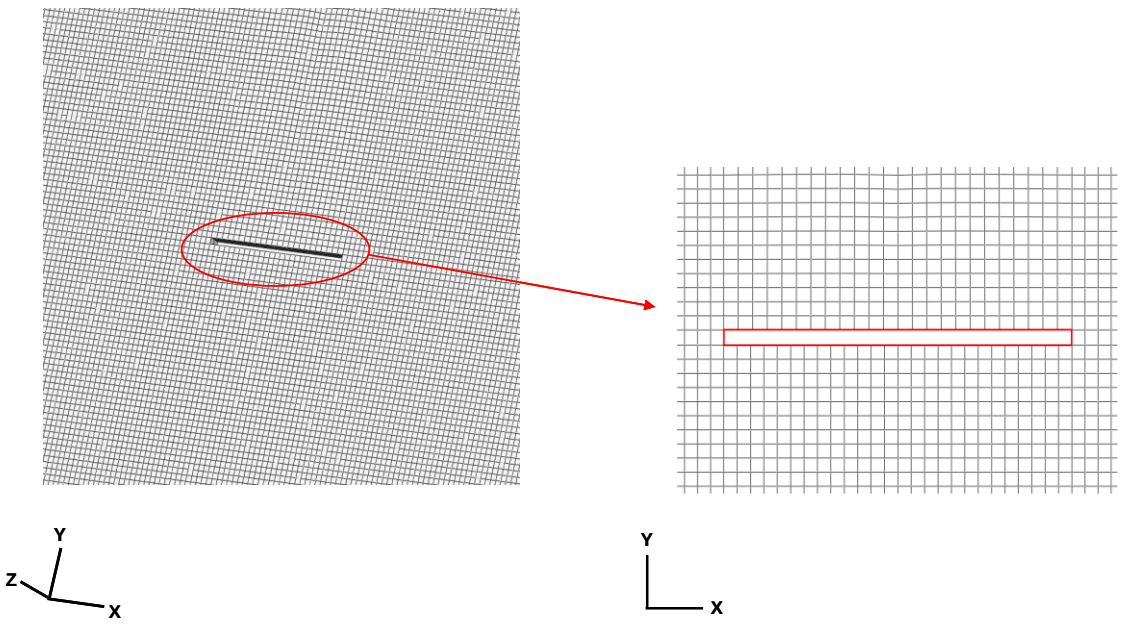

(a)

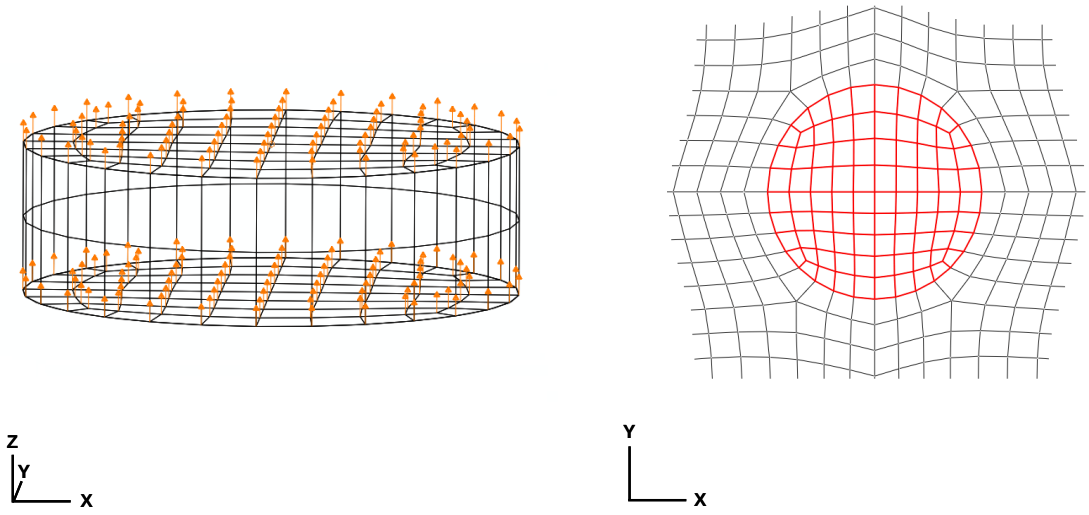

(b)

Fig. 2.4. (a) Partial FE model of the aluminium plate shown in Fig. 2.3 with zoomed-in part containing a through-thickness crack; and (b) the PZT actuator model (left: profile view, right: top view) with imposed out-of-plane (z -axis) displacement constraints for generating the A_0 mode dominantly

As typical results of simulation, crack-reflected wave signals, the residual signals upon subtracting corresponding baseline signals (those acquired via the same sensing paths in the same structure but in the absence of any damage) from current signals, acquired via three representative sensing paths, $A_i - S_i$ ($i = 1,\ 2,\ 3$; *i.e.*, $\theta = 0^0$, $\theta = 15^0$ and $\theta = 30^0$, respectively), are displayed in Fig. 2.5(a). All captured signals were normalised relative to the magnitude of their corresponding incident waves, and then treated with a Hilbert transform (HT)-based signal processing (Eq. 1.4) introduced in Section 1.2.3, so as to depict energy distribution of signals, shown in Fig. 2.5(b).

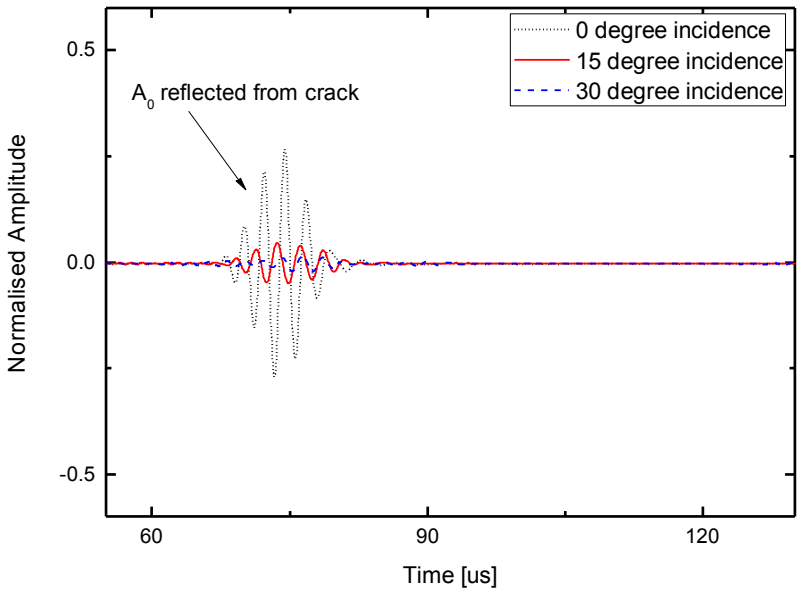

(a)

Fig. 2.5. (a) Crack-reflected A_0 modes (residual signals) acquired via typical sensing paths $A_1 - S_1$ ($\theta = 0^0$), $A_2 - S_2$ ($\theta = 15^0$) and $A_3 - S_3$ ($\theta = 30^0$) from FE simulation (showing signal fragments containing damage-reflected A_0 mode only; normalised by the magnitude of corresponding incident waves); and (b) envelopes of energy distribution of signals shown in (a) obtained using HT-based signal processing

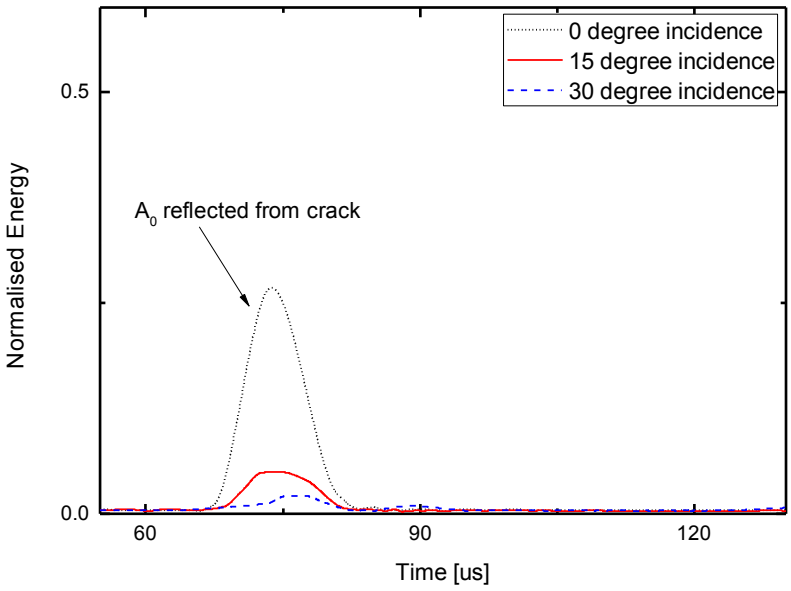

(b)

Fig. 2.5. *Cont.*

In the HT-processed signals, the peak value of the envelope of energy distribution was defined as the intensity of the damage-reflected wave in the following. Taking into account seven sensing paths, a correlation between the intensity of crack-reflected signal energy and angle of wave incidence relative to the crack orientation was obtained, shown in Fig. 2.6. It can be seen that the strongest reflection from crack is captured via $A_1 - S_1$ (normal incidence, $\theta = 0^0$); with the increase of incidence angle, the intensity of crack-reflected signal energy decreases monotonously and reaches its minimum when $\theta = 90^0$; remarkable decrease takes when $\theta < 30^0$, whereas no significant decrease can further be observed when $\theta > 30^0$.

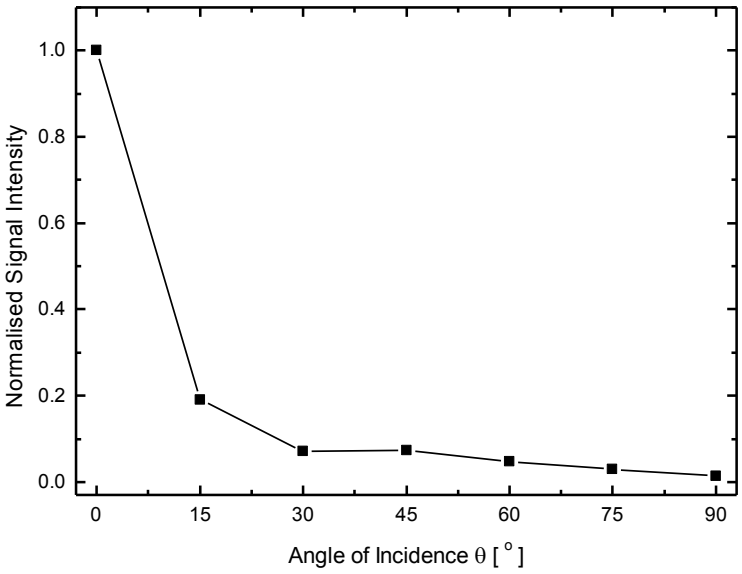

Fig. 2.6. Intensity of signal energy reflected by a crack vs. angle of wave incidence from FE simulation

To further explore the influence of damage severity on the above established relationship, the crack length was varied from 10 to 30 mm with an increment of 2 mm. The linkages between the intensity of crack-reflected signal energy and angle of wave incidence were obtained, exhibited in Fig. 2.7. It can be seen that at a given angle of incidence, the intensity of signal energy reflected by a longer crack is slightly stronger than that by a shorter crack, although certain fluctuation of such a trend can be noticed. However the discrepancy due to crack length in the discussed variation range (10 to 30 mm, *i.e.*, 1.5-4.5 times the wavelength of the selected A_0 mode) is insignificant and would not lead to evident difference in identification results.

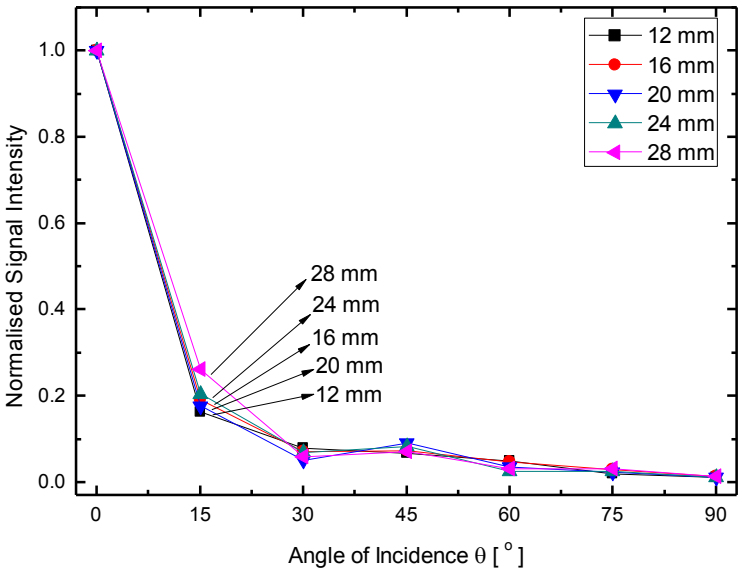

Fig. 2.7. Intensity of signal energy reflected by cracks of different lengths vs. angle of wave incidence from FE simulation

2.3.2 Experimental Validation

Experiments were conducted to validate the above FE simulation using the same configurations. The specimen was photographed in Fig. 2.8, where 16 circular PZT wafers (nominal diameter: 5 mm, thickness: 0.5 mm each) with material properties detailed in Table 2.1 were surface-mounted on the plate using a thin layer of two-component epoxy adhesive. The adhesive is conductive, making the transducers be grounded and eliminating the need for additional electrodes. A lead wire was soldered onto the top surface of each PZT wafer to serve as signal wire. Shielded wires and standard BNC connectors were used to minimise measurement noise. The 16 mm long through-thickness crack was subsequently introduced into the aluminium plate using a fine blade (0.64 mm wide).

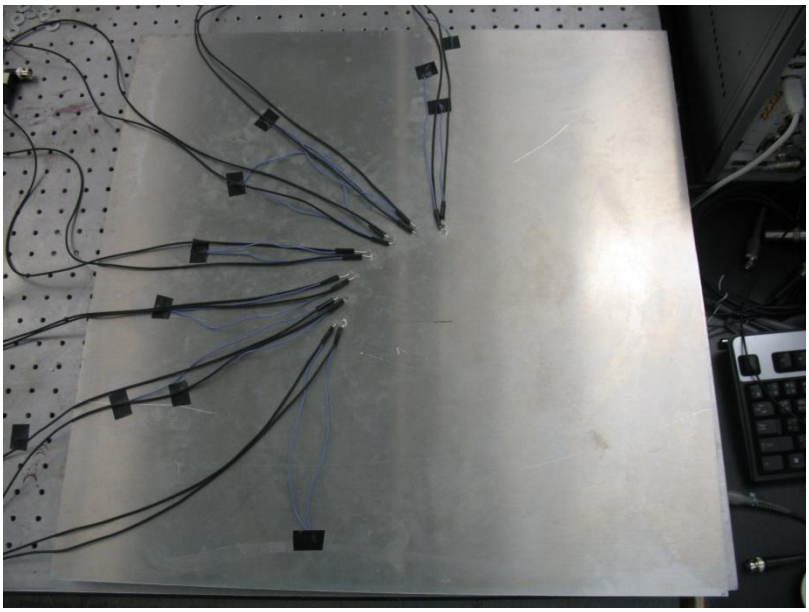

Fig. 2.8. The aluminium specimen containing a through-thickness crack and seven PZT actuator-sensor pairs

Table 2.1. Material properties of the PZT wafer used for active sensor network

Product name	PI 151
Diameter	5 mm
Thickness	0.5 mm
Density	7.80 g/cm^3
Poisson's ratio	0.31
Charge constant d_{31}	-170×10^{-12} m/V
Charge constant d_{33}	450×10^{-12} m/V
Relative dielectric constant	1280
Dielectric permittivity p_0	8.85×10^{-12} Fm^{-1}
Young's modulus E	66 GPa

The aluminium specimen was instrumented with a signal generation and acquisition system developed on a *VXI* platform [101], shown schematically in Fig. 2.9. The excitation signal, the same as the one used in simulation, was generated by a waveform generator (Agilent® E1441) and amplified using a linear signal amplifier (PiezoSys® EPA-104) to 60 $V_{p\text{-}p}$, which was then applied on each PZT actuator in turn to activate the diagnostic wave. The crack-reflected wave signals were acquired via each sensing path using an oscilloscope (HP™-54810A) at a sampling rate of 25 MHz.

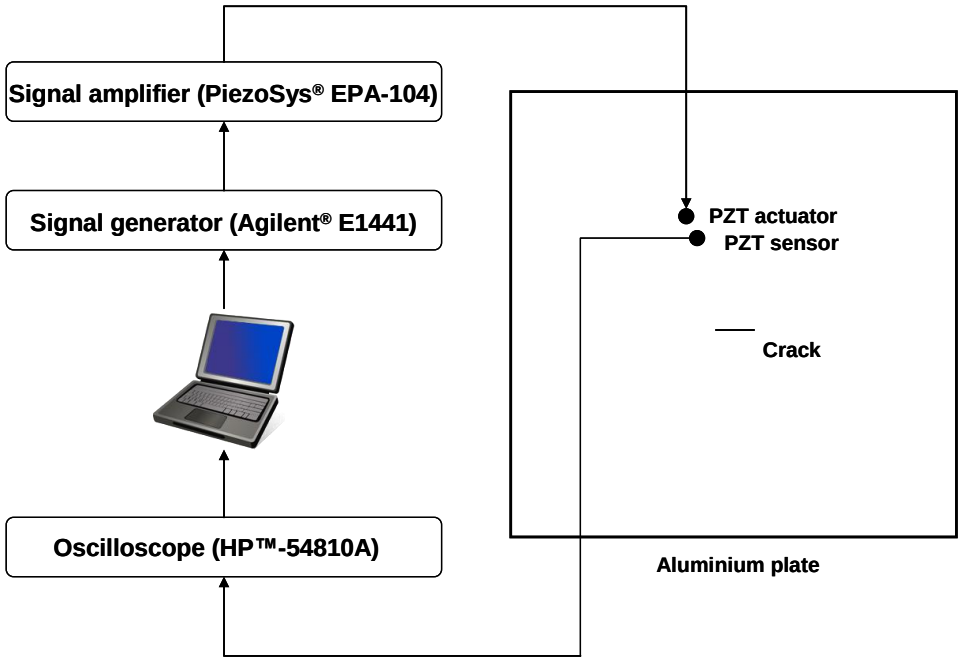

Fig. 2.9. Schematic of experimental setup

As typical results of experiment, crack-reflected wave signals, the residual signals upon subtracting corresponding baseline signals from current signals, acquired via three representative sensing paths, $A_i - S_i$ ($i = 1,\ 2,\ 3$; *i.e.*, $\theta = 0^0$, $\theta = 15^0$ and $\theta = 30^0$, respectively), are exhibited in Fig. 2.10, together with their corresponding

HT-processed counterparts.

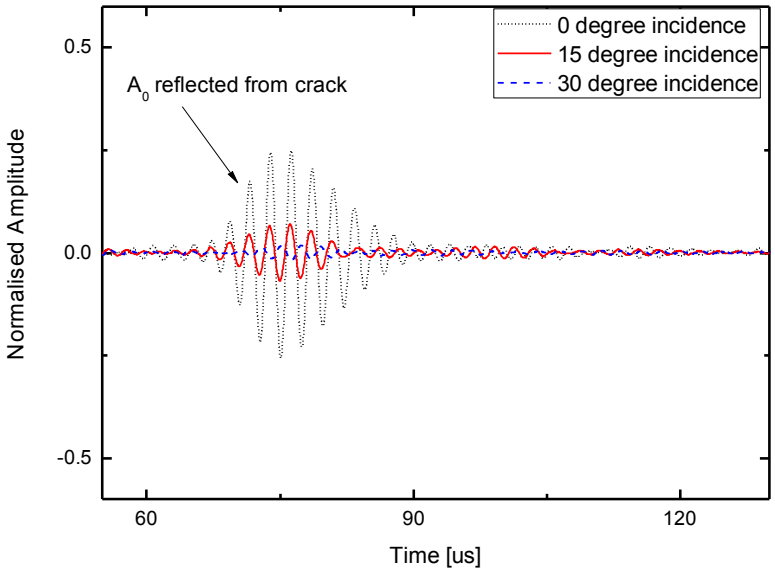

(a)

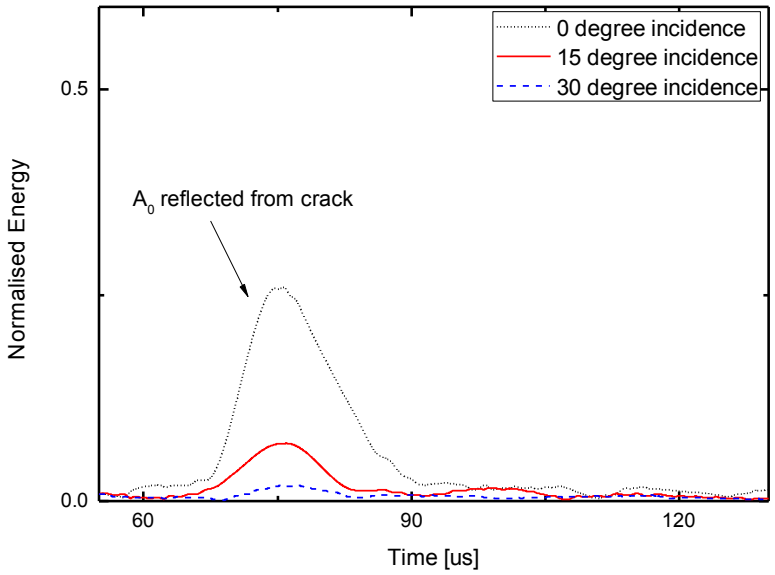

(b)

Fig. 2.10. (a) Crack-reflected A_0 modes (residual signals) acquired via typical sensing paths $A_1 - S_1$ ($\theta = 0^0$), $A_2 - S_2$ ($\theta = 15^0$) and $A_3 - S_3$ ($\theta = 30^0$) from experiment (showing signal fragments containing damage-reflected A_0 mode only; normalised by the magnitude of corresponding incident waves); and (b) envelopes of energy distribution of signals shown in (a) obtained using HT-based signal processing

Similarly, dependence of the intensity of crack-reflected signal energy on the angle of wave incidence was ascertained, plotted in Fig. 2.11. Results from the experiment (Figs. 2.10 and 2.11) can be seen to match well those from FE simulation (Figs. 2.5 and 2.6), providing consistent correlation between scattering characteristics of the crack-reflected A_0 mode and angle of wave incidence (Figs. 2.6 and 2.11).

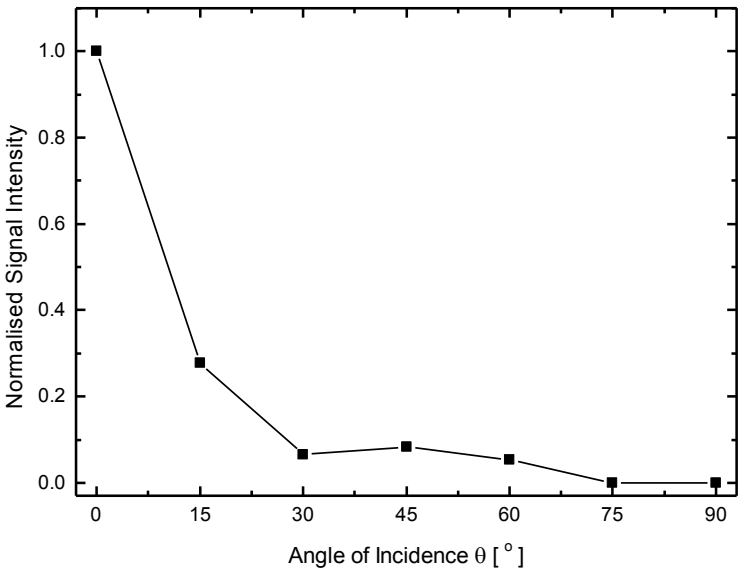

Fig. 2.11. Intensity of signal energy reflected by a crack versus angle of wave incidence from experiment

To further investigate the influence of excitation frequency on the above established relationship, the experiment was repeated in a sweep frequency range from 350 to 550 kHz with an increment of 50 kHz. The accordingly obtained linkages between the intensity of crack-reflected signal energy and angle of wave incidence are shown in Fig. 2.12 for several representative frequencies. It can be noticed that at a given angle of

incidence, the intensity of crack-reflected wave at a higher frequency is slightly weaker (in another word more prominent loss of energy included in the crack-reflected waves relative to a normal incidence case) than that reflected by the same crack but at a lower frequency. This can be attributed to the fact that elastic waves at higher frequencies possess shorter wavelengths, presenting higher sensitivity to variation in angle of wave incidence and therefore more phenomenal changes in signal energy. Although this observation implies that different linkages should be accordingly selected for different frequencies of incident wave, the diversity in the discussed variation range (350 to 550 kHz) is not pronounced.

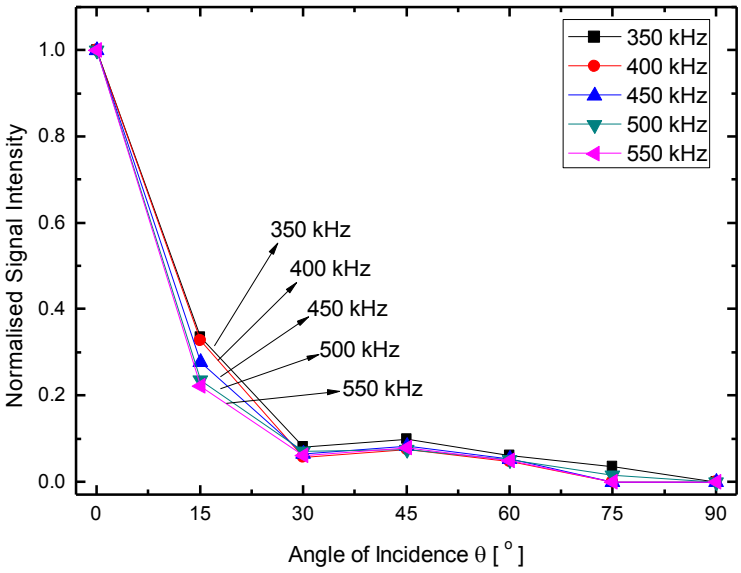

Fig. 2.12. Intensity of signal energy reflected by a crack at different excitation frequencies versus angle of wave incidence from experiment

2.4 Attenuation of Lamb Waves

The intensity of damage-scattered signal energy is subject to not only the orientation of damage as discussed previously, but also the propagation distance, a phenomenon well known as *wave attenuation*. To evaluate the damage orientation based on intensity of signal energy using the correlations described by Figs. 2.6 and 2.11, it is of vital necessity to compensate for variation in signal intensity due to wave attenuation, whereby change in signal intensity, if any, can be solely attributed to damage orientation.

To experimentally quantify this, another aluminium plate was selected (measuring $600\ \text{mm} \times 600\ \text{mm} \times 1.5\ \text{mm}$). As is shown in Fig. 2.13, five PZT wafers were surface-mounted in a straight line on the specimen, with the first one being the wave actuator and the rest being sensors (Sensors I/II/III/IV which were 100/200/320/480 mm away from the actuator, respectively). The A_0 modes captured by four sensors are combined in Fig. 2.14(a), to observe the attenuation of wave packet in a trend shown in Fig. 2.14(b).

Such an attenuation trend can be described approximately proportional to the inverse square root of the distance. Conversely, attenuation of the waves as propagation distance can be compensated in terms of

$$f'(t) = f(t) \cdot \frac{\sqrt{d}}{\sqrt{d_0}} \quad , \tag{2.1}$$

where $f'(t)$ and $f(t)$ are the compensated and original wave signals, respectively; d the propagation distance at which the wave signal is captured; and d_0 a reference distance (*e.g.*, 100 mm in this study). With Eq. 2.1, the magnitude of an acquired signal after travelling an arbitrary distance d becomes the same as that of a signal travelling a reference distance d_0 only (*i.e.*, there is no further attenuation in magnitude between distance $d - d_0$). Upon compensation, changes in the intensity of signal magnitude, if any, can solely be attributed to the variation in damage orientation. It should be noted that for a very thin aluminium plate, a good match could be achieved by ignoring material damping, as seen in Fig. 2.14(b), due to the small material damping. But for composite materials, material damping is large and must be considered.

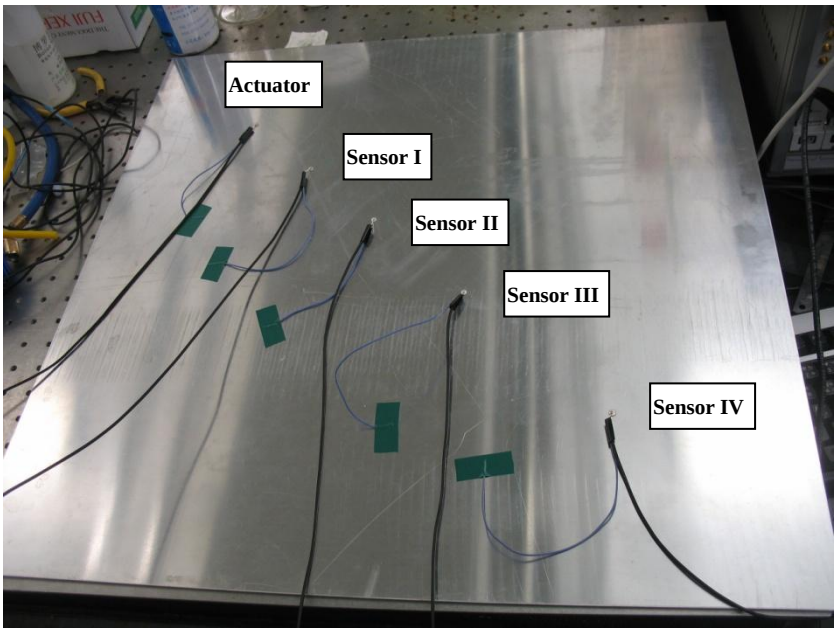

Fig. 2.13. Aluminium specimen containing five PZT wafers

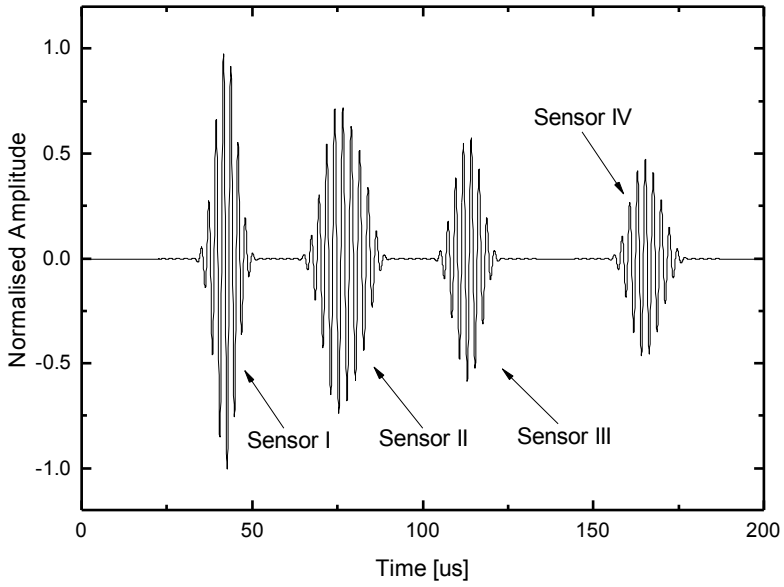

(a)

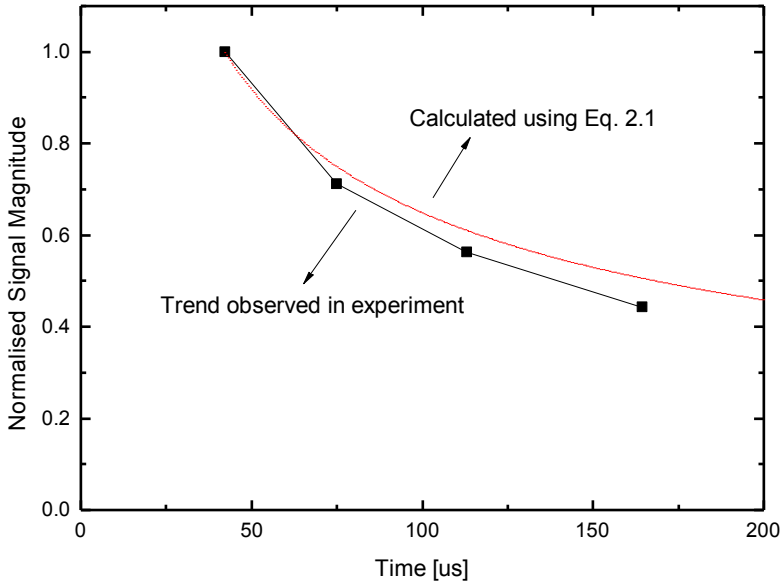

(b)

Fig. 2.14. (a) Combined Lamb wave signals (A_0 mode) propagating in an aluminium plate (1.5 mm thick) captured by sensors 100/200/320/480 mm away from the actuator (normalised by the magnitude of signal captured at 100 mm); and (b) attenuation properties of A_0 mode obtained experimentally and analytically

2.5 Influential Area of Damage on Wave Sensing Path

To perform Lamb-wave-based damage detection, a pulse signal is usually emitted across the structure under inspection and received by a sensor located appropriately. Consider a particular case which the actuator and senor are apart to form a pitch-catch sensing path ('pitch-catch' to be detailed in Section 3.1) and attached to a structure for inspection, damage in the structure can be determined by examining amplitude decrease, phase delay or dispersion captured via this sensing path in comparison with a pristine situation. It is understood that the detection using such a way considerably depends on the relative position of damage relative to the actuator-sensor sensing path. Only when the damage is located not too far away from the sensing path, can the damage be sensed. That is because the multimodal nature, dispersion and attenuation of waves make the identification of damage-scattered waves difficult. Allowing for this, it is important to explore the influential area of damage on a sensing path, *i.e.* the relationship between the distance of a defect relative to an actuator-sensor sensing path and the damaged status that this actuator-sensor path senses. In this study, both FE simulation and experimental validation were carried out to explore such correlation.

2.5.1 FE Simulation

The same aluminium plate as the one used in Section 2.3.1 (600 mm × 600 mm × 1.5 mm) was considered. A circular hole with a diameter of 20 mm was assumed at the centre of the plate, as shown in Fig. 2.15. To explore the relationship between the distance of the hole relative to an actuator-sensor sensing path and the damaged status that this actuator-sensor path can sense, seven actuator-sensor paths, $A_i - S_i$ ($i = 1,\ 2,\ \cdots,\ 7$), were formed by using 14 PZT wafers, having the distance to the hole centre as 0, 6, 12, 18, 24, 30, 36 mm, respectively. The locations of individual PZT wafers are tabulated in Table 2.2. For each actuator-sensor path, the distance between the actuator and the sensor was 200 mm.

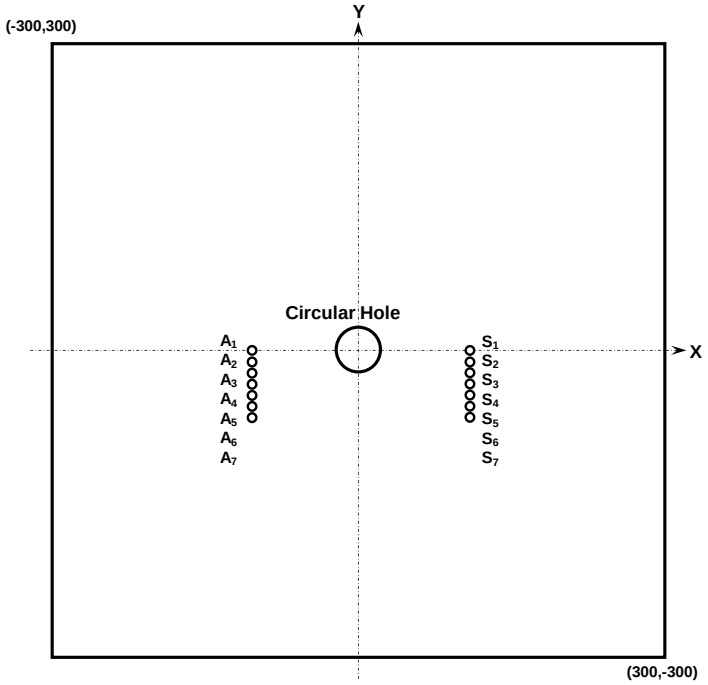

Fig. 2.15. An aluminium plate containing a circular hole and seven actuator-sensor sensing paths (unit: mm)

Table 2.2. Coordinates of centre locations of PZT wafers

Actuator	Coordinates [mm]	Sensor	Coordinates [mm]
A_1	(-100, 0)	S_1	(100, 0)
A_2	(-100, -6)	S_2	(100, -6)
A_3	(-100, -12)	S_3	(100, -12)
A_4	(-100, -18)	S_4	(100, -18)
A_5	(-100, -24)	S_5	(100, -24)
A_6	(-100, -30)	S_6	(100, -30)
A_7	(-100, -36)	S_7	(100, -36)

The plate was meshed using three-dimensional eight-node brick elements. The hole in the plate was formed by eliminating corresponding FE elements in the location of hole from the plate model, as shown in Fig. 2.16. The same input signal as the one used in Section 2.3.1 (shown in Fig. 2.2) was re-called as excitation signal, numerically generated by recalling the PZT actuator model introduced in Section 2.3.1. In order to examine the influential area of the damaged zone on different wave modes, both the S_0 and A_0 modes were activated by the PZT actuator model. Dynamic simulation was executed using ABAQUS®/EXPLICIT, in which the transmitted wave signals were acquired by calculating the strains at sensor locations.

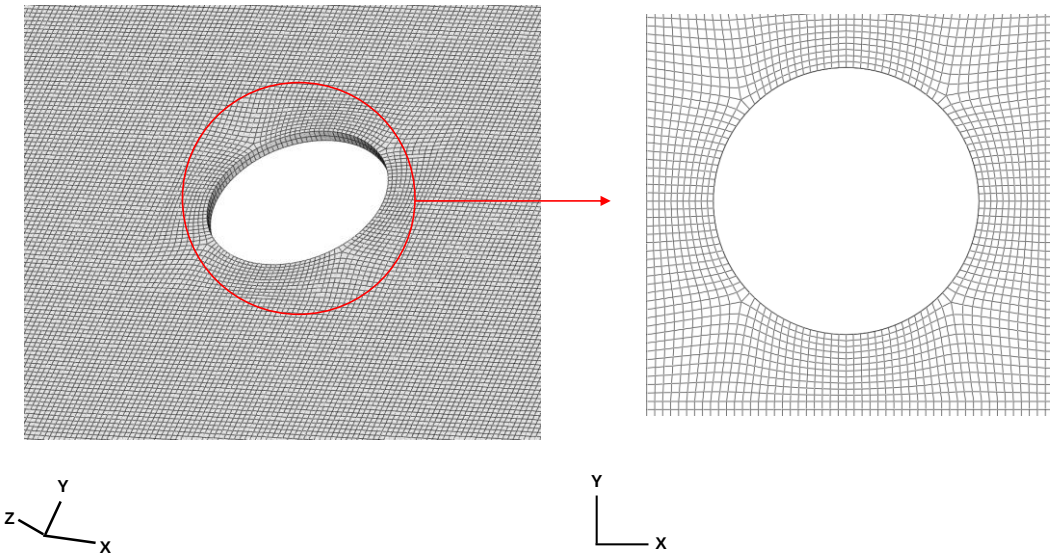

Fig. 2.16. Partial FE model of the aluminium plate shown in Fig. 2.15 with zoomed-in part containing a circular hole

Typical transmitted wave signals captured via $A_2 - S_2$ are displayed in Fig. 2.17(a). The captured signals were normalised relative to the magnitude of directly arrived A_0 wave from captured at an intact situation, and then processed with HT-based signal processing (Eq. 1.4), to obtain the energy distribution of the signal, in Fig. 2.17(b). It is observed that both the magnitudes of the S_0 and A_0 modes in the current signal are weaker than those in corresponding baseline signal. Such a reduction in magnitude can be attributed to the fact that $A_2 - S_2$ right passes through the hole and the wave signal captured via this sensing path is modulated significantly by the damage.

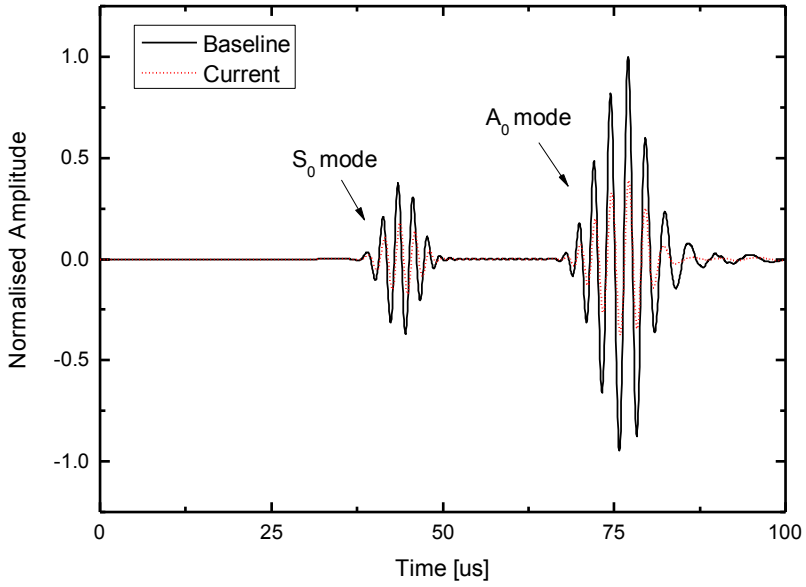

(a)

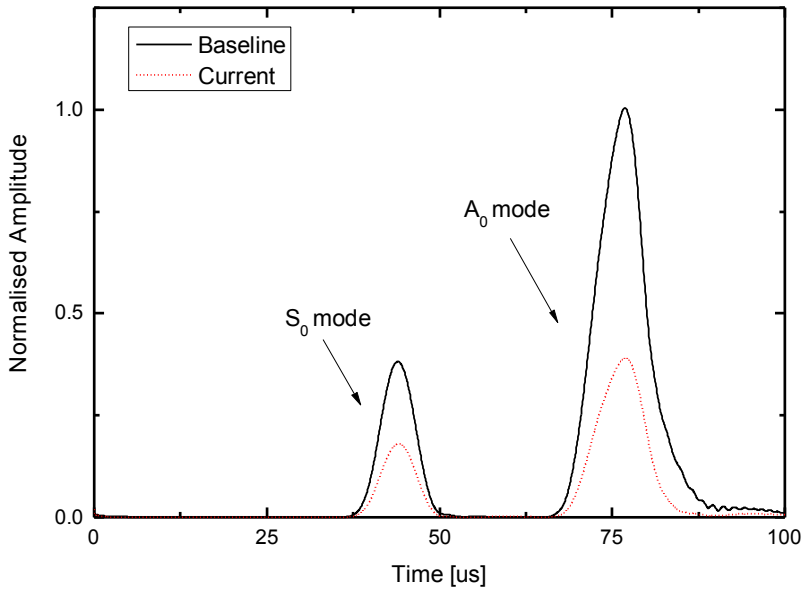

(b)

Fig. 2.17. (a) Lamb wave signals acquired via sensing path $A_2 - S_2$ from FE simulation; and (b) envelopes of energy distribution of signals shown in (a) obtained using HT-based signal processing (normalised by the magnitude of A_0 mode)

2.5.2 Experimental Validation

Experiments were in parallel conducted using the configurations same as those in FE simulation. The aluminium specimen is exhibited in Fig. 2.18, where 14 circular PZT wafers with material properties detailed in Table 2.1 were surface-installed on the plate, and a circular hole with a diameter of 20 mm was drilled at the centre. The aluminium specimen was instrumented with the same signal generation and acquisition system used in Section 2.3.2.

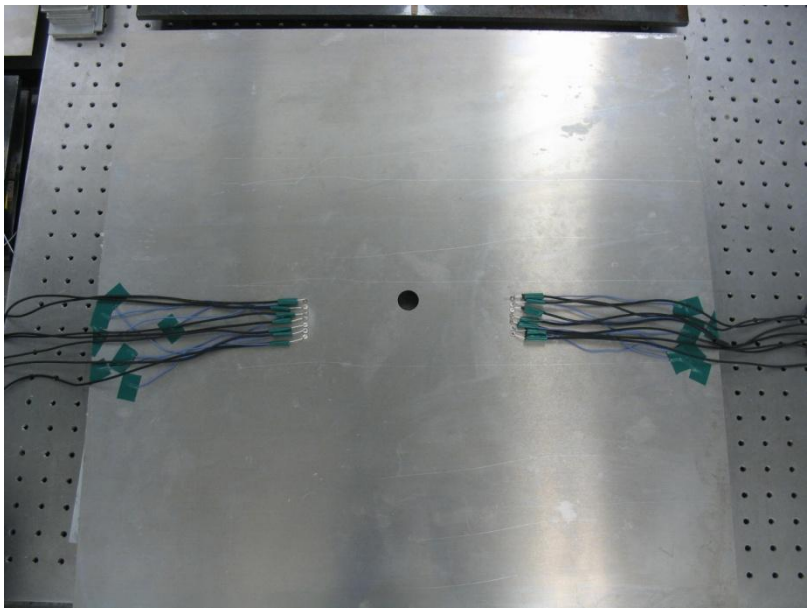

Fig. 2.18. Aluminium specimen containing a circular hole and seven PZT actuator-sensor paths

Same as the simulation, the captured transmitted wave signals via $A_2 - S_2$ are displayed in Fig. 2.19, together with their corresponding HT-processed counterparts. Results from experiment (Fig. 2.19) can be seen to match well those from FE

simulation (Fig 2.17).

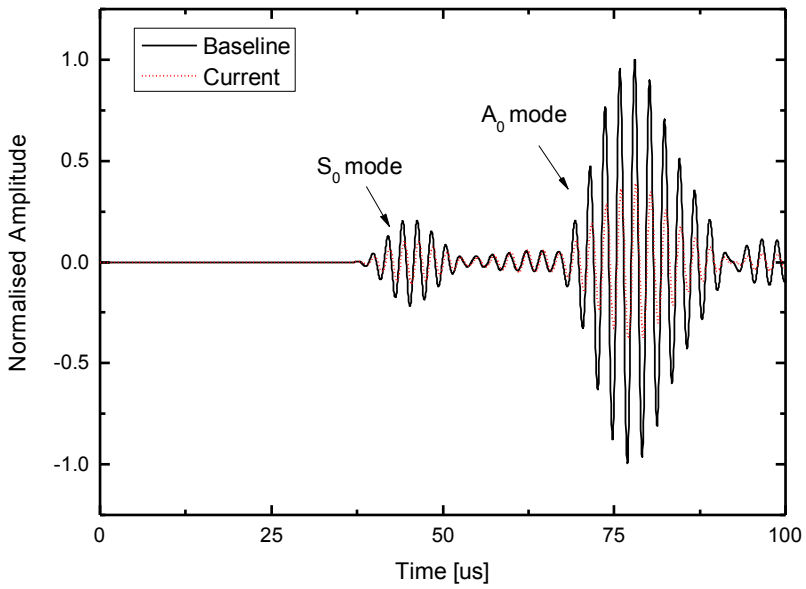

(a)

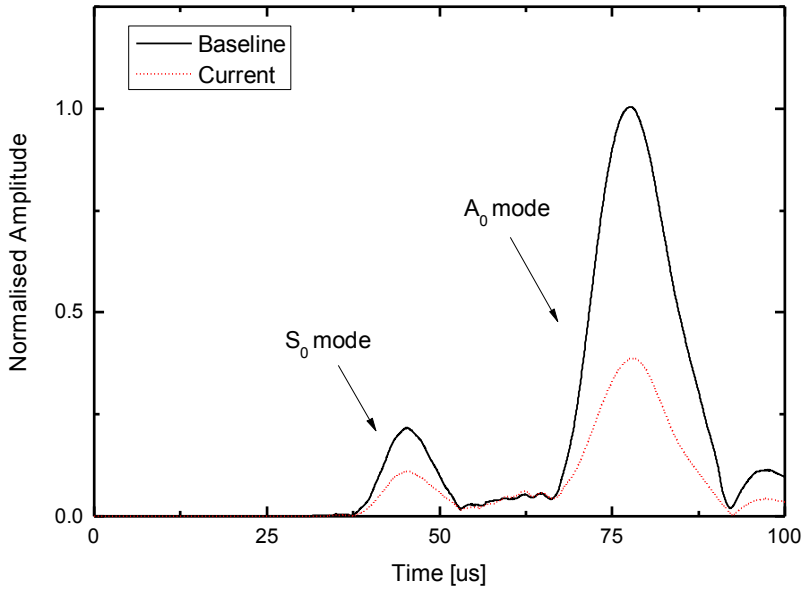

(b)

Fig. 2.19. (a) Lamb wave signals acquired via sensing path $A_2 - S_2$ from experiment; and (b) envelopes of energy distribution of signals shown in (a) obtained using HT-based signal processing (normalised by the magnitude of A_0 mode)

2.5.3 Discussions

To quantify damaged status that a certain actuator-sensor path can sense, a damage index (DI) was defined, as,

$$DI = \left| \frac{\Xi_{baseline} - \Xi_{current}}{\Xi_{baseline}} \right| , \quad \textbf{(2.2)}$$

where $\Xi_{baseline}$ and $\Xi_{current}$ are intensities of wave signals (peak value of HT-processed signal) acquired from pristine and current situation, respectively. The larger the DI is, the higher the possibility of a damage existing on this actuator-sensor sensing path. DIs of the seven actuator-sensor paths, $A_i - S_i$ ($i = 1,\ 2,\ \cdots,\ 7$), were calculated using Eq. 2.2. The correlation between the DI of a certain actuator-sensor path and the distance of this sensing path relative to the hole centre was subsequently obtained and exhibited in Fig. 2.20. A circle is plotted in the figures to show the size of the hole, from which the hole centre is located at the origin.

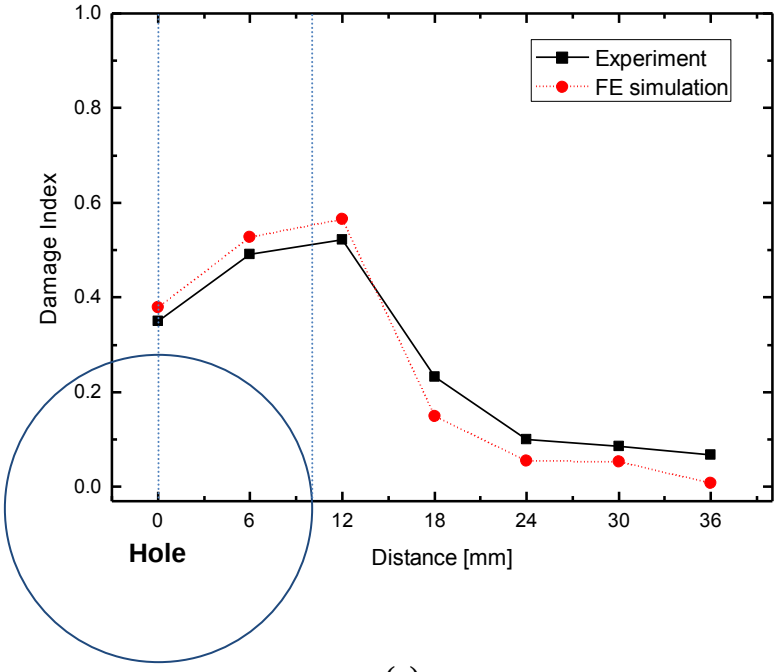

(a)

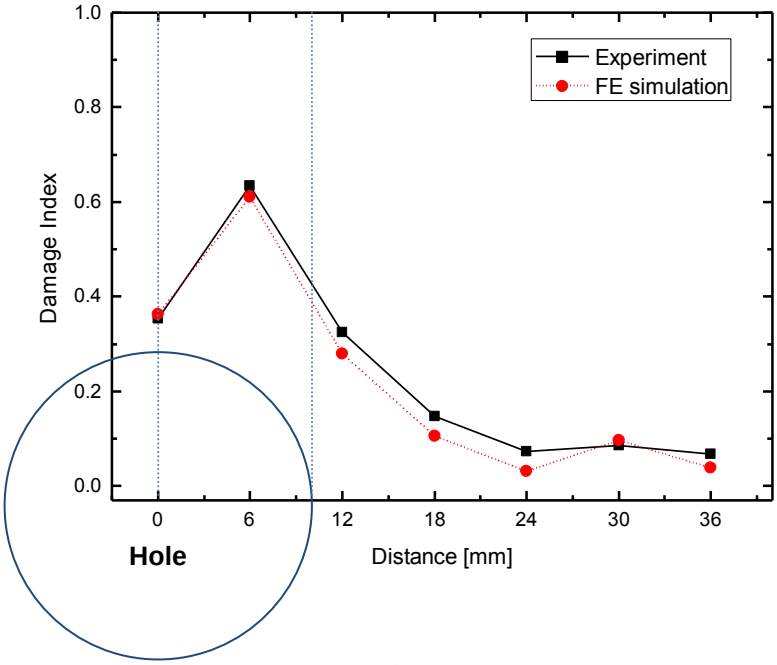

(b)

Fig. 2.20. Variation of DI against the distance between the hole centre and actuator-sensor sensing paths for (a) S_0 mode and (b) A_0 mode (excitation frequency: 450 kHz)

It can be seen that when the sensing path right passes through the centre of the hole, DI is relatively large (over 0.3). With the increase of the distance, DI increases as well until it reaches a certain extreme value. Subsequently, DI decreases gradually until it drops to a certain value (around 0.1). Then, DI fluctuates slightly. Both S_0 mode and A_0 mode present a similar tendency, whereas slightly different.

To further investigate the influence of the frequency on the above established relationships for both wave modes, the FE simulation was repeated in a sweep frequency range from 350 to 500 kHz with an increment of 50 kHz. The accordingly obtained linkages between the DI of a certain actuator-sensor sensing path and the distance of this sensing path relative to the hole centre are shown in Fig. 2.21 for several representative frequencies. It can be observed that, for both S_0 and A_0 modes, variation in excitation frequencies does not influence such linkages prominently. It is noted that DI at a higher frequency decreases more rapidly than that at a lower frequency. This can be attributed to the fact that elastic waves at higher frequencies possess shorter wavelengths, presenting higher sensitivity to variation in distance away from the damage and therefore more phenomenal changes in signal energy.

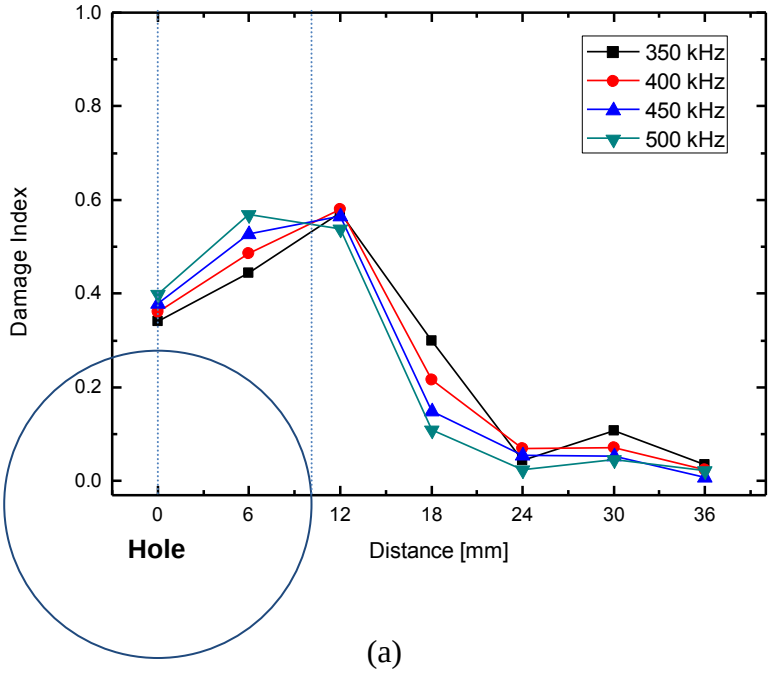

(a)

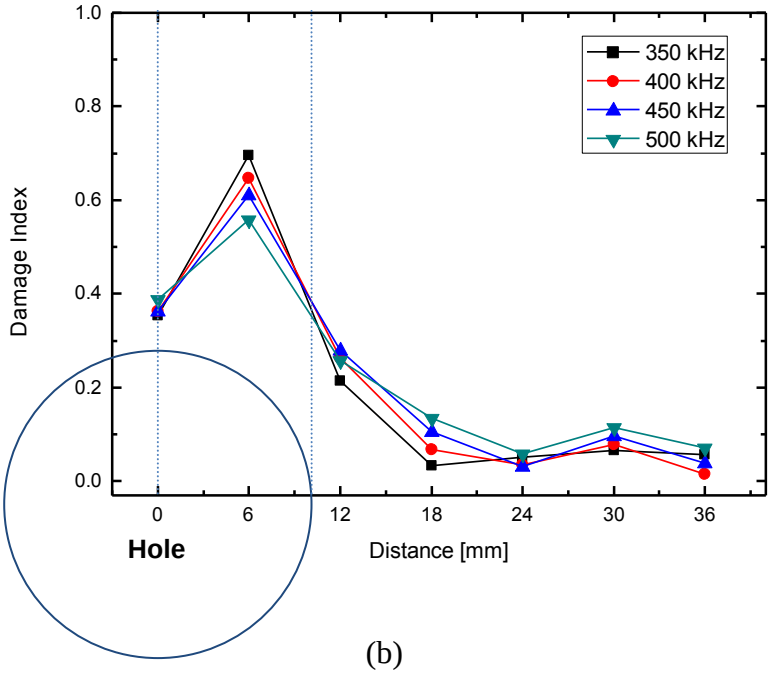

(b)

Fig. 2.21. Variation of DI against the distance between the hole centre and actuator-sensor sensing paths for (a) S_0 mode and (b) A_0 mode at different excitation frequencies from FE simulation

From the above observations, it can be seen that the correlation between DI and the distance of a sensing path to the damage is somewhat complicated within the damage area. However, what we are most concerned in this study is the influential area that a sensing path holds (this will be addressed in Section 4.2.2). Inside the influential area, DIs feature relatively large values, benefiting identification of damage; while beyond the influential area, DIs relatively small, posing difficulty on damage detection.

To further quantify such an influential area with regard to the wavelength of the Lamb wave, a threshold of the DI for a clear identification of damage was introduced, below which the captured DI was deemed too small to characterise the damage, while over which the DI was sufficiently large to depict the damage explicitly. Using the discussed hole as an example for illustration, such a threshold was set as 0.2, as indicated in Fig. 2.22 for two concerned wave modes. At this threshold ($DI = 0.2$), the distances are 19.4 mm and 16.2 mm for S_0 and A_0 modes, respectively. It is proper to use the distance between the sensing path and the fringe of the hole rather than the hole centre because it is the fringe of the damage that first scatters incident waves. In this case, when $DI = 0.2$, the distances between the fringe of hole and the sensing paths for two wave modes are $19.4 - 10 = 9.4\,mm$ for S_0 mode, and $16.2 - 10 = 6.2\,mm$ for A_0 mode. Interestingly, the influential area for S_0 mode, 9.4 mm, is close to the S_0 mode wavelength, 11.8 mm; while the influential area for A_0 mode, 6.2 mm, is close to the A_0 mode wavelength, 6.7 mm. (It should be noted that,

the threshold value of 0.2 is only for this case, *i.e.* a circular hole. Since different types of damage modulate wave field in different ways, different threshold values may be selected for different types of damage.)

Conclusion can thus be drawn that (a) as a rule of thumb, the influential area of a damaged zone on a particular sensing path is comparable to the wavelength of the wave propagating along this sensing path; and (b) the S_0 mode seems to have a relatively larger influential region than A_0 mode.

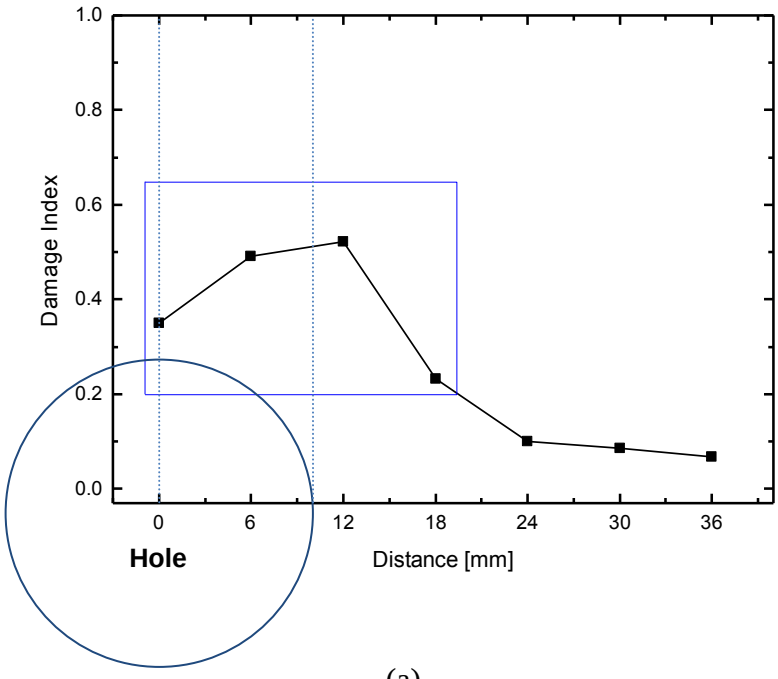

(a)

Fig. 2.22. Influential area for an actuator-sensor sensing path to detect damage using (a) S_0 mode and (b) A_0 mode at the excitation frequency of 450 kHz from experiment (encircled by rectangles)

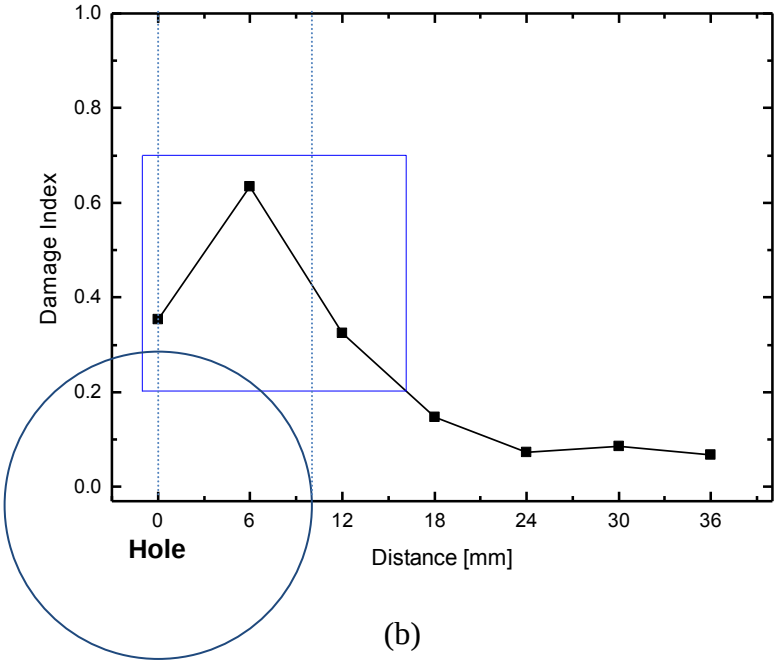

(b)

Fig. 2.22. *Cont.*

2.6 Concluding Remarks

In this chapter, three fundamental studies were performed, *i.e.*, a) Effect of the orientation of damage with sizable length in a particular dimension (orientation-specific damage) on Lamb wave propagation was scrutinised quantitatively, b) attenuation of Lamb wave was calibrated and compensated, and c) influential area of damage on wave sensing path was investigated. Investigations lead to the following conclusions: a) crack orientation has a prominent influence on Lamb wave propagation, in which strongest reflection is captured with normal incidence, and with the increase of angle of wave incidence, the intensity of crack-reflected signal

energy quickly decreases. Thus, the intensity of damage-reflected wave energy can be a sensitive indicator to damage orientation. b) Lamb waves in a thin aluminium plate attenuate at a rate that is approximately proportional to the inverse square root of the propagation distance. c) The influential area of a damaged zone on a particular sensing path is comparable to the wavelength of the wave propagating along this sensing path. The scrutinised correlations are applied to develop novel diagnostic imaging approaches in the following chapters.

CHAPTER 3 Probability-based Diagnostic Imaging Using Pulse-echo Configuration

3.1 Introduction

Pulse-echo and pitch-catch are two configurations commonly used in damage identification. In the former, after exciting the structure with a very narrow bandwidth pulse, a sensor collocated with the actuator is used to 'listen' to the echoes of the pulse scattered back from the discontinuities existing in the wave propagation path, to acquire time-of-flights (ToFs) or signal magnitude of the echo waves. From the captured echo wave signals, defects can be located using the conventional triangulation with known wave propagation speed. In the latter, a pulse signal is sent across the specimen under inspection and a sensor at far field of the specimen receives the damage-scattered signal. Based on various wave scattering characteristics such as delay in time of transit, reduction in signal amplitude and change in phase, information about the scattering source (*i.e.*, damage) can be obtained.

In this chapter, the former configuration offered by an active sensor network was considered first to develop a probability-based diagnostic (PDI) technique. In the approach, based on the established correlations between (1) damage location and ToFs extracted from echo signals, and (2) intensity of signal energy echoed back by damage and damage orientation, a PDI approach was developed. The effectiveness of this approach was then demonstrated by predicting selected orientation-specific damage including a triangular through-thickness hole (through FE simulation) and a through-thickness crack (through experiment) in aluminium plates. Relying on the signal feature including both the temporal information and signal intensity, and with the assistance of a two-level synthetic image fusion scheme, this PDI approach is capable of indicating the orientation of individual damage edges clearly and further the shape of damage, apart from the location of the damage.

3.2 Principle

In a PDI approach, the planar area of an inspected structure is first meshed and projected to an image, each image pixel corresponding exclusively to a spatial point of the structure. The value of an image pixel is termed *field value* in what follows, which can be linked to the probability of damage presence at the spatial point of the structure corresponding to that pixel, using appropriately selected signal features. Establishing an appropriate field value is the crucial step in PDI methods.

3.2.1 ToF-based Field Value

In a probability image, a field value at a pixel can be calculated or defined using signal features appropriately extracted from signals (*e.g.*, ToF, signal magnitude, signal energy). In particular, ToF, defined as the time consumed for a wave to travel a certain distance [36], is one of the most straightforward features of a wave signal.

In this study, ToF extracted from damage-echoed wave signals was used first to define the field value. To brief its principle, consider a PZT sensor network consisting of N pulse-echo pairs as shown in Fig. 3.1(a). Two neighboring PZT wafers form a pulse-echo sensing path, denoted by $A_i - S_i$ ($i = 1,\ 2,\ \cdots,\ N$), with A_i serving as the wave actuator and at the same time its neighboring PZT wafer S_i serving as sensor. Without losing the generality, focusing on a pulse-echo path, $A_i - S_i$, a local coordinate system can be established for this path as shown schematically in Fig. 3.1(b), where the origin is at the centre of actuator A_i and sensor S_i, and the damage is presumed to be at (x_D, y_D) (two unknown variables to be determined). With the assumption that wave propagation velocity V is constant before and after interacting with damage (a more general scenario in which the velocity of damage-scattered wave is different from that of incident wave due to mode conversion can be referred to elsewhere [88]), a series of equations can be established for all individual pulse-echo paths in this sensor network, as

$$\frac{L_{A_i-D} + L_{D-S_i}}{V} = \Delta t_i \qquad (i = 1,\ 2,\ \cdots,\ N), \qquad \textbf{(3.1)}$$

where Δt_i is the sum of (i) ToF for the incident wave to propagate from actuator A_i to the damage, and (ii) ToF for the damage-reflected wave to propagate from damage to sensor S_i. L_{A_i-D} and L_{D-S_i} represent the distances between actuator A_i and damage at (x_D, y_D), and the damage and sensor S_i, respectively. Because the distance between A_i and S_i is much smaller than L_{A_i-D} and L_{D-S_i}, it can be hypothesized that $L_{A_i-D} = L_{D-S_i} = \sqrt{x_D{}^2 + y_D{}^2}$. Mathematically, Eq. 3.1 depicts a series of circle-like locus which is the prior perceptions regarding the presence of damage from the perspective of the pulse-echo path that creates such a locus.

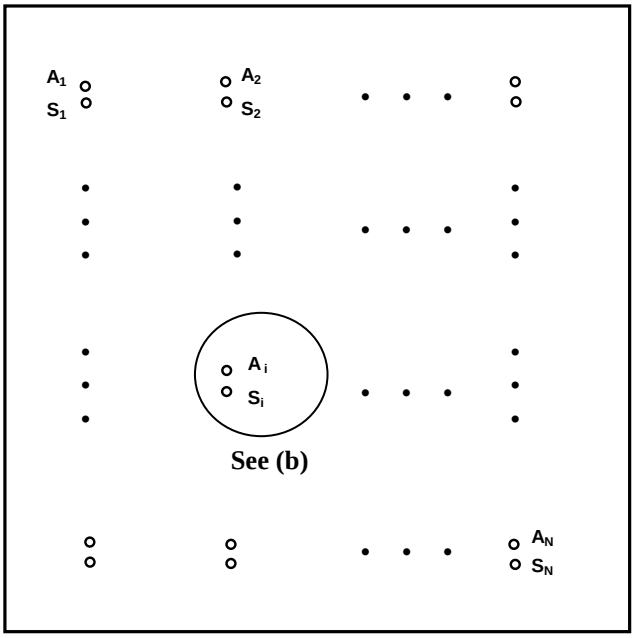

(a)

Fig. 3.1. (a) An active sensor network consisting of N pulse-echo pairs; and (b) relative positions among actuator A_i, sensor S_i and damage in the local coordinate system for pulse-echo path $A_i - S_i$

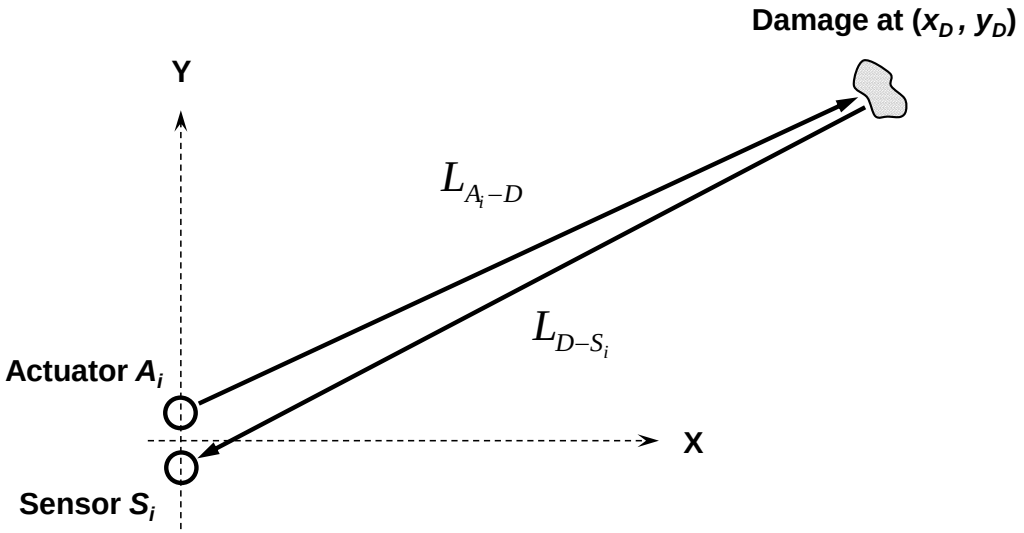

(b)

Fig. 3.1. *Cont.*

It should be mentioned that traditional damage detection approaches using ToF is based on seeking the intersections of more than two loci established by different actuator-sensor paths [36], as illuminated schematically in Fig. 3.2. However, in our approach, in order to develop field value at each pixel of the probability image, no attempt was made at this stage to locate the damage using traditional approaches.

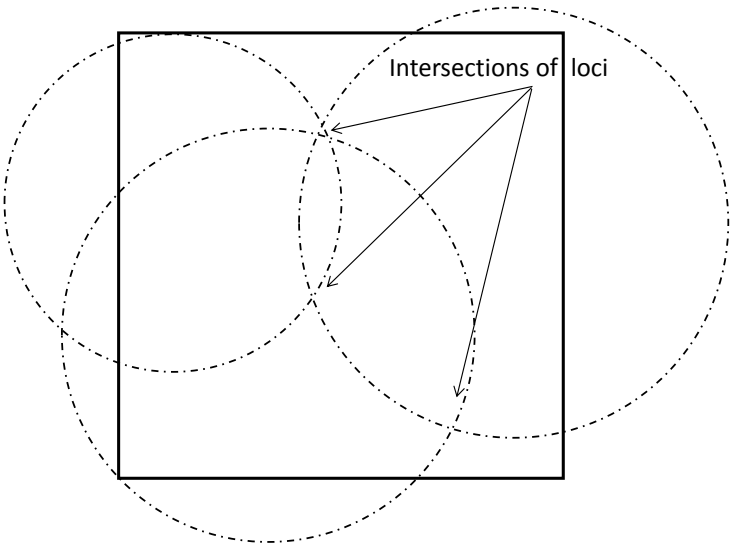

Fig. 3.2. Traditional damage detection procedures by seeking intersections of different loci

In the present approach, for a plate-like structure under inspection to which the above active sensor network is attached, the structure can be meshed using $L \times K$ nodes virtually (each mesh node exclusively corresponds to a pixel of the probability image). At every single node, probabilities concerning damage presence perceived by individual pulse-echo paths can be quantified in terms of the loci attained using Eq. 3.1: in principle, the nodes that rightly locate on a particular locus have the highest degree of probability (100%) of damage presence from the perspective of the pulse-echo path that produces such a locus; for other nodes, the further the distance to this locus, the lower the probability that damage exists at those nodes. Therefore, the distance from a particular mesh node to the loci defined by Eq. 3.1 can be associated with the probability of damage at the node. In the approach, a *cumulative distribution function* (CDF), $F(z)$, was introduced to define the probability as [87],

$$F(z)=\int_{-\infty}^{z} f(z_i)\cdot dz_i, \tag{3.2}$$

where $f(z_i)=\frac{1}{\sigma_i\sqrt{2\pi}}\exp[-\frac{z_i^{\,2}}{2\sigma_i^2}]$ is the *Gaussian distribution function*, representing the probability density of damage presence at mesh node (x_m, y_n) ($m=1,\ 2,\ \cdots,\ L$; $n=1,\ 2,\ \cdots,\ K$) established by pulse-echo path A_i-S_i . $z_i=\sqrt{(x_i-x_m)^2+(y_i-y_n)^2}$, where (x_i, y_i) is the location on the locus established by A_i-S_i that has the shortest distance to (x_m, y_n), as explained in Fig. 3.3. σ_i is the standard variance which describes the variability or dispersion of a data set. In this study, σ_i was carefully set as 0.44 based on a series of trials. Thus the field value at node (x_m, y_n) (*i.e.*, the probability of damage presence at the point of the structure corresponding to this pixel), $I(x_m, y_n)$, perceived by sensing path A_i-S_i, is

$$I(x_m, y_n)=1-\left[F(z_i)-F(-z_i)\right]. \tag{3.3}$$

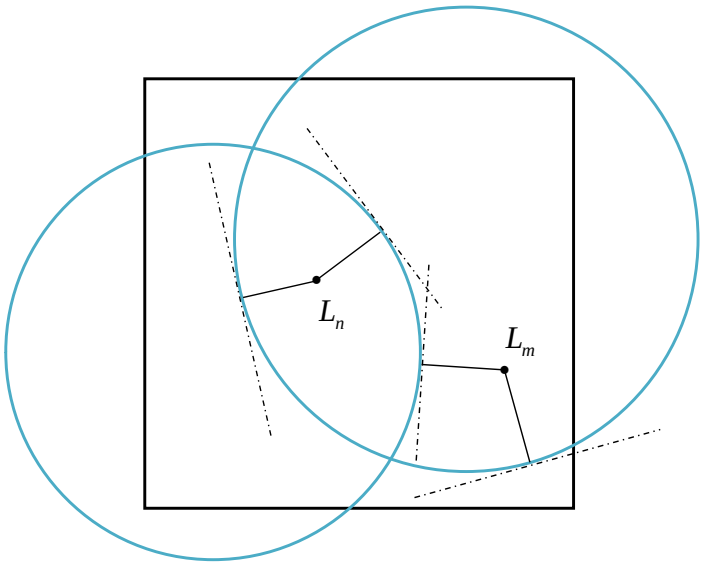

Fig. 3.3. The distances of two arbitrarily selected spatial nodes, L_m and L_n, with regard to two loci

Using such a method, field value at each pixel can be developed. Fig. 3.4 exemplarily shows such a probability image, established by a pulse-echo path using Eq. 3.3. In the image, the lighter a pixel in the greyscale image is, the greater the possibility of damage existing at that pixel.

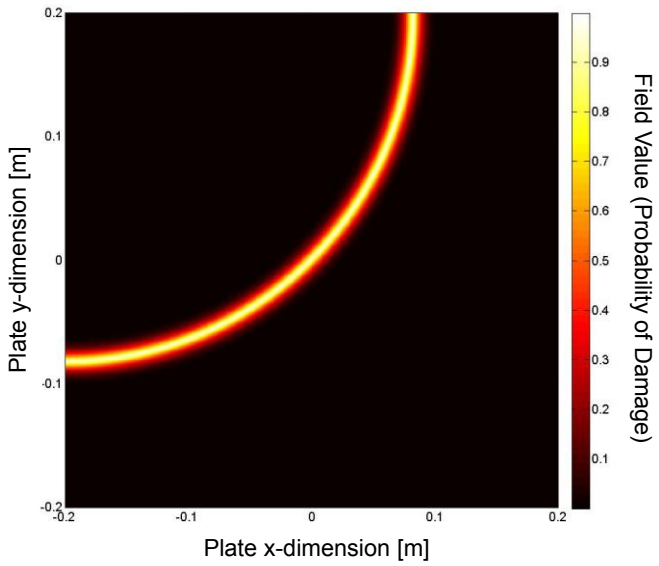

Fig. 3.4. A probability image established by a pulse-echo path

3.2.2 Retrofitted Field Value by Integrating Intensity of Signal Energy

It is debatable whether information based solely on temporal information such as ToFs extracted from signals is sufficient to deliver quantitative depiction of damage including its orientation, shape and severity. That is because difference in damage

orientation, shape and severity often impacts recognisable modulation on signal intensity, rather than on temporal information. As a compromised endeavour, one can properly select a threshold of field value to quantitatively estimate the damaged zone [75, 88, 90, 91]: when the probability at a pixel is greater than the threshold, it is estimated that this pixel is contained in the damaged zone, and by this means shape of the damaged zone can be approximately defined by keeping pixels with field values higher than the threshold only. With such a philosophy, the probability image is most likely able to highlight the locations of both damage tips (*e.g.*, two tips of a crack) because the damage tip is the major source of wave scattering. The crack length can further be ascertained by calculating the distance between two major scattering sources [75]. For detecting damage with a certain area such as delamination, added mass or debonding, the image possibly highlights edges or boundary of the damage, and the damaged area can further be approximated by drawing the smallest circle that connects the scattering sources highlighted in the image by assuming that the damage is circular. Notwithstanding there is no clear mechanism to support such a processing for portraying damage shape solely based on temporal information.

As demonstrated previously (Section 2.3), the intensity of damage-reflected wave energy can be a sensitive indicator to damage orientation relative to the angle of wave incidence (Figs. 2.6 and 2.11). Allowing for this, the field value defined by Eq. 3.3 was retrofitted by integrating extracted signal features associated with energy intensity of

signal, as below, with an attempt to quantify the damage orientation:

$$I(x_m, y_n)' = \frac{I(x_m, y_n) \times \Xi}{\Xi_{\max}}, \tag{3.4}$$

where $I(x_m, y_n)$ is the field value at pixel (x_m, y_n) obtained using Eq. 3.3; $I(x_m, y_n)'$ is the retrofitted field value at pixel (x_m, y_n); Ξ is the intensity of damage-reflected wave packet which has already been compensated for wave attenuation due to propagation distance using Eq. 2.1; $\Xi_{\max}$ is the extremum of Ξ obtained via all available pulse-echo pairs in the sensor network. Integrating (i) intensity of damage-reflected signal energy (subject to damage orientation upon compensation for wave attenuation) with (ii) temporal information (subject to location of damage), the retrofitted field value defined in Eq. 3.4 is endowed with an enhancive capacity to portray damage quantitatively including orientation of its edges, whereby damage shape can further be ascertained if the damage is deemed as the continuum of a series of cracks with various lengths.

3.3 Imaging Fusion Scheme

Based on Eq. 3.4 every single pulse-echo pair of the active sensor network contributes a probability image, called *source image*. Source images contain, however, not only damage-scattered information but unwanted features such as measurement

noise and uncertainties, multiple wave modes, reflections from structural boundaries, *etc.*, presenting complexity or even unreliable information in image appearance. To screen unwanted features and strengthen damage-associated information, different image fusion techniques have been developed.

Image fusion, *i.e.*, fusion of source images at pixel-level, leads to a resultant image through aggregating corresponding field values of individual source images appropriately. The image fusion is a route from perceptions of individual sensing paths to ultimate consensus of the whole sensor network. At a rudimental level, a resultant image can be achieved by averaging all source images. Such a simple process accentuates commonality and weakens contrast in individual source images, but it may significantly mask information which exists in only few sources, as a result of equal balance of all sources. Towards this deficiency, fusion schemes giving weighted consideration on particular sources have been preferred, as systematically summarised by Su *et al.* [87, 88].

A two-level synthetic image fusion scheme was proposed in this approach. Considering a sensor network consisting of N pulse-echo pairs**,** $A_j - S_j$ **(** $j = 1,\ 2,\ \cdots,\ N$ **),** from which each sensor S_j independently perceives a damage event with probability of *E*, described by $P(E|S_j)$. The entire sensor network contributes in total N source images. In the two-level fusion scheme, arithmetic mean

and geometric mean were first applied to fuse all available source images, respectively, to obtain two interim images, in accordance with

arithmetic mean scheme: $$P_{arithmetic}(S_1, S_2, \cdots, S_N) = \frac{1}{N}\sum_{j=1}^{N} P(E|S_j), \quad \textbf{(3.5a)}$$

geometric mean scheme: $$P_{geometric}(S_1, S_2, \cdots, S_N) = \left(\prod_{j=1}^{N} P(E|S_j)\right)^{\frac{1}{N}}. \quad \textbf{(3.5b)}$$

Subsequently, a conjunctive fusion technique [87] was applied to two interim images to obtain an ultimate resultant image, which is defined as,

$$\begin{aligned} P_{conjunctive}(S_1, S_2, \cdots, S_N) &= P_{arithmetic}(S_1, S_2, \cdots, S_N) \cap P_{geometric}(S_1, S_2, \cdots, S_N) \\ &= P_{arithmetic}(S_1, S_2, \cdots, S_N) \cdot P_{geometric}(S_1, S_2, \cdots, S_N), \end{aligned} \quad \textbf{(3.6)}$$

The conjunctive fusion process aggregates two interim perceptions to strengthen a common part in between.

As flowcharted in Fig. 3.5, such a synthetic fusion process intensifies salient features of individual source images originated from damage and simultaneously suppress less salient features in interim images such as measurement noise and uncertainties.

The motivation to develop a hybrid fusion scheme is to reap merits of different fusion schemes for maximising fusion efficiency. The arithmetic mean is able to

highlight prominence of damage-induced features in source images. However with increase of involved sensing paths (*i.e.*, more source images) such prominence can be weakened considerably because each sensing path is only sensitive to the damage near it and contributes little to perceiving damage that is relatively far away from it (due to the exponential function in Eqs. 3.3 and 3.4 for defining the field value, probability of damage presence exponentially approaches to zero as the distance increases between nodes and loci). And as a result of the nature of arithmetic mean - equally balanced average of all source images, damage, highlighted in few images contributed by sensing paths near the damage, becomes de-emphasised in the ultimate resultant image and meanwhile noise and uncertainties irrelevant to damage stand out. In contrast, the geometric mean possesses capability of de-noising since it highlights features in common only. But it might 'optimistically shrink' the likelihood of damage presence because such a fusion scheme multiplicatively processes all sources, and any low possibility in particular sources can lead to significantly low likelihood in the ultimate resultant image. The synthetic fusion exploits merits of arithmetic mean and geometric mean so as to achieve a compromise in between, by equally taking into account all perceptions and well decentralising their contribution.

The following applications to actual damage identification have demonstrated that such a two-level synthetic scheme helps enhance the robustness and tolerance of identification to measurement uncertainties and possible erroneous perceptions from

particular sensors.

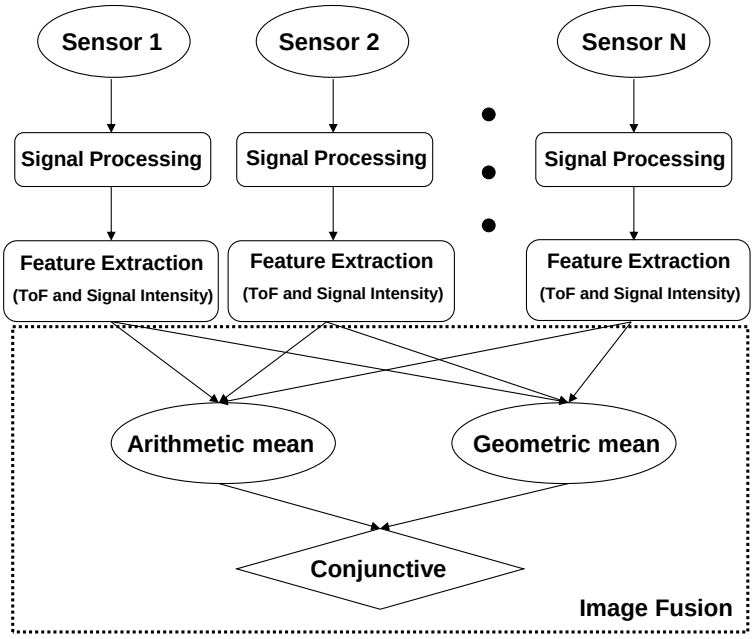

Fig. 3.5. Flowchart of the two-level synthetic image fusion scheme

3.4 Feasibility Study Using FE Simulation

To examine the feasibility of the proposed approach using retrofitted field value defined by Eq. 3.4 for quantifying location and orientation of individual damage edge, an aluminium plate (600 mm×600 mm×1.5 mm with encastre boundary conditions) was considered, bearing a triangular through-thickness hole (three edges are 20, 21 and 24 mm long, respectively), as shown in Fig. 3.6. The figure also shows eight PZT pulse-echo pairs, forming a sensor network, allocated at outer fringe of the plate, $A_i - S_i$ ($i = 1, 2, \cdots, 8$), in which A_i is 10 mm apart from S_i for each

actuator-sensor pair. The aluminium plate and PZT elements were modelled in ABAQUS®/EXPLICIT using the same modelling and simulation technique introduced in Section 2.3.1. The triangular damage was formed by removing associated FE elements from the plate model. *Hanning*-window-modulated five-cycle sinusoidal tonebursts at a central frequency of 450 kHz were respectively applied on FE nodes of the upper and lower surfaces of each PZT actuator model in the out-of-plane direction to generate the A_0 mode dominantly (Fig. 2.4(b)). The damage-scattered wave signals were captured by calculating the strains at places where eight sensors were located.

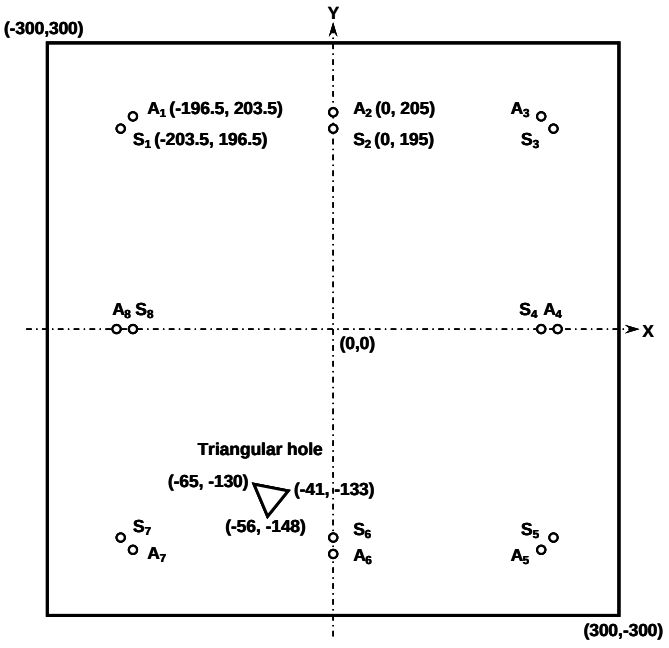

Fig. 3.6. Specimen configurations for identifying a triangular through-thickness damage in FE simulation (unit: mm) (allocation of PZT elements in the sensor network being symmetric relative to $x-$ and $y-$axes)

As a representative example, the Lamb wave signal captured via pulse-echo path $A_6 - S_6$, after being normalised by the magnitude of the incident wave, is displayed in Fig. 3.7(a). For comparison, the corresponding baseline signal is included in the same diagram, where the damage-reflected A_0 mode stands out clearly. As a result of small angle of wave incidence offered by pulse-echo pair $A_6 - S_6$ ($\theta < 5^0$, as defined in Fig. 2.3) the damage-reflected A_0 wave can be seen to be strong in magnitude, coinciding with observations in Figs. 2.6 and 2.11. The signal was subsequently applied with HT-based signal processing, Fig. 3.7(b), from which ToF and intensity of damage-reflected signal energy were extracted. The probability image for this pulse-echo pair was accordingly established in terms of Eq. 3.4, shown in Fig. 3.8.

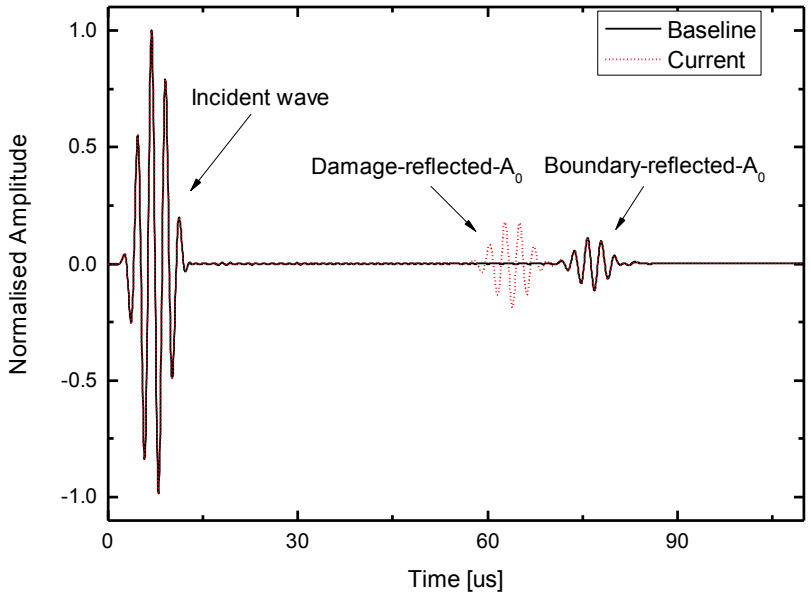

(a)

Fig. 3.7. (a) Lamb wave signals acquired via pulse-echo path $A_6 - S_6$ from FE simulation; and (b) envelopes of energy distribution of signals shown in (a) obtained using HT-based signal processing (normalised by the magnitude of incident waves)

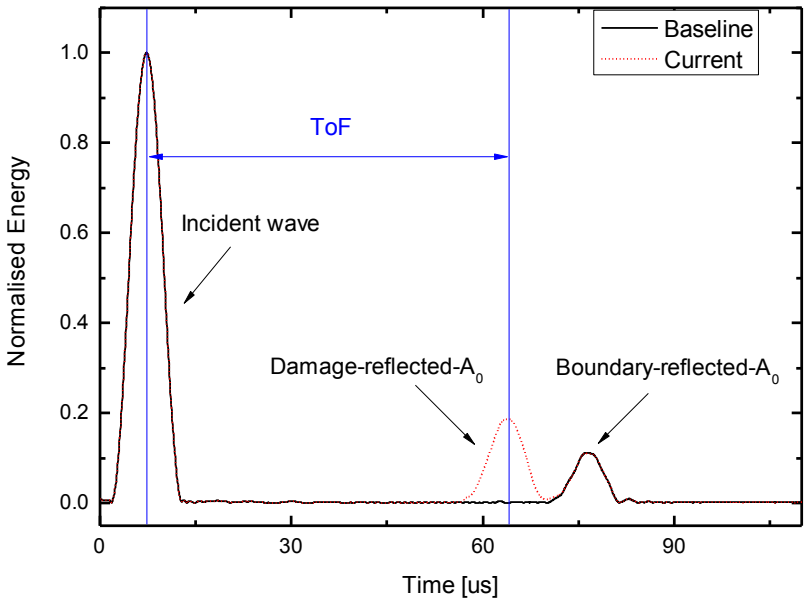

(b)

Fig. 3.7. *Cont.*

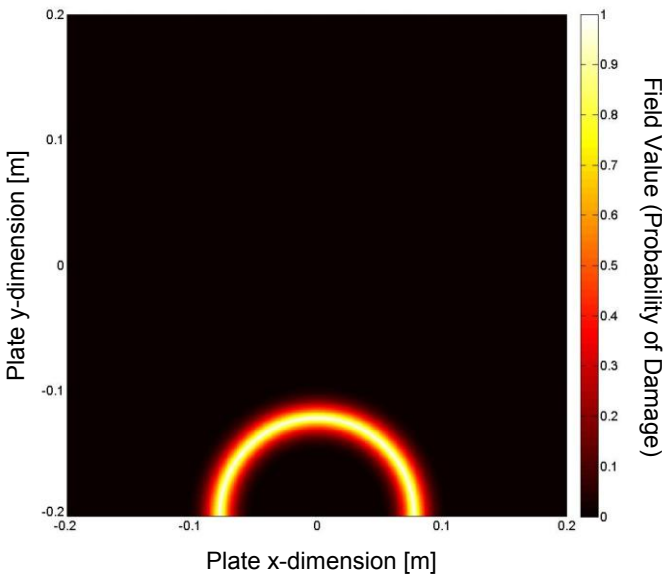

Fig. 3.8. Probability image established by pulse-echo path $A_6 - S_6$ (diagram showing inspection area only covered by the sensor network)

Source images contributed by eight pulse-echo pairs of the sensor network using the above process were fused with the two-level synthetic image fusion scheme. The interim images obtained using the arithmetic mean at the first level fusion, without and with compensation for wave attenuation with propagation distance, are displayed in Fig. 3.9. It can be seen that in the absence of compensation the approach fails to predict the damage accurately (Fig. 3.9(a)), because the reduction in intensity of signal energy as propagation distance was counted by the algorithm as changes in damage orientation. Note that no pronounced error in predicting damage location can be noticed even without compensation because prediction of damage location by the algorithm is fully based on ToFs in terms of Eq. 3.3, independent of signal intensity. In the contrast, both location and shape of the damage can be estimated accurately when compensation was applied, Fig. 3.9(b). By complying with this conclusion, compensation for wave attenuation with propagation distance was always taken into account in following study.

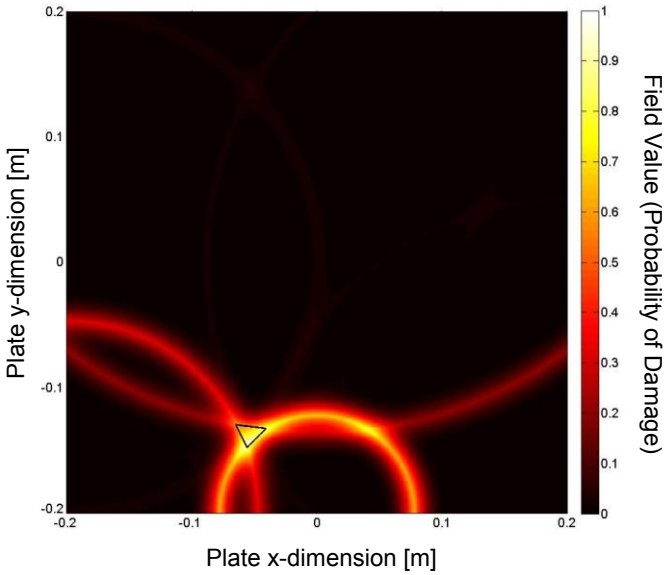

(a)

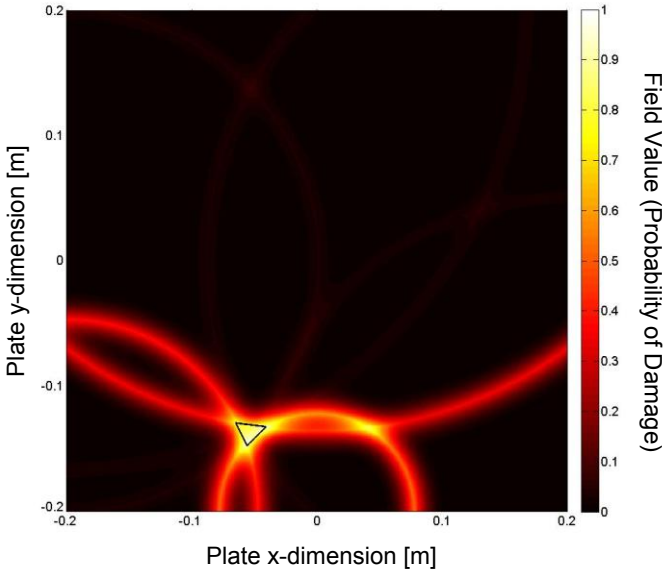

(b)

Fig. 3.9. Interim probability images obtained using arithmetic mean at the first level fusion: (a) without and (b) with compensation for wave attenuation as propagation distance

Further applying the second level fusion on interim images, the ultimate resultant probability image is exhibited in Fig. 3.10, where orientation of three edges of the triangular damage are clearly revealed, further portraying the shape of the damage.

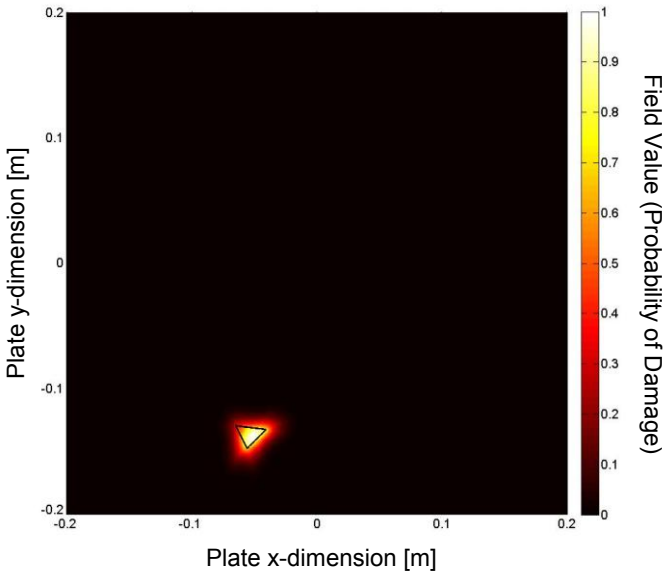

Fig. 3.10. Ultimate resultant probability image obtained using the two-level synthetic fusion scheme

3.5 Applications to Damage Identification

3.5.1 Specimen Configuration

An aluminium sample of the same dimension as the one used in the above simulation was prepared. A through-thickness crack of 16 mm in length and 0.64 mm in

width (Scenario I) was introduced to the plate using a fine blade. The crack was then extended to an L-shape crack consisting of two through-thickness cracks (Edge I and Edge II), 25 mm long and 1.5 mm wide each (Scenario II). Two damage scenarios are shown schematically in Figs. 3.11 and 3.12, respectively. An active sensor network consisting of 16 circular PZT wafers (nominal diameter: 5 mm, thickness: 0.5 mm each) with material properties detailed in Table 2.1 was surface-mounted to the plate to configure eight pulse-echo pairs, referring to Fig. 3.11(b) for locations of individual PZT wafers. The signal generation and acquisition system introduced in Section 2.3.2 was employed to produce a diagnostic signal the same as the one used in the simulation which were then applied in turn on each PZT actuator to generate incident wave after being amplified to 60 $V_{p\text{-}p}$. The crack-reflected wave signals were acquired via each sensor using an oscilloscope (HP™-54810A) at a sampling rate of 25 MHz.

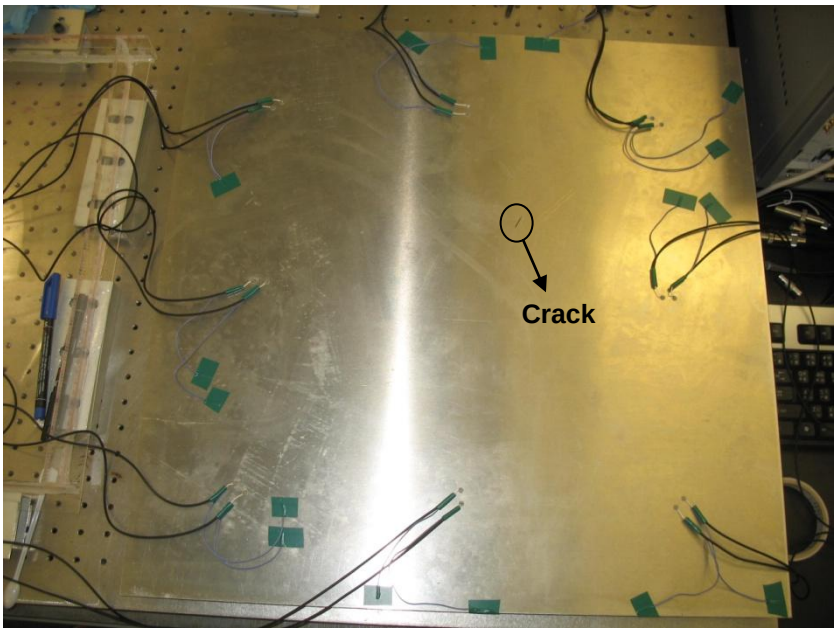

(a)

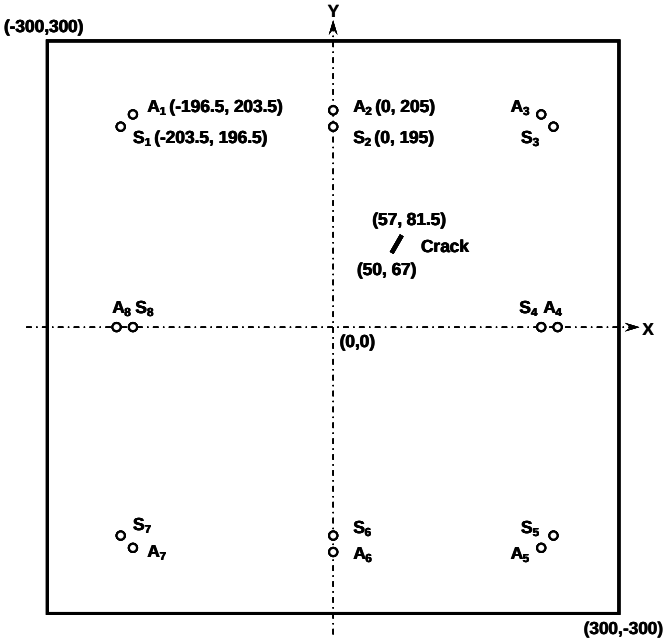

(b)

Fig. 3.11. (a) Aluminium specimen and (b) its configurations for identifying a through-thickness crack (scenario I) (unit: mm) (allocation of PZT elements in the sensor network being symmetric relative to $x-$ and $y-$axes)

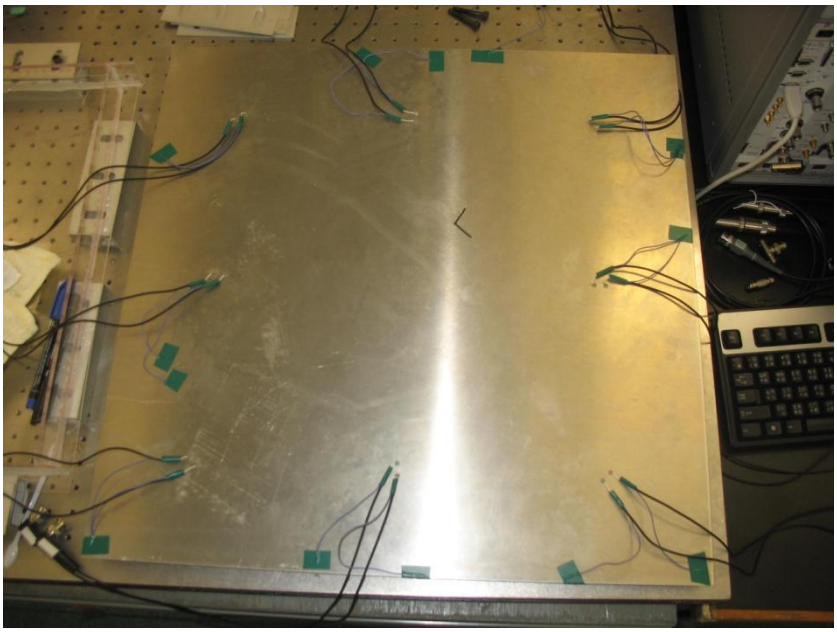

(a)

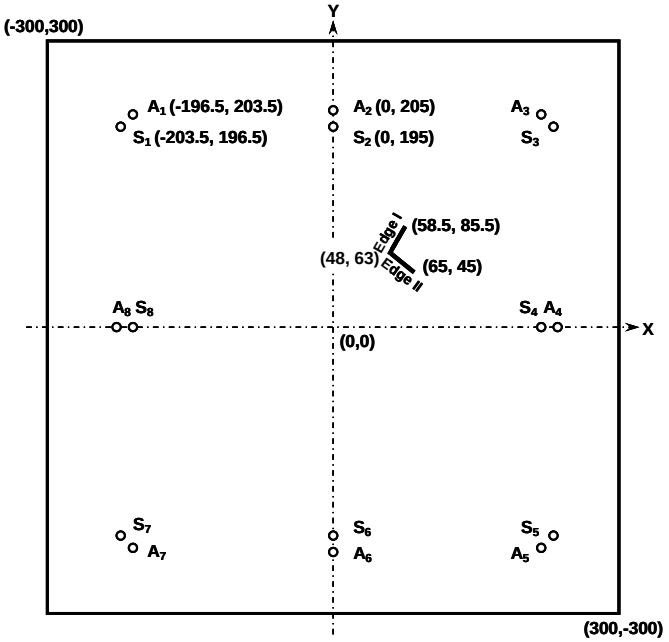

(b)

Fig. 3.12. (a) Aluminium specimen and (b) its configurations for identifying an L-shape crack (scenario II) (unit: mm) (allocation of PZT elements in the sensor network being symmetric relative to $x-$ and $y-$axes)

3.5.2 Signal Processing

Captured raw Lamb wave signals unavoidably contained various noise and it was of necessity to filter out such unwanted signal features. Thus, only wave component of interest was retained and applied for further analysis.

In this study, captured raw wave signals were pre-processed using signal averaging to reduce global noise and minimise uncertain fluctuation, and then applied with continuous wavelet transform (CWT) as introduced in Section 1.2.3. Upon CWT, wave component corresponding to the excitation frequency (450 kHz in this study) was extracted.

In CWT, a number of wavelets are available. A basic selection criterion is that the waveform of a selected wavelet should be as similar as possible to the waveform of the captured wave signal, since the wavelet coefficient actually indicates the similarity between the wavelet function and the signal to be processed. In this study, the Morlet wavelet (as shown in Fig. 3.13) was employed as the mother wavelet due to its closest similarity to the designed diagnostic signal.

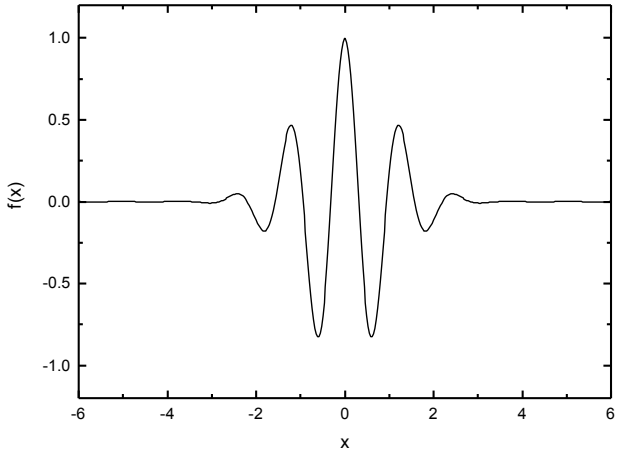

Fig. 3.13. Morlet wavelet function

A typical captured raw Lamb wave signal and its CWT-processed result are displayed in Figs. 3.14(a) and (b), respectively. It can be observed that, upon application of CWT, higher frequency noise included in the raw signal is reduced significantly.

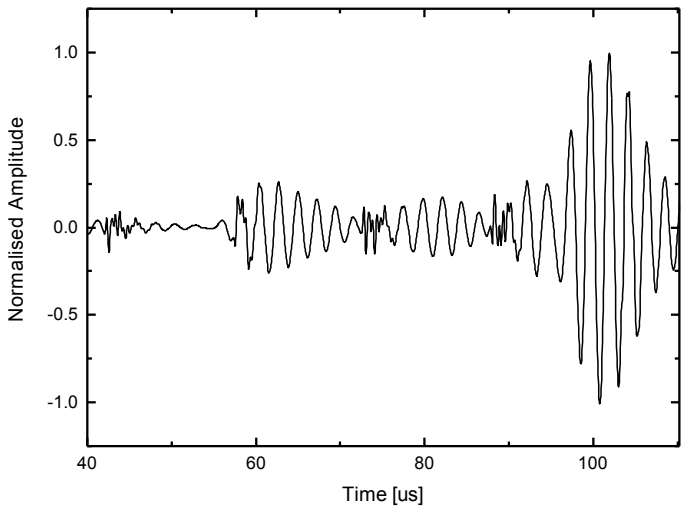

(a)

Fig. 3.14. (a) A typical raw Lamb wave signal from experiment; and (b) its CWT-processed result

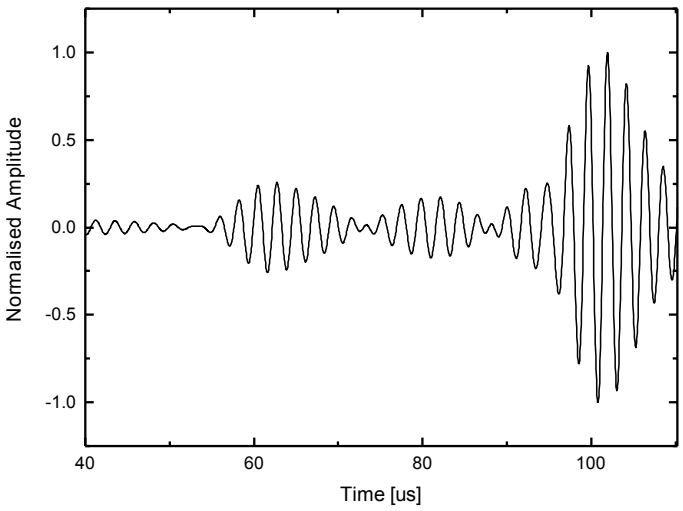

(b)

Fig. 3.14. *Cont.*

3.5.3 Results and Discussions

In experiment it is important to select the most appropriate frequency at which the activated waves are able to deliver maximum coupling between the host structure and PZT wafers, leading to a high signal-to-noise ratio (SNR). To determine such a frequency, a sweep frequency test ranging from 200 to 700 kHz was conducted. The Lamb wave signal acquired via sensing path $A_5 - S_4$ at frequencies of 250, 350, 450 and 550 kHz, as examples, are compared in Fig. 3.15, to observe that the wave signal at a central frequency of 450 kHz presents the maximum response in signal magnitude. Moreover, at this frequency, the S_0 mode is substantially suppressed (magnitude of S_0 mode is below one-fifth that of the A_0 mode). Accordingly, 450 kHz was selected

as the excitation frequency in all following experiments.

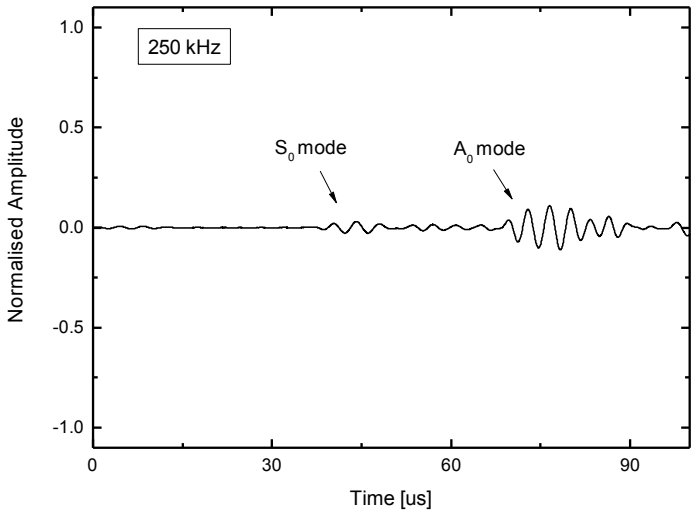

(a)

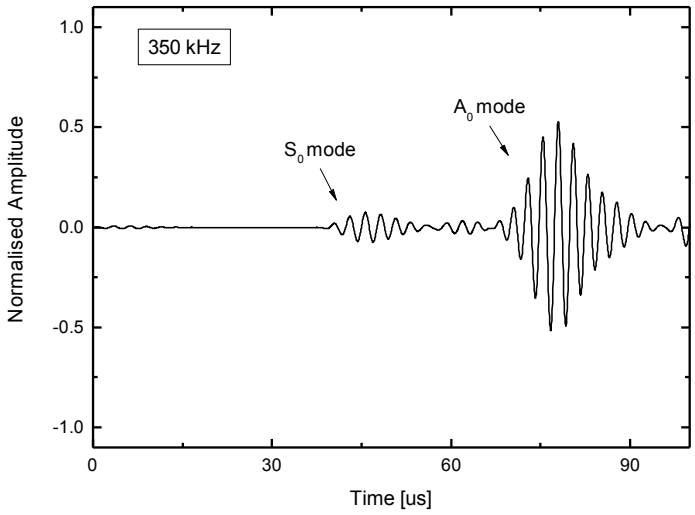

(b)

Fig. 3.15. Lamb wave signals acquired via sensing path $A_5 - S_4$ at excitation frequencies of (a) 250 kHz; (b) 350 kHz; (c) 450 kHz; and (d) 550 kHz (normalised by the signal intensity at 450 kHz)

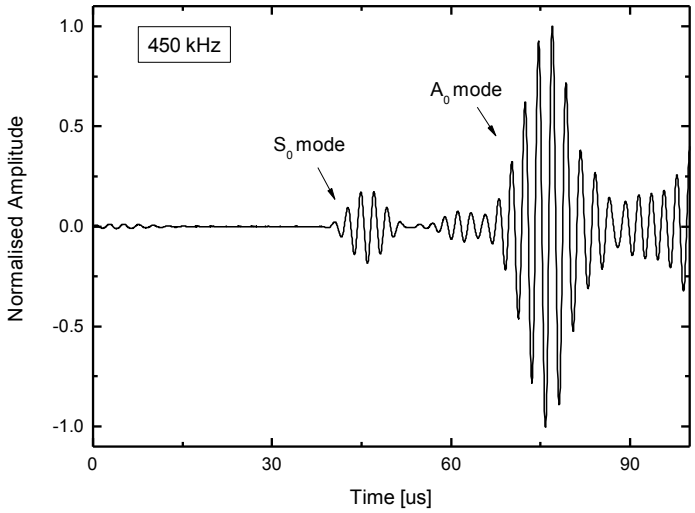

(c)

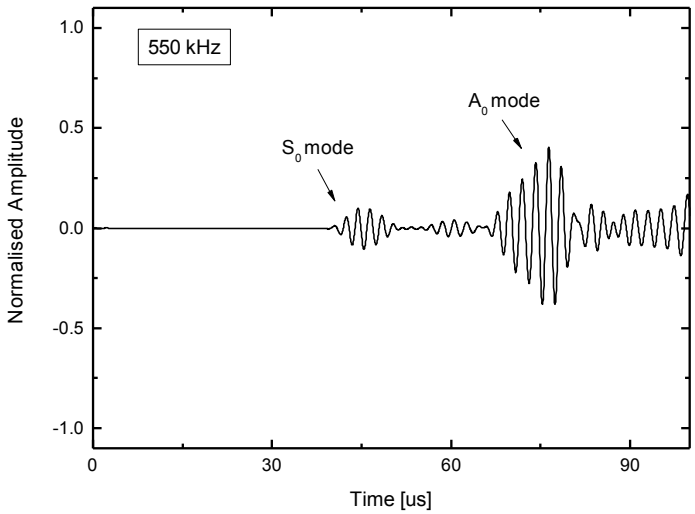

(d)

Fig. 3.15. *Cont.*

Representatively, Lamb wave signals acquired via pulse-echo path $A_1 - S_1$ are displayed in Fig. 3.16(a) for two created damage scenarios (scenarios I and II: crack and L-shape crack, respectively), upon application of CWT-based signal processing.

All captured signals were normalised relative to the magnitudes of their corresponding incident waves. The normalisation processing was aimed to eliminate discrepancies incurred due to the soldering and bonding among different pulse-echo paths. In order to obtain the field values concerning signal intensity, captured wave signals were subsequently processed with HT to highlight energy concentrations, shown in Fig. 3.16(b). To further strengthen damage-scattered wave packet, the difference between the HT-processed current signals and corresponding baseline signal for this pulse-echo path are shown in Fig. 3.16(c).

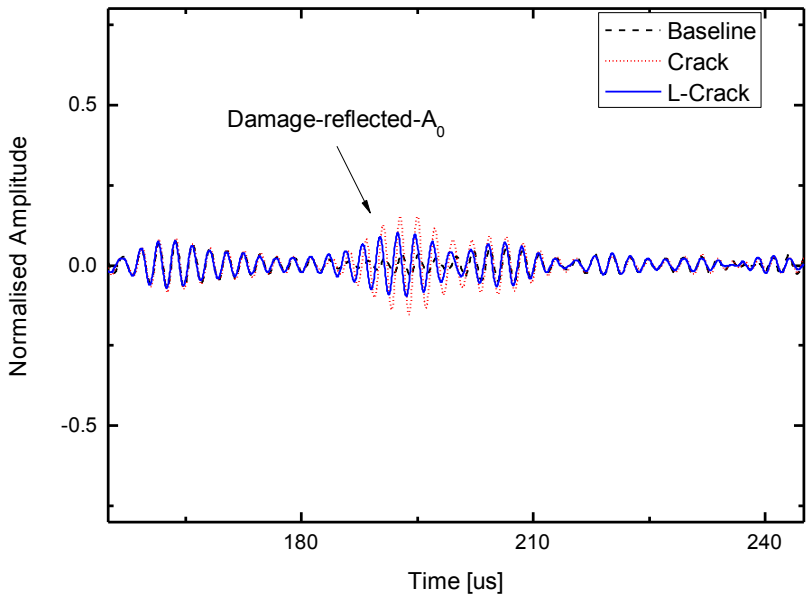

(a)

Fig. 3.16. (a) Lamb wave signals acquired via pulse-echo path $A_1 - S_1$ from experiment (normalised by the magnitude of incident waves); (b) corresponding envelopes of energy distribution of signals in (a) obtained using HT-based signal processing; and (c) residual signals upon subtraction baseline signal from current signals

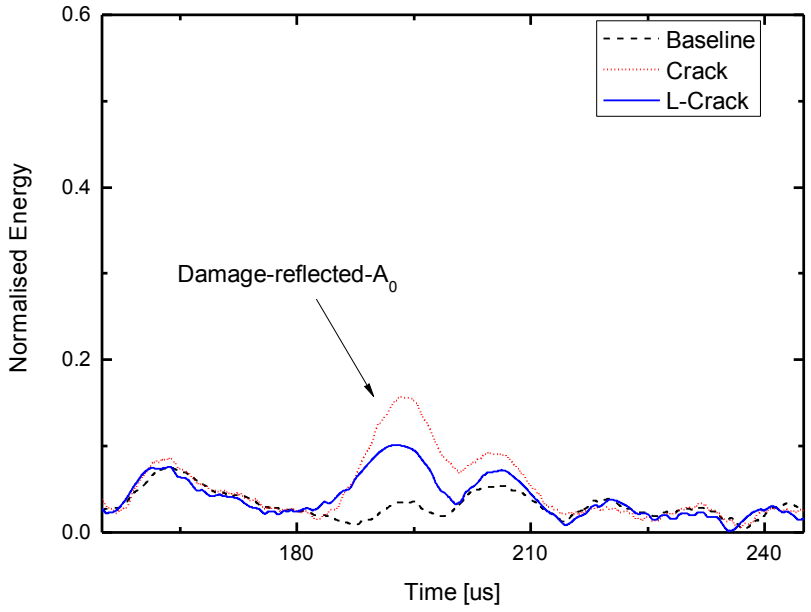

(b)

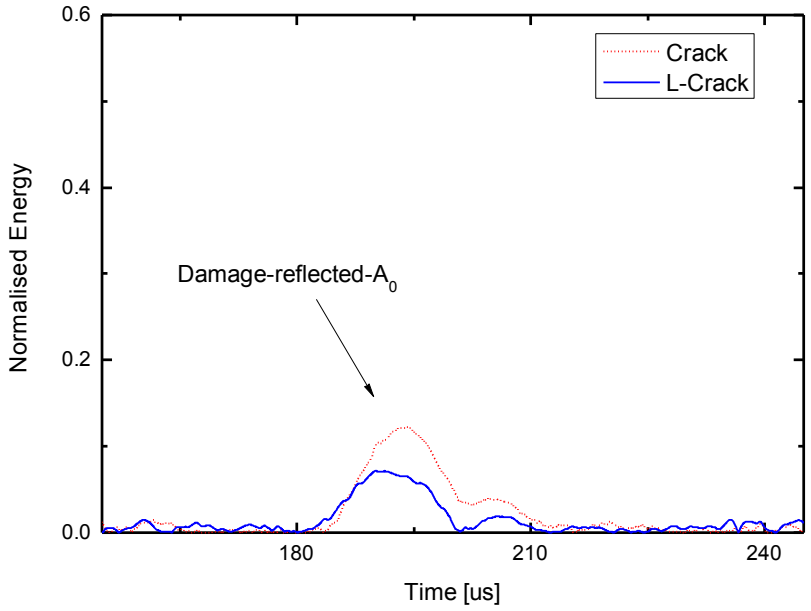

(c)

Fig. 3.16. *Cont.*

Similar as above, Lamb wave signals acquired via pulse-echo path $A_3 - S_3$, their HT-processed counterparts, and difference between HT-processed current signals and corresponding baseline signal are exhibited in Fig. 3.17.

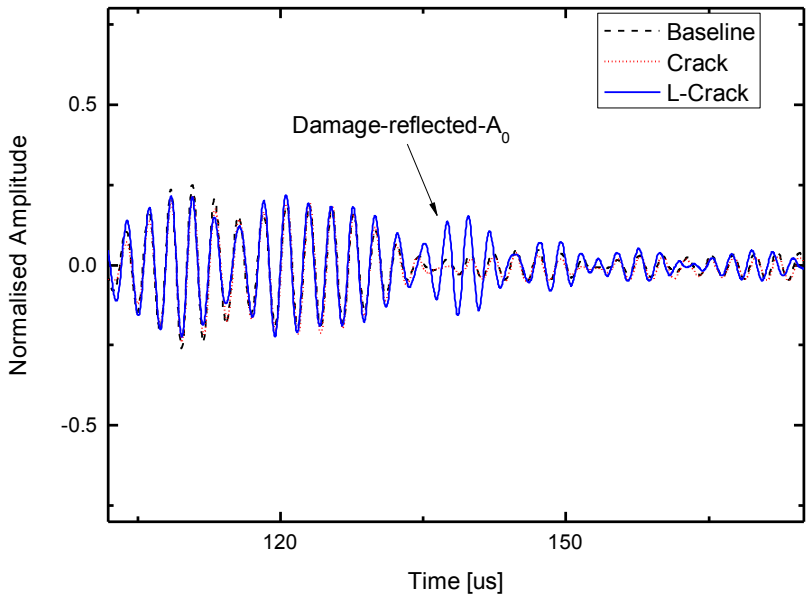

(a)

Fig. 3.17. (a) Lamb wave signals acquired via pulse-echo path $A_3 - S_3$ from experiment (normalised by the magnitude of incident waves); (b) corresponding envelopes of energy distribution of signals in (a) obtained using HT-based signal processing; and (c) residual signals upon subtraction baseline signal from current signals

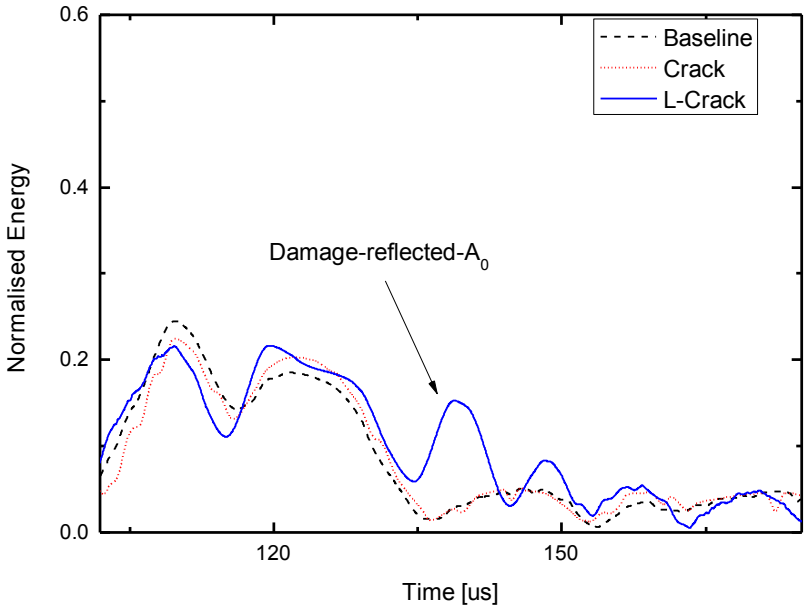

(b)

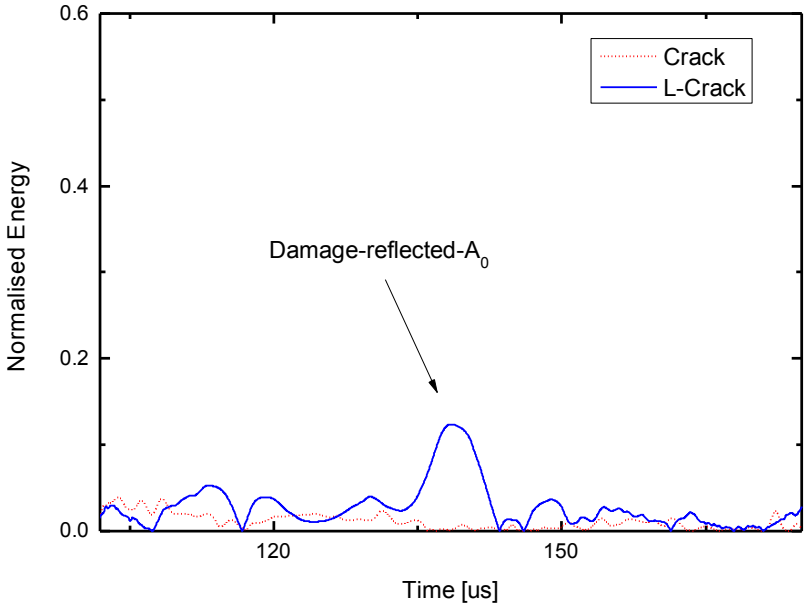

(c)

Fig. 3.17. *Cont.*

In Fig. 3.16(c) for $A_1 - S_1$, the A_0 modes scattered by the crack (Scenario I) and the L-shape crack (Scenario II) hold high intensity, because of the relatively small angle of wave incidence ($\theta < 5^0$) with regard to the orientation of crack (Scenario I) and orientation of Edge I (Scenario II). In Fig. 3.17(c) for $A_3 - S_3$, strong reflection remains for Scenario II but not for Scenario I, because the angle of wave incidence via this sensing path is large ($\theta > 70^0$) with regard to the orientation of crack (Scenario I), leading to weak scattering in terms of Figs. 2.6 and 2.11. For Scenario II, incident wave via $A_3 - S_3$ becomes insensitive to Edge I but is well scattered by Edge II ($\theta < 5^0$), therefore keeping high intensity.

Applying the developed imaging approach supplemented with the two-level synthetic fusion scheme, two interim and ultimate resultant images for Scenario I are shown in Fig. 3.18, to observe accurate identification results in the ultimate resultant image (Fig. 3.18(c)), in which the predicted damage location, orientation and length match well the real ones.

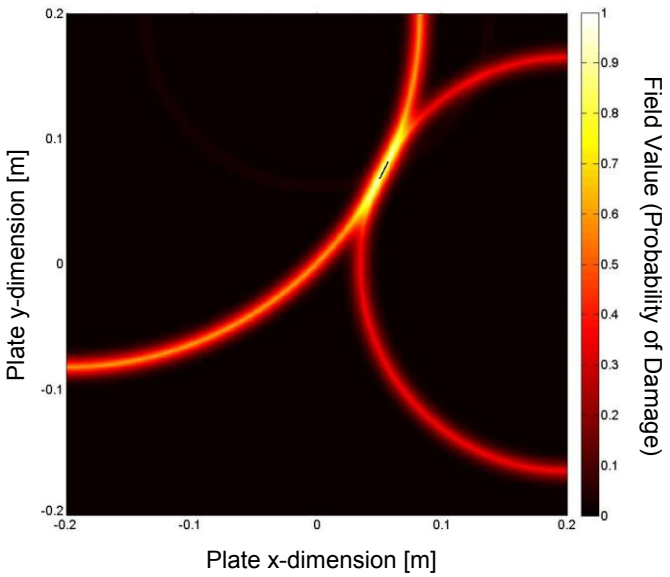

(a)

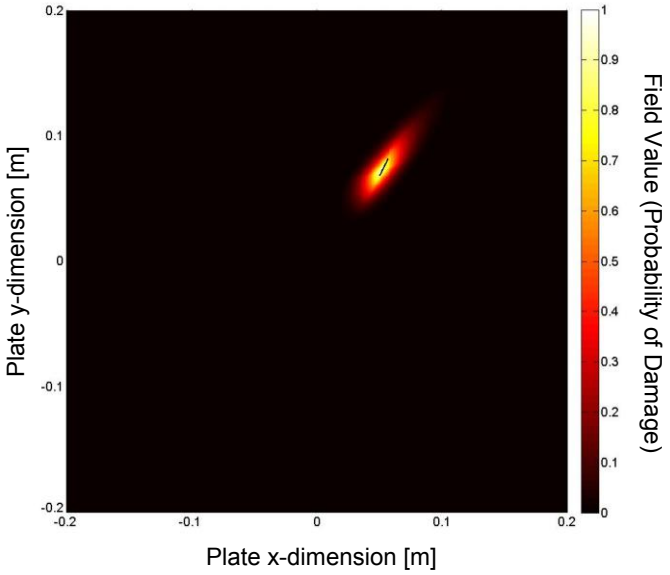

(b)

Fig. 3.18. Probability images for damage Scenario I using (a) arithmetic mean (interim image) and (b) geometric mean (interim image) at the first level; and (c) conjunctive fusion (ultimate image) at the second level (short solid line: real crack)

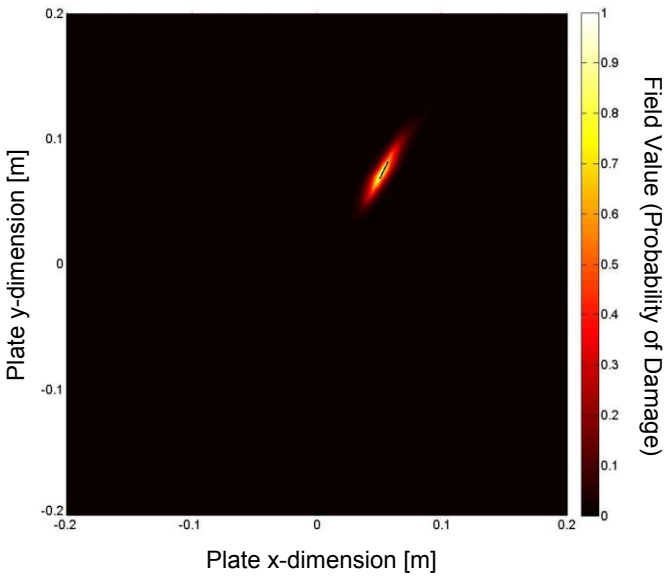

(c)

Fig. 3.18. *Cont.*

It is noteworthy that in this approach both the waves reflected from the main body of crack and the waves scattered from crack tips were taken into account, thanks to the active sensor network which enabled the diagnostic waves to be emitted from different incidence angles, as explained in Fig. 3.19 for Scenario I, where the waves reflected by the main body of crack were captured by sensing path $A_1 - S_1$ while waves scattered by individual crack tips by $A_2 - S_2$ and $A_8 - S_8$, respectively. Features extracted from signals captured via different paths were then fused using the two-level synthetic image fusion. This makes it possible to deliver a quantitative description of the damage including the orientation and size.

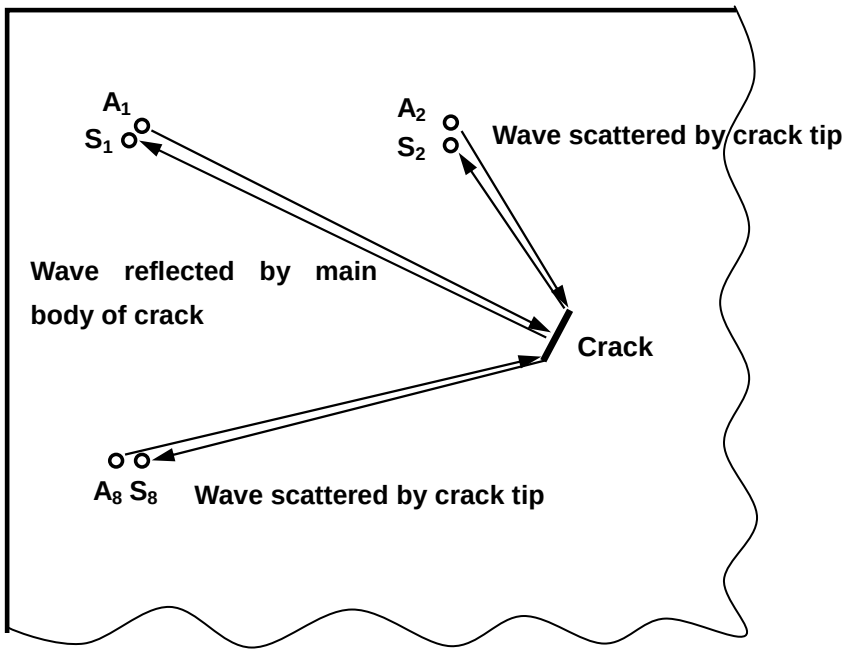

Fig. 3.19. Illustration for signal feature extraction via different sensing paths in a sensor network (different sensing paths providing various signal features associated with damage for two-level synthetic image fusion)

For Scenario II, the interim and ultimate resultant images are shown in Fig. 3.20. Relatively large prediction errors are observed, which are attributable to the fact that Edge I and Edge II are almost perpendicular to each other, and if a particular sensing path perceives strong reflection from one of the two edges then the same sensing path would be insensitive to the other; when all images are fused, the common part perceived by this sensing path (connection area of Edge I and Edge II) is double enhanced in the ultimate resultant image, but two tips of the L-shape crack are de-emphasised. For this reason, two edges of the L-shape crack are not clearly highlighted simultaneously in the resultant image. Such a deficiency in detecting

L-shape crack is to be circumvented in the following chapter.

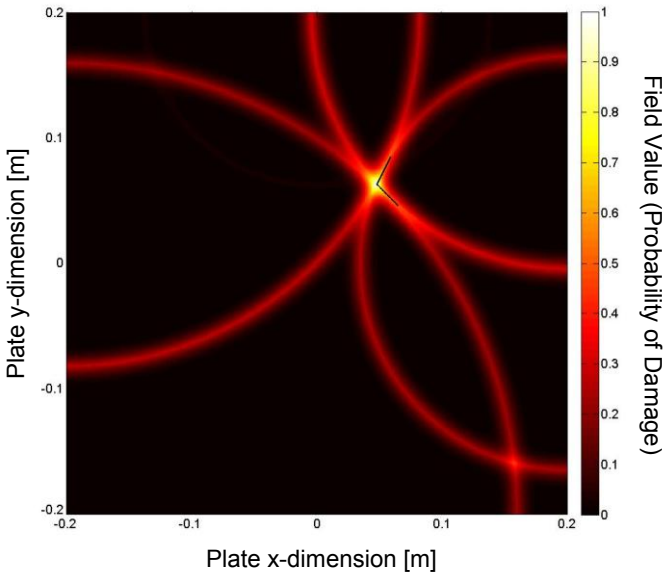

(a)

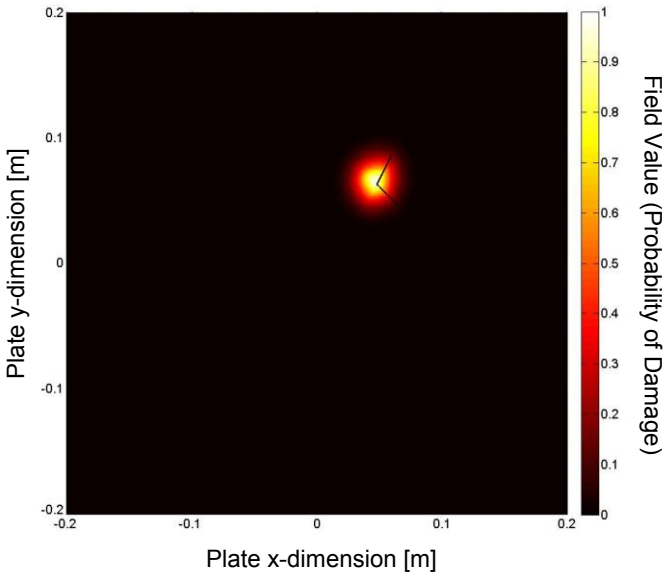

(b)

Fig. 3.20. Probability images for damage Scenario II using (a) arithmetic mean (interim image) and (b) geometric mean (interim image) at the first level; and (c) conjunctive fusion (ultimate image) at the second level (short solid line: real edge of the L-shape crack)

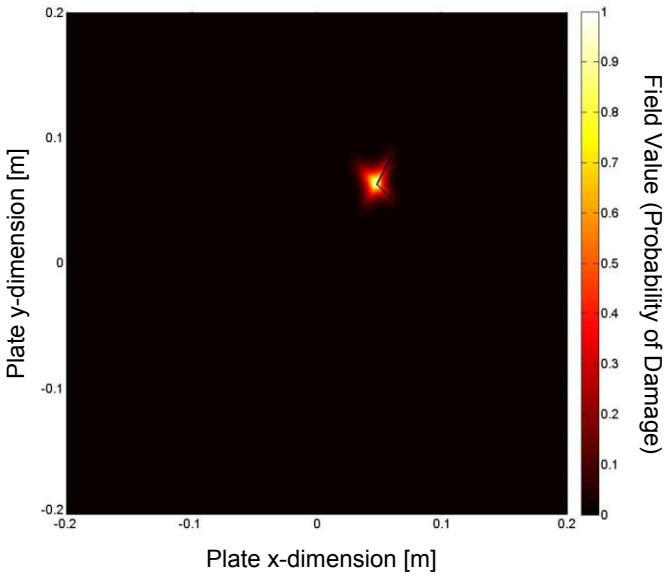

(c)

Fig. 3.20. *Cont.*

3.6 Concluding Remarks

In this chapter, based on the established correlations between damage parameters (location, orientation and shape) and extracted signal features, a PDI approach was developed in conjunction with use of an active sensor network in conformity to a pulse-echo configuration. Damage location, orientation of individual edges of damage can be estimated, facilitating quantitative description of damage shape. To enhance robustness and tolerance to measurement noise/uncertainties and possible erroneous perceptions from particular sensing paths, a two-level synthetic image fusion scheme was developed. The effectiveness of this approach was demonstrated by predicting

orientation-specific damage including a triangular through-thickness hole (through FE simulation) and a through-thickness crack (through experiment) in aluminium plates. The results, highlighted in intuitional and easily interpretable images, have shown satisfactory accuracy of the developed approach for identifying orientation-specific damage.

CHAPTER 4 Probability-based Diagnostic Imaging Using Hybrid Pulse-echo and Pitch-catch Configurations

4.1 Introduction

The probability-based diagnostic imaging (PDI) established in Chapter 3 relies on sole pulse-echo configuration. To overcome deficiencies of this method (not capable of depicting damage of multi-edges with arbitrary orientations), an enhanced PDI approach taking advantage of hybrid pulse-echo and pitch-catch configurations was developed in this chapter. Various signal characteristics were extracted via this hybrid sensor network, to establish relationships between (i) temporal information and damage location, (ii) intensity of signal energy and damage orientation/shape, and (iii) signal correlation and damage location/size. A novel concept of '*virtual sensing*' was proposed to facilitate acquisition of these signal features. The approach was validated by predicting representative damage scenarios including L-shape through-thickness crack (orientation-specific damage), polygonal damage (multi-edge damage) and multi-damage in aluminium plates.

4.2 Principle of Diagnostic Imaging Using Pitch-catch Configuration

Selecting and establishing an appropriate field value is the core step in a PDI approach. In Chapter 3, key signal features including ToF and intensity of signal energy were employed to develop field values. The developed field value was able to depict damage parameters including location and shape. However, when dealing with some orientation-specific damage such as L-shape, measurement noise may overwhelm damage-related information, impairing detection accuracy and prevision. To circumvent such deficiency, additional signal feature, correlation coefficient, was further extracted and applied to develop enhanced field value.

4.2.1 Signal Correlation-based Field Value

It is appreciated that the correlation coefficient between the signals captured from the monitored structure (current signal) and from its 'healthy' counterpart (baseline signal) can quantitatively indicate changes in the structure along or near the sensing paths via which the signals are acquired. The physical intuition behind this is that a captured wave signal would change drastically if a defect right locates on or very close to its sensing path, presenting a relatively small correlation coefficient. In contrast, the signal deviation would be trivial if the defect is away from the sensing path, leading to

high similarity between the current and baseline signals (*i.e.*, a great correlation coefficient). The correlation coefficient has in particular proven susceptibility to changes in signal phase (leading to different ToFs) as well as changes in local signal amplitude (leading to different intensities of signal energy) [89], advantageous over other signal features in terms of the sensitivity to phase delay and reduction in signal amplitude. For this reason, signal features associated with signal correlation were further extracted to develop the field value, as a supplement to the field value defined by Eq. 3.4 based on ToF and intensity of signal energy.

Considering two wave signals of the same length $X=\{x_1, x_2, ..., x_n\}$ (current signal) and $Y=\{y_1, y_2, ..., y_n\}$ (baseline signal) (both having n sampling points) captured via a sensing path having an included angle of α relative to a pre-selected baseline direction, a field value can be defined as (all the pixels along a sensing path holding the same field value),

$$I(\alpha)=1-|\rho_{XY}|, \tag{4.1}$$

where ρ_{XY} is the correlation coefficient between X and Y, defined as

$$\rho_{XY}=\frac{C_{XY}}{\sigma_X \cdot \sigma_Y}=\frac{\sum_{i=1}^{n}(x_i-\eta_X)(y_i-\eta_Y)}{\sqrt{\sum_{i=1}^{n}(x_i-\eta_X)^2}\cdot\sqrt{\sum_{i=1}^{n}(y_i-\eta_Y)^2}}. \tag{4.2}$$

In the above, C_{XY} is the covariance of X and Y; σ and η are the standard

deviation and mean of the signal, respectively, distinguished by different subscripts for two signals. Because X and Y are two signals captured via the same sensing path in the same structure (at two different moments), the greater the similarity between them, the closer to unity is the coefficient, leading to low field values at pixels along this sensing path and indicating low probability of damage existence near this sensing path; in contrast, in the case damage occurs in or close to the sensing path, correlation coefficient between two signals becomes particularly low, resulting in high field values at pixels along this sensing path.

4.2.2 Retrofitted Field Value Using Concept of Virtual Sensing

However, due to the small influential area of a sensing path demonstrated in Section 2.5, the image established by such a path often shows a very narrow band of highlight along the sensing path, if part of the damage is in the path or very close to it; while those pixels at other regions of the image hold very low field values. In other words, a particular sensing path can only sense damage near it, making the field value defined by Eq. 4.1 highly inert to distant damage. By way of illustration, Fig. 4.1 presents a probability image established by a sensing path right passing through damage, to observe that only those pixels along this sensing path have very high field values.

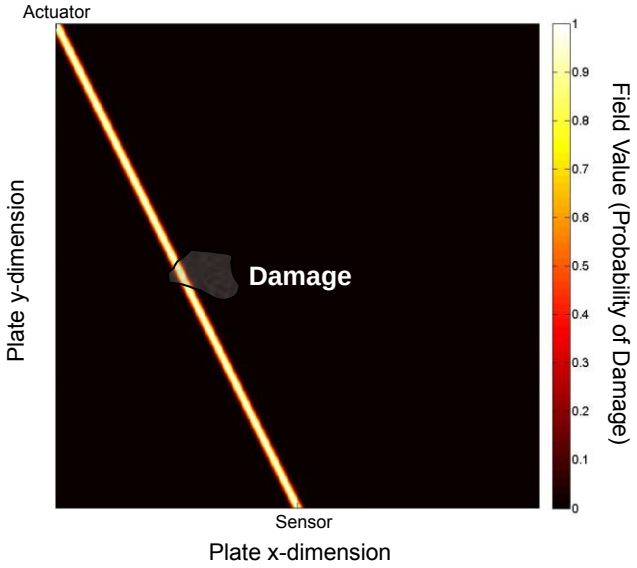

Fig. 4.1. A typical probability image established by a sensing path using the means for defining field value in terms of Eq. 4.1

The above-addressed property (a sensing path can only sense damage near it) can be beneficial to the identification of multi-damage (to be detailed in Section 4.4.3), but it poses harsh requirement on the density of sensing paths to cover the whole inspection area. Although more sensing paths certainly help to achieve a denser coverage and to detect damage of more random locations, merits of the developed PDI approach over traditional tomography capitalising on a large number of actuator-sensor pairs are compromised considerably.

To tackle this deficiency, an interpolation method based on a novel concept of '*virtual sensing*' was developed in this study to enhance the efficiency, with a hope of producing more sensing paths using limited sensors. Consider a sensor network

comprised of an actuator, A, and five sensors, S_1, S_2, S_3, S_4 and S_5, forming five sensing paths: $A-S_1$, $A-S_2$, $A-S_3$, $A-S_4$ and $A-S_5$, shown schematically in Fig. 4.2. Knowing that the angle of each sensing path relative to a baseline direction (*e.g.*, $A-S_5$) respectively being α_1, α_2, α_3, α_4 and α_5 ($\alpha_5 = 0^0$ for the current selection of baseline direction), field values at pixels along these five sensing paths can be calculated using Eq. 4.1 which are $I(\alpha_1)$, $I(\alpha_2)$, $I(\alpha_3)$, $I(\alpha_4)$ and $I(\alpha_5)$, respectively. Apart from those sensing paths configured by physically existing actuator (A) and sensors (S_1, S_2, S_3, S_4 and S_5), virtual sensing paths connecting A and imaginary sensors ($S_{virtual}$) located at any position of interest within the inspection area are formed virtually. For the discussed case in Fig. 4.2, field value at all pixels along a virtual sensing path, $A-S_{virtual}$ (connecting A and an imaginary sensor $S_{virtual}$, with an angle of $\alpha_{virtual}$ with regard to the baseline direction), can be obtained using the field values of two physical sensing paths which are clockwise and anticlockwise closest to $A-S_{virtual}$, by linearly scaling their respective field values and angles, as

$$I(\alpha_{virtual}) = I(\alpha_k) + (\alpha_{virtual} - \alpha_k)\frac{I(\alpha_{k+1}) - I(\alpha_k)}{\alpha_{k+1} - \alpha_k}, \qquad (\alpha_{k+1} < \alpha < \alpha_k)$$

(4.3)

where $I(\alpha_{virtual})$ is the field value of the discussed virtual sensing path $A-S_{virtual}$ established using Eq. 4.1. Same as a physical sensing path, all pixels along a virtual sensing path hold the same field value.

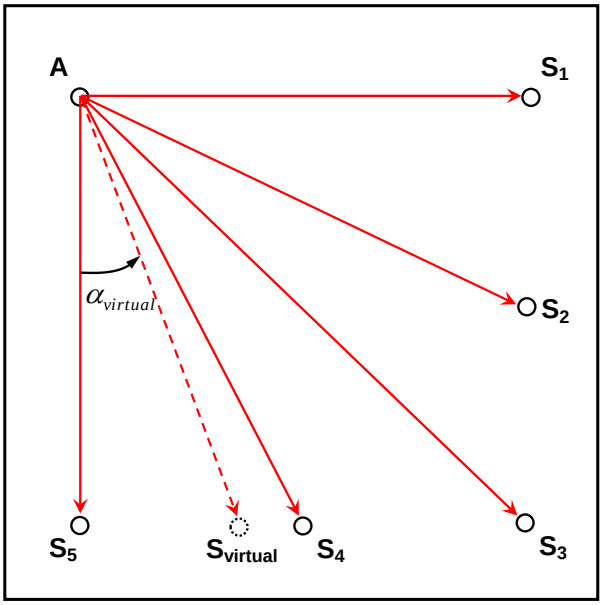

Fig. 4.2. Schematic of a sensor network consisting of five physical sensing paths and a virtual sensing path

In virtue of the concept of '*virtual sensing*', the field values at all pixels across the entire inspection region, even for those areas in which there is no any physical sensing path passing through, can be estimated by changing $\alpha_{virtual}$ with a tiny increment (*e.g.*, 1^0) relative to the baseline direction. The concept of '*virtual sensing*' virtually expands the sensor network coverage by enriching sensing information without actually adding more sensors.

4.3 Hybrid Imaging Fusion

Hybrid pulse-echo and pitch-catch configurations were employed to develop field values of probability image. To make a clear distinction, field value defined by Eq. 3.4 which was used for pulse-echo configuration is classified as the first genre of field value, while field value defined by Eqs. 4.1 and 4.3 which were used for pitch-catch configuration is classified as the second genre of field value. In terms of Eqs. 3.4, 4.1 and 4.3, various signal features were extracted to develop different genres of field value, resulting in different kinds of probability images (*e.g.* Figs. 3.4 and 4.1). The image established by a sensing path, whichever genre was used, is defined as the *source image* hereinafter. A source image is the prior perceptions regarding damage from the viewpoint of the sensing path that creates it.

In practice, a source image contains not only information associated with damage but unwanted features such as ambient noise and measurement uncertainties, multiple wave modes and reflections from structural boundaries. These unwanted signal features possibly dim damage-related information, further weakening perceptions from individual source images. To circumvent this problem, an image fusion algorithm was developed.

For illustration, take a sensor network consisting of N pairs of actuator and sensor $((A_i, S_i),\ i = 1,\ 2,\ \cdots,\ N)$ as shown in Fig. 4.3. Now, there are two types of sensing

configurations are available: *pulse-echo* ($A_i - S_i$ ($i = 1,\ 2,\ \cdots,\ N$)) and *pith-catch* ($A_i - S_j$, ($i,\ \ j = 1,\ 2,\ \cdots,\ N$, but $i \neq j$)), respectively. Upon preliminary signal processing (signal averaging, DC offset and CWT) and extraction of signal features (ToF, intensity of signal energy and correlation coefficients),

(i) for every single pulse-echo pair, the first genre of field value (ToF-based with integrated intensity of signal energy) is calculated using Eq. 3.4, each pulse-echo pair creating a source image. The source image established by the i^{th} pulse-echo pair is denoted by $I_i'\Big|_I$;

(ii) for every actuator A_i , the second genre of field value (correlation coefficient-based) is first calculated using Eq. 4.1, in which physically existing paths $A_i - S_j$ ($j = 1,\ 2,\ \cdots,\ N$, but $j \neq i$) contribute $N-1$ probability images. Subsequently, with the concept of '*virtual sensing*', a series of virtual sensing paths connecting A_i with imaginary sensors are created by changing $\alpha_{virtual}$ with an increment (e.g., 1^0), each virtual path rendering a probability image as well in accordance with the principle described by Eq. 4.3. All these probability images, from $N-1$ physical paths and all virtual paths, are aggregated, to create a source image for the current actuator (A_i), denoted by $I_i\big|_{II}$. Note that, to avoid excelling the maximum probability of damage presence of ONE after aggregation of all probability images, field values along a virtual path are calculated only for those pixels in the virtual path which are not included in the very narrow band of high field values of a physical sensing path (referring to Fig. 4.1).

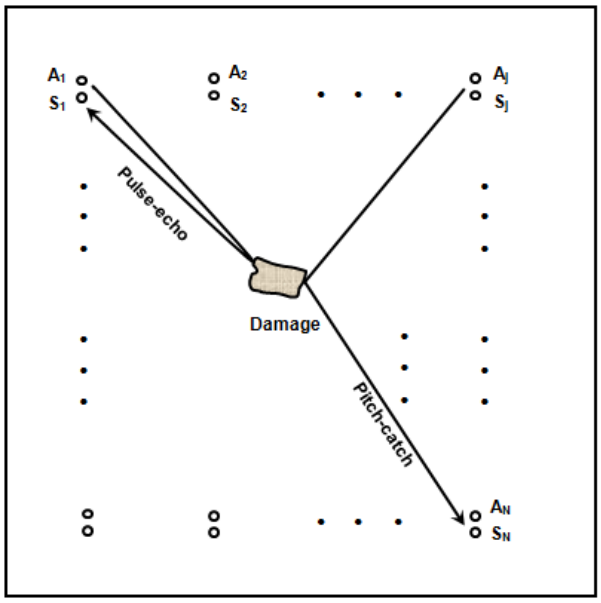

Fig. 4.3. An active sensor network consisting of N pairs of actuator and sensor

In summary, each actuator (N in total) offers a source image via pulse-echo configuration, and another source image via pitch-catch configuration. Then, a hybrid fusion scheme was developed to fuse all available source images in the sensor network, as

$$P_{hybrid} = \frac{1}{N}\sum_{i=1}^{N}(I_i'\Big|_I \cap I_i\big|_{II}), \tag{4.4}$$

as flowcharted in Fig. 4.4, where P_{hybrid} is the field value in the ultimate resulting image. The incentive to develop such a hybrid fusion scheme is driven by considerations that (i) an arithmetic fusion ('Σ' in Eq. 4.4) equally takes into account all prior perceptions from individual source images and well decentralises individual

contributions in the ultimate resulting image. Although the arithmetic fusion guarantees a full inclusion of prior perceptions from all individual source images, it is envisaged that information in all source images including ambient noise and measurement uncertainty is also engaged, which might 'pessimistically exaggerate' the possibility of damage presence, leading to false alarm (pseudo damage); and (ii) a conjunctive fusion ('$\cap$' in Eq. 4.4) multiplicatively processes source images, and a low field value at a pixel in any source image can lead to significantly low likelihood of damage presence at that pixel in the ultimate resulting image. Through the hybrid fusion, damage-related information (commonality in individual source images) is stood out and noise (random information in individual source images) is filtered.

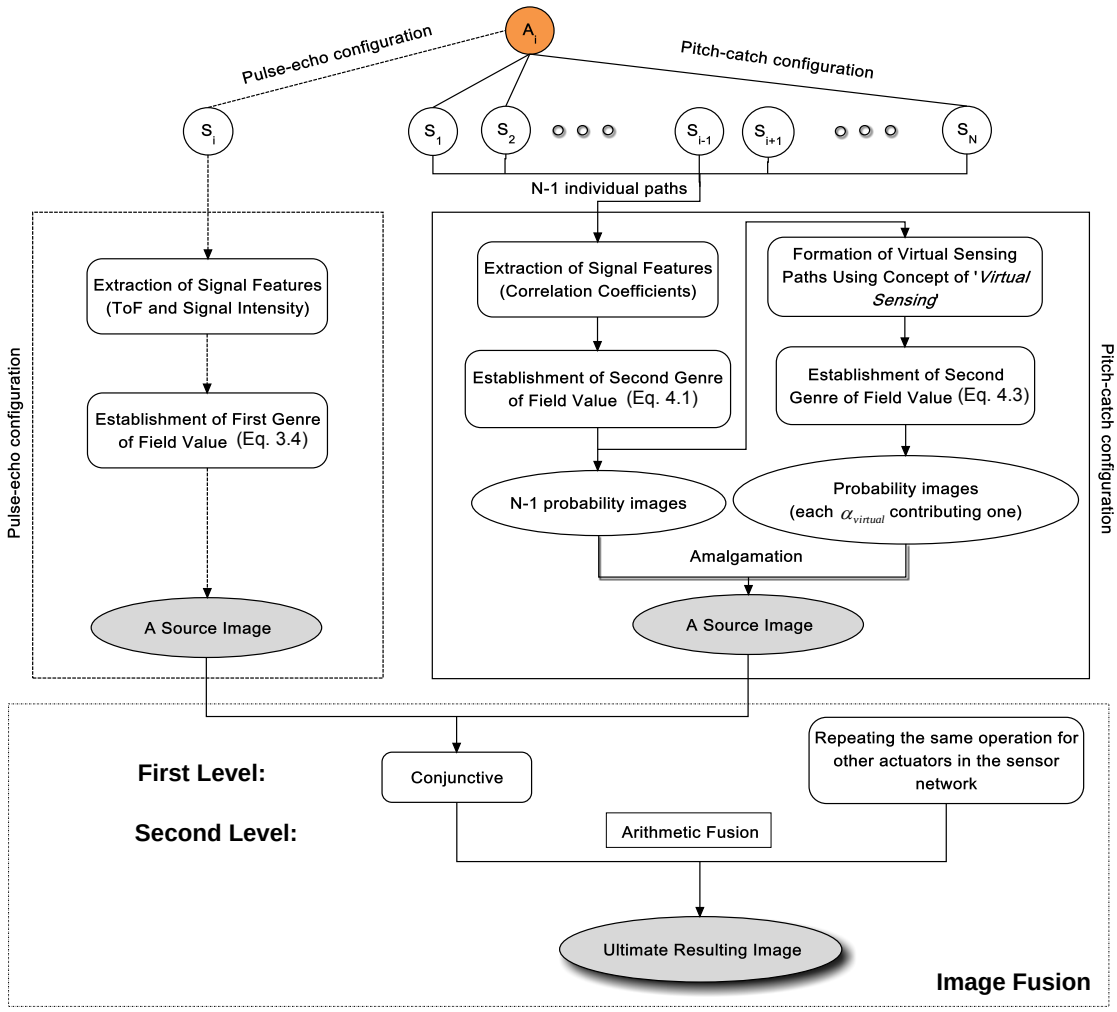

Fig. 4.4. Flowchart of hybrid fusion scheme

4.4 Applications to Damage Identification

The developed PDI approach was employed to identify various types of structural damage, including L-shape through-thickness crack (strong orientation-specific damage), polygonal damage (multi-edge damage) and multi-damage in aluminium plates.

4.4.1 L-shape Crack (Strong Orientation-specific Damage)

The aluminium specimen containing an L-shape crack used in Section 3.5.1 was used again. As shown in Fig. 3.12, 16 circular PZT wafers were surface-mounted to the plate, providing eight pulse-echo pairs, $A_i - S_i$ ($i = 1,\ 2,\ \cdots,\ 8$), and $7 \times 8 = 56$ pitch-catch sensing paths, $A_i - S_j$ ($i, j = 1,\ 2,\ \cdots,\ 8$, $i \neq j$). The aluminium specimen was instrumented with the same signal generation and acquisition system used in Section 2.3.2. All captured signals were normalised by the magnitudes of their respective incident waves, for eliminating the difference in soldering and bonding of PZT wafers.

As an example of signals captured via pulse-echo paths, Fig. 4.5(a) exemplarily displays the current and corresponding baseline signals provided by $A_3 - S_3$. In order to obtain the first genre of field value, two signals were treated with HT-based processing (Fig. 4.5(b)), whose difference is shown in Fig. 4.5(c) to strengthen extra wave packet scattered by the damage. In the difference signal, the damage-reflected A_0 mode can be observed explicitly, which features a high intensity, thanks to the relatively small angle of wave incidence along $A_3 - S_3$ with regard to Edge II ($\theta < 5^0$).

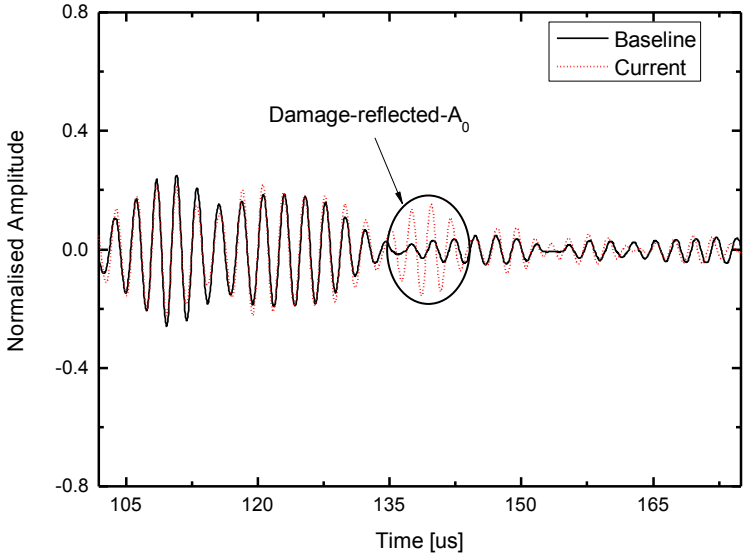

(a)

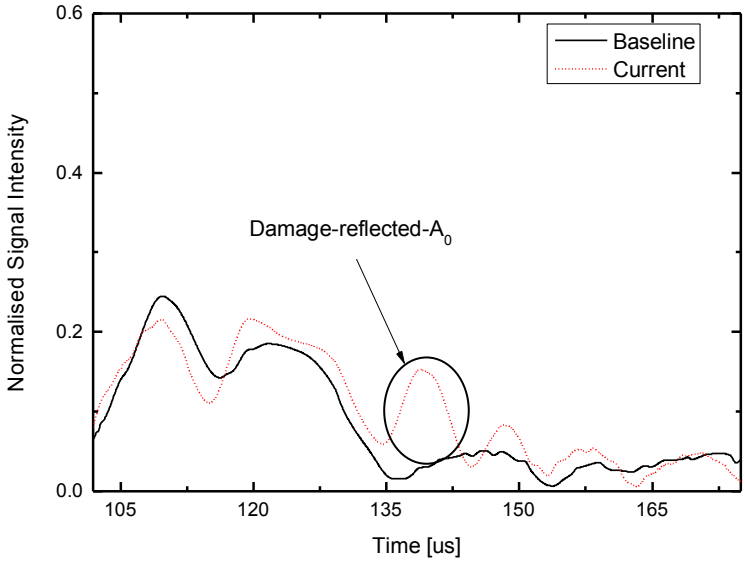

(b)

Fig. 4.5. (a) Current and baseline signals acquired via pulse-echo path $A_3 - S_3$ (normalised by the magnitude of incident waves); (b) energy distribution of signals in (a) obtained using HT; and (c) difference between two signals in (b)

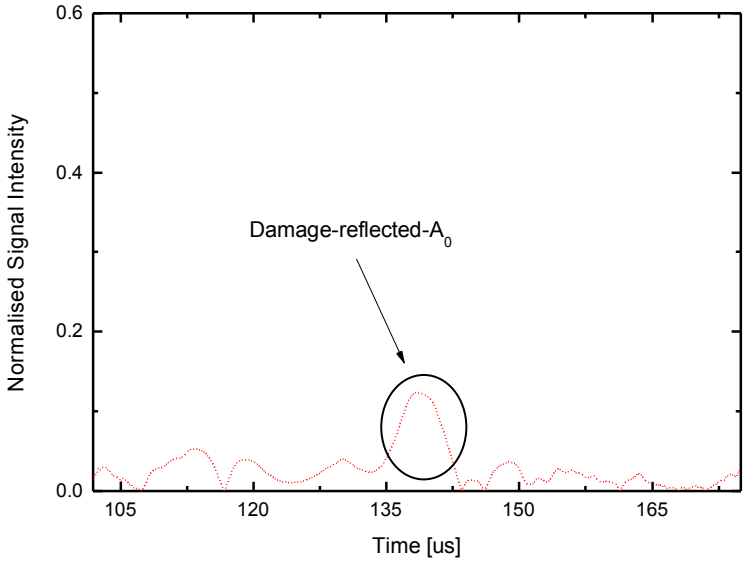

(c)

Fig. 4.5. *Cont.*

Using Eq. 3.4, the source image established by $A_3 - S_3$ was constructed, in Fig. 4.6. In accordance with the same principle, each available pulse-echo paths in the sensor network (eight in total) respectively provided a source image.

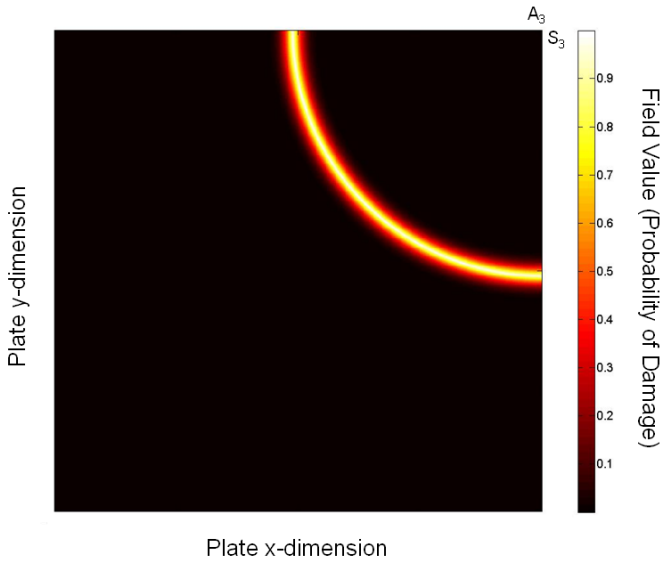

Fig. 4.6. Source image established by $A_3 - S_3$ (diagram showing inspection area only covered by the sensor network)

As an example of signals captured via pitch-catch sensing paths, Fig. 4.7 shows the current and corresponding baseline signals provided by $A_2 - S_5$, to observe that magnitudes of both S_0 and A_0 modes in the current signal are much weaker than those in the baseline signal. Such a reduction in magnitude can be attributed to the fact that path $A_2 - S_5$ right passed through partial of the damage, and both S_0 and A_0 modes captured via this sensing path were modulated by the damage significantly. This led to a relatively small correlation coefficient ($\rho_{XY} = 0.891$) between the current and baseline signals. Using Eq. 4.1, the field values (the second genre) at pixels along all physical pitch-catch paths were calculated.

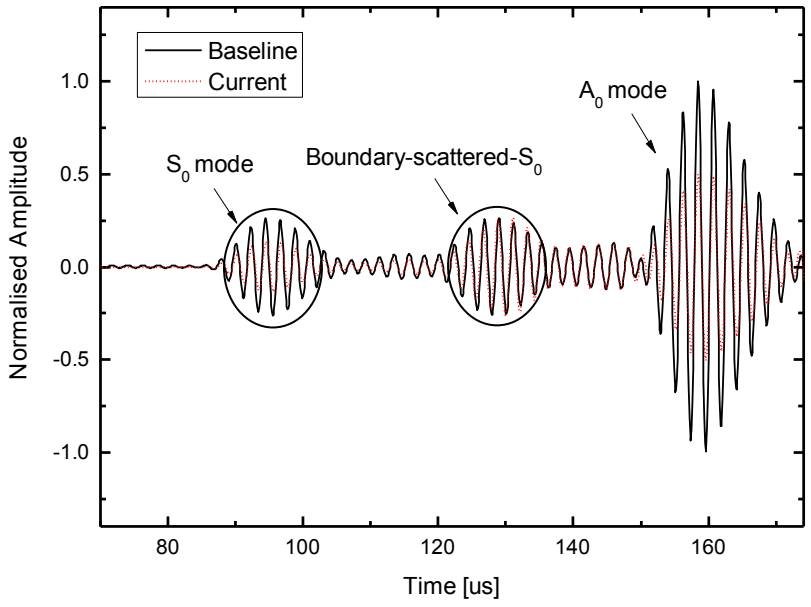

Fig. 4.7. Current and baseline signals acquired via pitch-catch sensing path $A_2 - S_5$ (normalised by the magnitude extremum of baseline signal)

Further, with the concept of '*virtual sensing*', for every single actuator, the field values at pixels along all virtual sensing paths radiated from this actuator were obtained by increasing α with a small increment (1^0 in this study), following the mechanism described by Eq. 4.3. Every physical or virtual path contributed a probability image, respectively, and all of them were aggregated for this actuator, as detailed in Section 4.3. By way of illustration, Fig. 4.8 exhibits a typical probability image when A_2 served as the actuator and $\alpha_{virtual}$ varied in the range of $[0, \pi]$ with an increment of 1^0 relative to $x-$axis, based on the concept of '*virtual sensing*' and known field values along physical sensing paths $A_2 - S_j$ ($j = 1,\ 3, \cdots,\ 7,\ 8$).

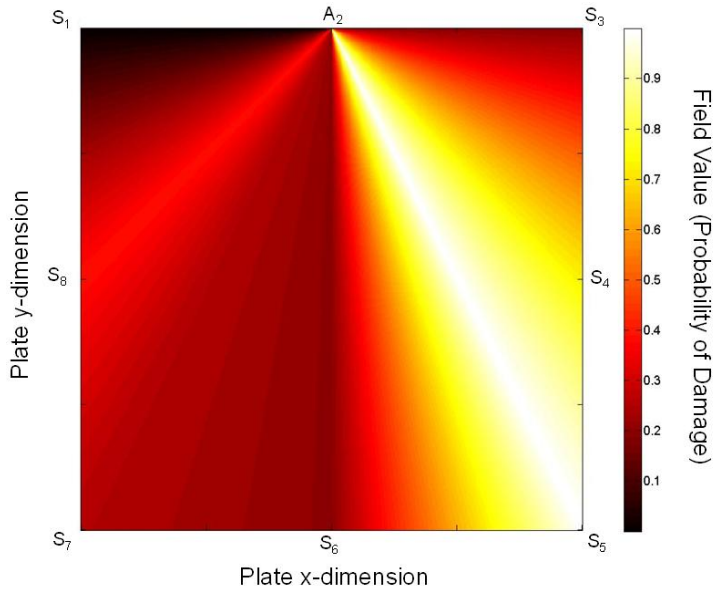

Fig. 4.8. Source image established by physical sensing paths $A_2 - S_j$ ($j = 1,\ 3, \cdots,\ 7,\ 8$) and virtual sensing paths (diagram showing inspection area only covered by the sensor network)

Applied with the hybrid image fusion scheme defined by Eq. 4.4, all source images established by pulse-echo paths and pitch-catch sensing paths in the sensor network were fused and the ultimate resulting image is shown in Fig. 4.9(a). For comparison, source images provided by sole pulse-echo paths and by sole pitch-catch sensing paths, respectively, were also fused in accordance with the arithmetic fusion scheme as,

$$P_{pulse-echo} = \frac{1}{N}\sum_{i=1}^{N} I_i' \Big|_{I} \qquad \text{(for } N \text{ pulse-echo pairs),} \qquad \textbf{(4.5a)}$$

$$P_{pitch-catch} = \frac{1}{N}\sum_{i=1}^{N} I_i \Big|_{II} \qquad \text{(for } N \text{ actuators).} \qquad \textbf{(4.5b)}$$

where $P_{pulse-echo}$ and $P_{pitch-catch}$ are the field values in their respective ultimate resulting images, shown in Figs. 4.9(b) and (c). It can be seen that the fusion using sole pulse-echo pairs, Fig. 4.9(b), enables an approximate depiction of the damage shape by roughly highlighting the orientation of two crack edges, but many pseudo damage locations (false alarm) are included in the image; the one using sole pitch-catch sensing paths, Fig. 4.9(c), on the whole pinpoints the location of damaged zone, but fails to describe the damage shape under the interference of a great deal of noise (pseudo damage locations). The unsatisfactory identification results in Figs. 4.9(b) and (c) are attributable to the nature of arithmetic fusion in Eq. 4.5, through which all prior perceptions from individual sensing paths in the sensor network including noise are equally amalgamated and reflected in the fused images. With an increase in involved sensing paths (more source images), damage-associated information is de-emphasised

and meanwhile noise/uncertainties irrelevant to damage stand out in the ultimate resulting image. In contrast, the hybrid fusion, Fig. 4.9(a), is able to accurately highlight the location, orientation, shape and size of two individual crack edges, efficiently screening false alarms. Such a capacity of hybrid fusion is due to the facts that (i) the arithmetic fusion in the scheme guarantees a full inclusion of prior perceptions from all individual source images; and (ii) the conjunctive operation further remains the commonality in various source images (damage-associated signal features) and filters random components (noise in individual source images).

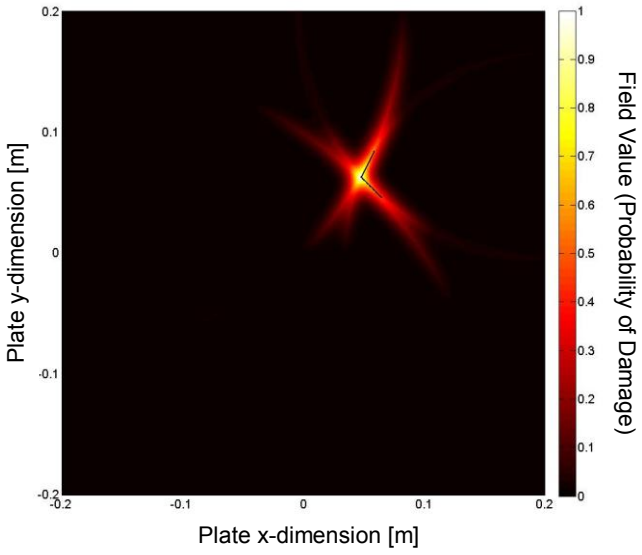

(a)

Fig. 4.9. Ultimate resulting images for L-shape crack using (a) hybrid fusion scheme (b) sole pulse-echo paths; and (c) sole pitch-catch sensing paths (diagram showing inspection area only covered by the sensor network; short black line: real edge of L-shape crack; white ellipse: area containing most pseudo damage locations)

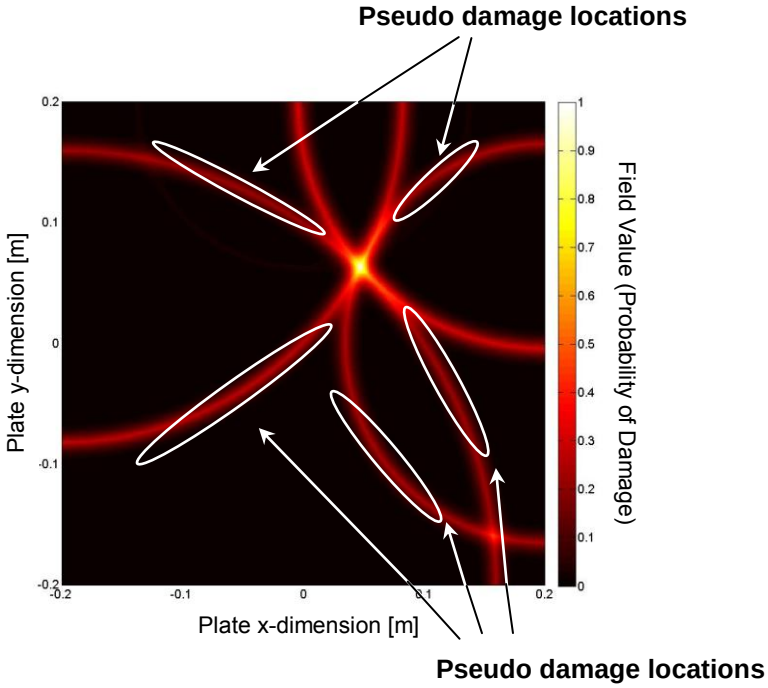

(b)

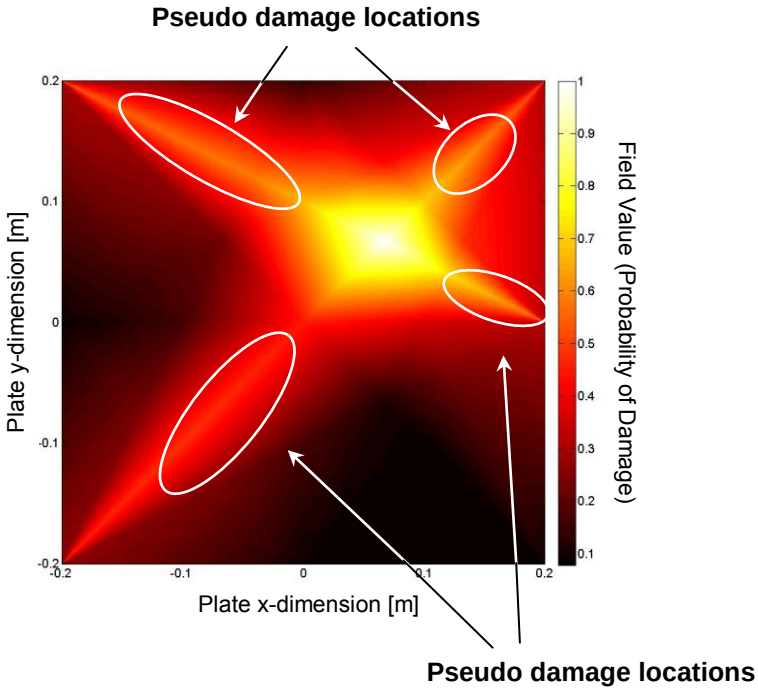

(c)

Fig. 4.9. *Cont.*

4.4.2 Polygonal Damage (Multi-edge Damage)

As an extension of the above application, the approach was used to identify polygonal damage formed by five edges (Edges I, II, III, IV and V) in an aluminium plate with the same dimensions and sensor network configuration as those in the above case, as seen in Fig. 4.10. Five damage edges have different lengths (25, 25, 21, 22 and 22 mm, respectively) and angles relative to $x-$axis (65^0, 133^0, 41^0, 92.5^0 and 168^0, respectively).

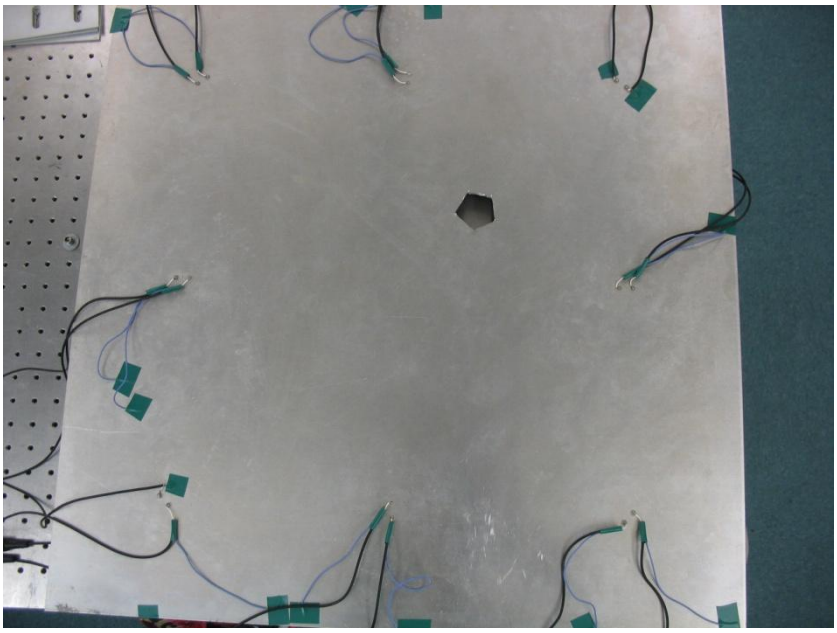

(a)

Fig. 4.10. (a) The aluminium specimen used in experiment with polygonal damage and (b) its schematic showing configuration of sensor network (unit: mm) (PZT wafers in the sensor network being symmetric relative to $x-$ and $y-$axes)

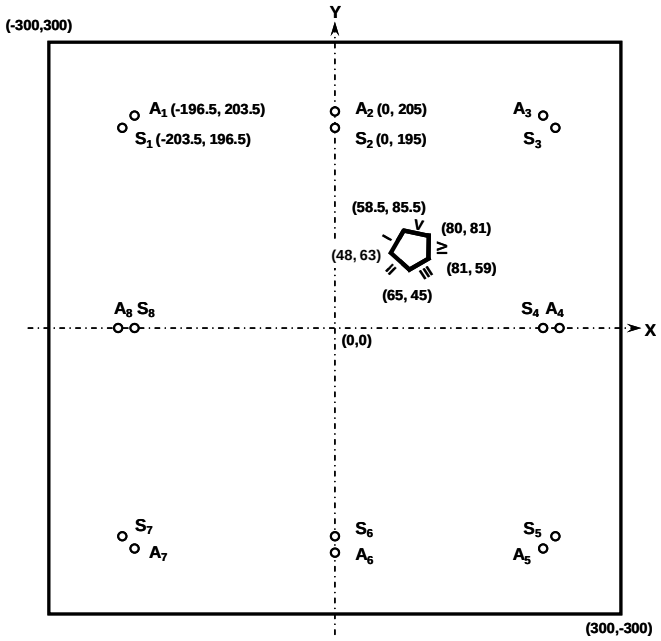

(b)

Fig. 4.10. *Cont.*

Fused image using the sole pulse-echo paths is displayed in Fig. 4.11, rendering limited description of the damage shape by highlighting Edges I, II and III only, and including abundant pseudo damage (false alarm). The pseudo damage can be seen to even hold higher probabilities of presence than the actual damage (reflected by the higher field values (the first genre) at pixels in those circled areas). Such a deficiency of fusion indicates that the effectiveness of the approach may be jeopardised if only the information acquired via pulse-echo pairs is relied on.

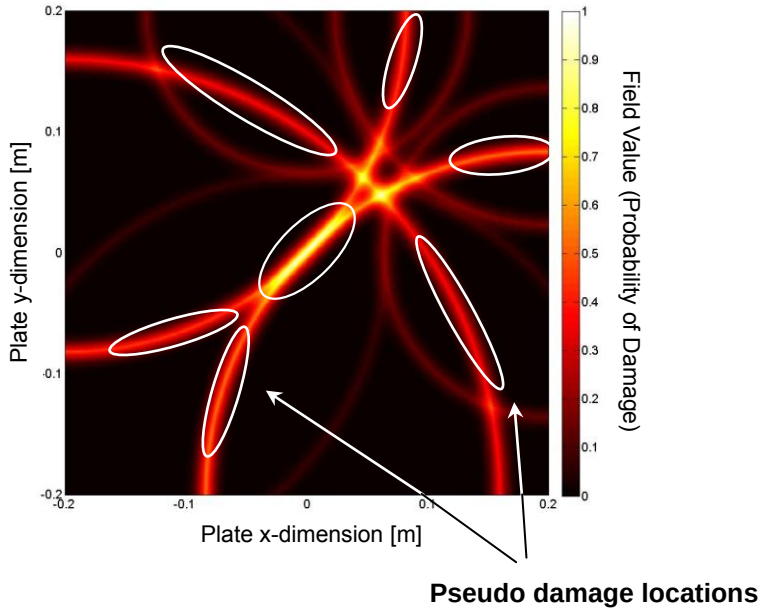

Fig. 4.11. Ultimate resulting image for polygonal damage using sole pulse-echo paths (diagram showing inspection area only covered by the sensor network; white ellipse: area containing most pseudo damage locations)

In parallel, fused images using the sole pitch-catch sensing paths without and with the assistance of '*virtual sensing*' are displayed in Figs. 4.12(a) and (b), respectively. In Fig. 4.12(a), pixels along physical paths, $A_1 - S_4$, $A_2 - S_5$ and $A_3 - S_7$ can be seen to hold higher field values (the second genre), implying higher possibility of damage presence along these three sensing paths. As commented previously, the way to define the second genre of field value in terms of Eq. 4.1 makes a sensing path very sensitive to the damage near it only, while highly inert to damage which is distant from it. When fused with other pitch-catch paths, these three sensing paths became dominant, whilst noise included in their source images also became pronounced. With the limited but noisy information, the identified results in Fig. 4.12(a) fail to quantitatively describe the

multi-edge damage.

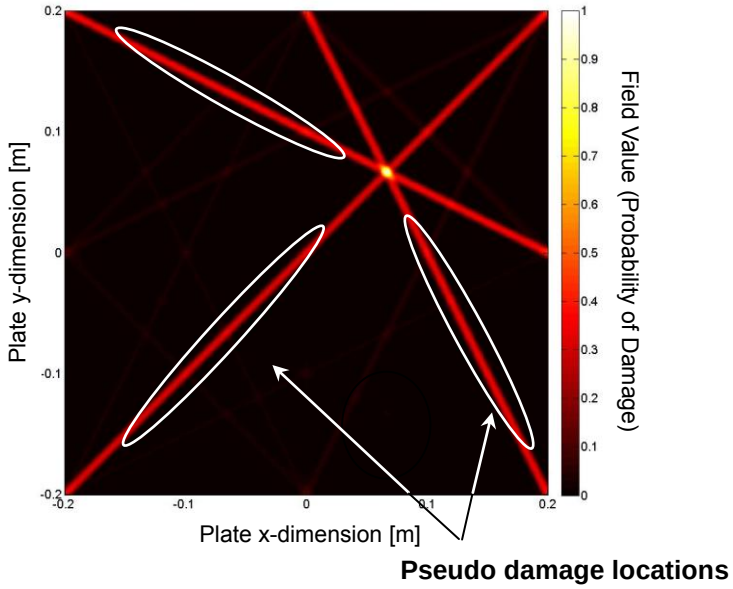

(a)

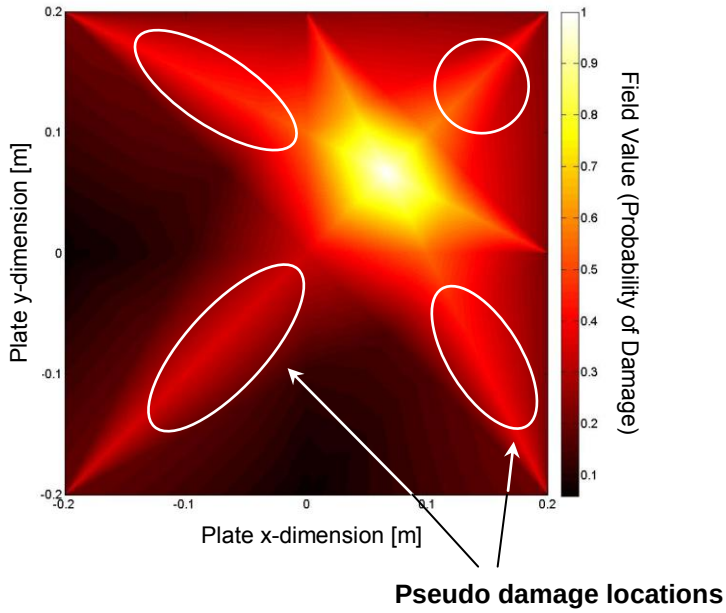

(b)

Fig. 4.12. Ultimate resulting image for polygonal damage using sole pitch-catch sensing paths (a) without and (b) with the assistance of *virtual sensing* (diagram showing inspection area only covered by the sensor network; white ellipse: area containing most pseudo damage locations)

With the concept of '*virtual sensing*', the sensor network was virtually densified. As a direct result, prior perceptions from individual source images were well decentralised and noise was largely removed. As seen in Fig. 4.12(b), apart from an indication of damage location, an approximate depiction of size of the polygonal damage was also achieved. However, although virtual sensing paths can be used to compensate for the insufficiency of input data, the fusion using sole pitch-catch paths does not have a capacity of pinpointing individual damage edges, and the predicted damage shape shown in Fig. 4.12(b) largely deviates from the reality.

With the hybrid fusion scheme, Fig. 4.13(a) shows the ultimate resulting image, to observe that the common perceptions of individual sources images were intensified, whilst noise in each source images was suppressed considerably. Furthermore, if 50% of the maximum field value in the ultimate resulting image is set as a threshold for a definitive conclusion that damage occurs, the shape of the polygonal damage can be clearly captured, in Fig. 4.13(b), upon forcing all field values which are less than this threshold to be zero. Although Edges I, II and III of the polygonal damage are highlighted, it is noteworthy that Edges IV and V are still unidentifiable. This is due to the fact (from the conclusions of preparatory study detailed in Section 2.3) that the orientation-specific damage (individual damage edge in this case) possesses a sensitive region in which the angle of wave incidence (θ in Fig. 2.3) is sufficiently small so as to ensure the damage-scattered wave energy to be captured efficiently. According to Figs.

2.6 and 2.11, the sensitive regions of Edges IV and V are indicated in Fig. 4.14. With the current sensor network configuration, there is no any actuator-sensor path directly passing through the sensitive regions of Edges IV and V, making it difficult to identify these two edges.

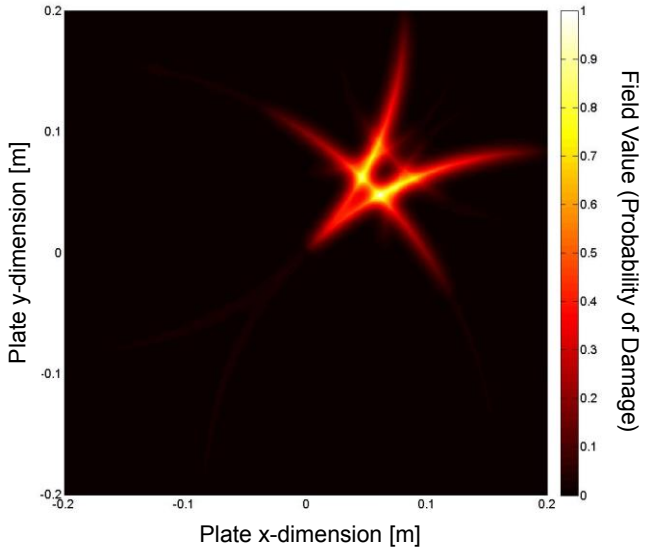

(a)

Fig. 4.13. (a) Ultimate resulting image for polygonal damage using hybrid fusion scheme; and (b) the image in (a) upon applying a threshold of 0.5 (diagram showing inspection area only covered by the sensor network; short black line: real edge of polygonal damage)

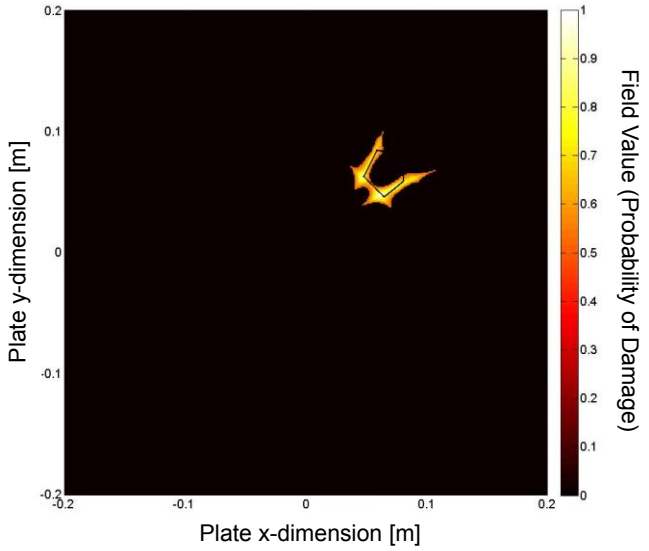

(b)

Fig. 4.13. *Cont.*

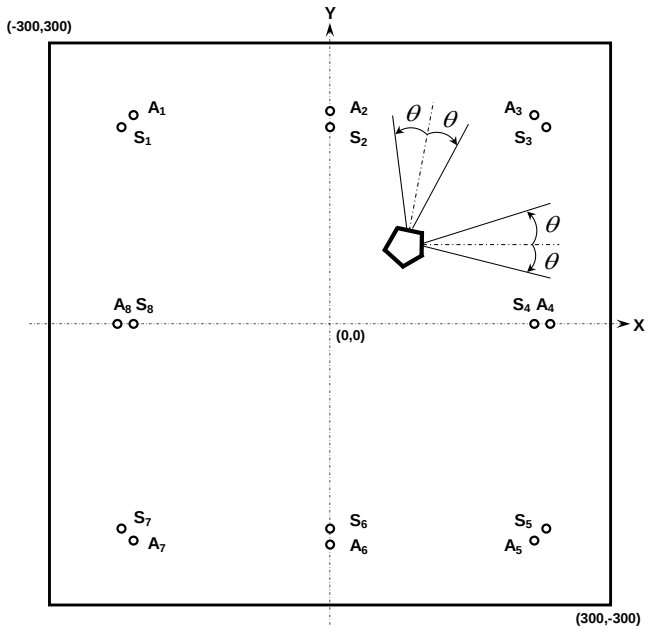

Fig. 4.14. Schematic of sensitive area of Edges IV and V

4.4.3 Multi-damage

To quantitatively identify multi-damage within the same inspection area is often a tanglesome task for most existing Lamb-wave-based NDE and SHM due to the challenge in interpreting complex wave scattering phenomena from multi-damage. To examine the feasibility of the developed PDI approach in identifying multi-damage, the aluminium panel bearing the polygonal damage used in the above case was further introduced with a through-thickness crack, referring to Fig. 4.15 (20 mm in length and 0.64 mm in width).

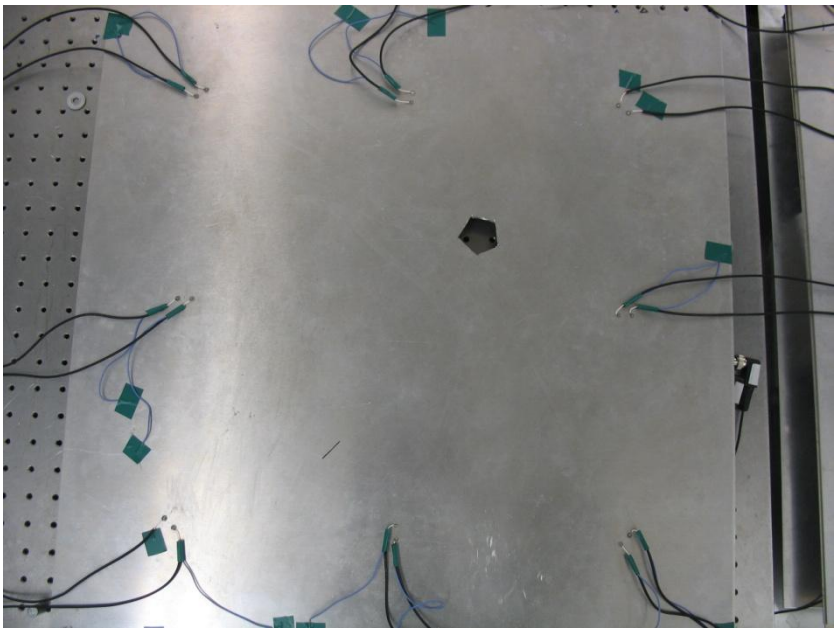

(a)

Fig. 4.15. (a) The aluminium specimen used in experiment with multiple damage and (b) its schematic showing configuration of sensor network (unit: mm) (PZT wafers in the sensor network being symmetric relative to $x-$ and $y-$axes)

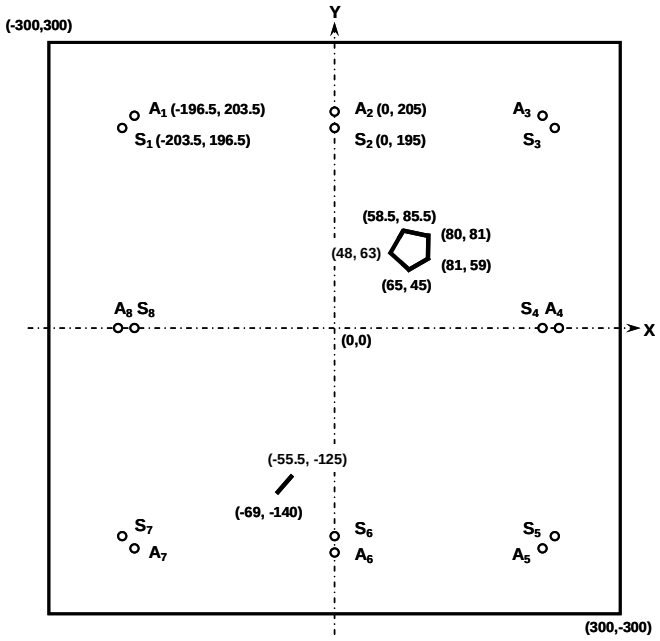

(b)

Fig. 4.15. *Cont.*

In the approach, natures of the first and second genres of field value endow the sensing paths in a sensor network to apperceive the damage near them only. Such a trait can be beneficial to detecting multi-damage. For example, in this case, actuator-sensor pairs, $A_1 - S_1$ and $A_1 - S_4$ can offer crucial information for the polygonal damage, while pairs $A_8 - S_8$ and $A_6 - S_8$ can provide information regarding the crack. Furthermore, with the concept of '*virtual sensing*', this active sensor network with eight actuator-sensor pairs was expanded virtually, able to provide larger coverage, avoiding insufficient acquisition of information. With the hybrid image fusion scheme, the ultimate resulting image is exhibited in Fig. 4.16(a). Similar as in Section 4.4.2, with a threshold (50% of the maximum field value in the image), the multi-damage can

be identified accurately and quantitatively, in Fig. 4.16(b), including damage locations, shapes and sizes, matching well the reality.

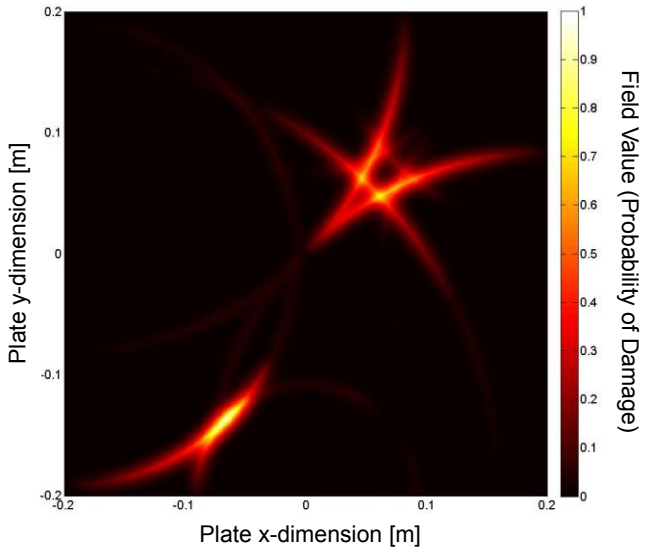

(a)

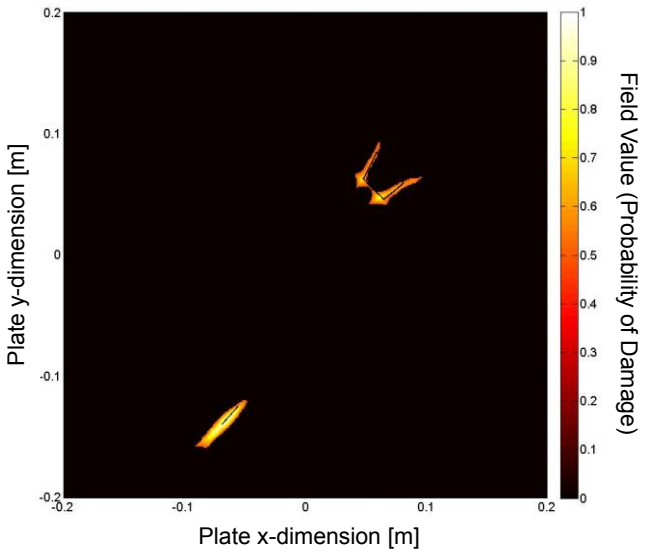

(b)

Fig. 4.16. (a) Ultimate resulting image for multi-damage using hybrid fusion scheme; and (b) the image in (a) upon applying a threshold of 0.5 (diagram showing inspection area only covered by the sensor network; short black line: real edge of damage)

In all the above three applications, it can be seen that the image fusion plays an essential role in the PDI approach in screening unwanted signal features and standing out damage-associated features. It greatly enhances the tolerance and robustness of the PDI technique to measurement noise and uncertainties, as well as erroneous perceptions from individual sensing paths.

4.5 Enhanced Diagnostic Imaging

Basically, the developed PDI approach exploits features extracted from captured Lamb wave signals rendered by a sensor network consisting of both the pulse-echo and pitch-catch configurations. In pulse-echo configuration, signal features including ToF and intensity of signal energy are used to establish field values; while in pitch-catch configuration, signal correlation coefficients are applied. Through experimental validation detailed in the above sections, it can been seen that the approach demonstrates good properties in predicting damage location, shape and size *etc.* Nevertheless, as shown in Fig. 4.14, existence of sensitive region for a particular damage orientation may fairly lower the resolution and accuracy of the approach, posing difficulty on the detection of damage with arbitrary orientation. To relieve such an issue, a relative dense sensor network has to be used.

To overcome such a deficiency by using sparse sensors, an enhanced PDI approach was further developed, from which signal features associated with ToF and signal intensity of captured waves from pitch-catch configuration were further employed to develop field values (Note in previous sections, only correlation coefficients were used to develop field values in pitch-catch configuration, while ToF and signal intensity were used in pulse-echo configuration).

4.5.1 Principle

Similar as the principle described in Section 3.2, ToF and intensity of damage-scattered energy were employed to develop field values for pitch-catch configuration (in Section 3.2, ToF and intensity of scattered energy were used for pulse-echo configuration only). Consider a sensor network consisting of N pairs of actuator and sensor as shown in Fig. 4.17(a). Without losing the generality, focusing on a pitch-catch path, $A_i - S_j$, a local coordinate system can be established as in Fig. 4.17(b), where actuator A_i is at the origin, and the centre of the damage is presumed at (x_D, y_D). A set of nonlinear equations can thus be established for individual pitch-catch paths, as

$$(\frac{L_{A_i-D}}{V} + \frac{L_{D-S_j}}{V}) - \frac{L_{A_i-S_j}}{V} = \Delta t_{i-j} \qquad (i, j = 1,\ 2,\ \cdots,\ N \text{, but } i \neq j), \qquad \textbf{(4.6)}$$

where

$$L_{D-S_j} = \sqrt{(x_D - x_j)^2 + (y_D - y_j)^2}\,, \quad L_{A_i-D} = \sqrt{x_D{}^2 + y_D{}^2}\,, \quad L_{A_i-S_j} = \sqrt{x_j{}^2 + y_j{}^2}\,.$$

In the above, Δt_{i-j} is the difference between the ToF for the incident wave to propagate from actuator A_i to the damage and then to sensor S_j, and the ToF for the incident wave to propagate directly from actuator A_i to sensor S_j. L_{A_i-D}, L_{D-S_j} and $L_{A_i-S_j}$ represent the distances between actuator A_i located at (0,0) and the damage centre (x_D, y_D), the damage centre and sensor S_j located at (x_j, y_j), and A_i and S_j, respectively. Eq. 4.6 depicts a series of ellipse-like loci with A_i and S_j being two foci, indicating possible damage locations.

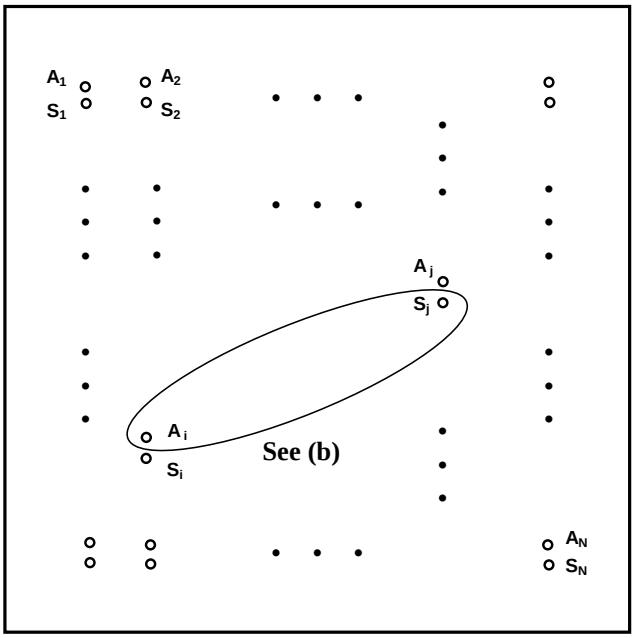

(a)

Fig. 4.17. (a) An active sensor network consisting of N pairs of actuator and sensor; and (b) relative positions among actuator A_i, sensor S_j and damage in the local coordinate system for pitch-catch path $A_i - S_j$

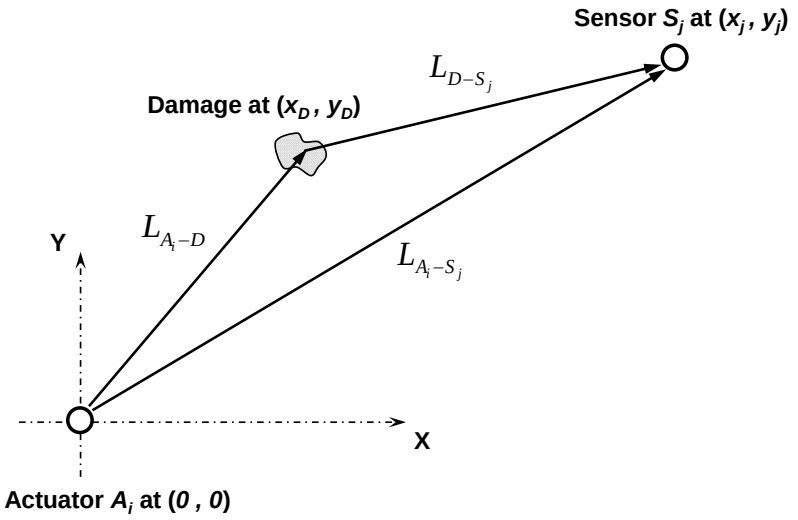

(b)

Fig. 4.17. *Cont.*

Meshing the structure under inspection using $L \times K$ nodes virtually (each mesh node is exclusively corresponding to a pixel of the probability image). The same as the method described in Section 3.2, field value at each pixel can be calculated using Eq. 3.4. With field values of all $L \times K$ pixels, a probability image established by such a pitch-catch path can be obtained, exemplarily shown in Fig. 4.18. In the image, the lighter a pixel in the greyscale image is, the greater the possibility of damage existing at that pixel. Note, the probability image established by a pulse-echo path is like a circle (Fig. 3.4), while the probability image established by a pitch-catch path is an ellipse-like locus (Fig. 4.18).

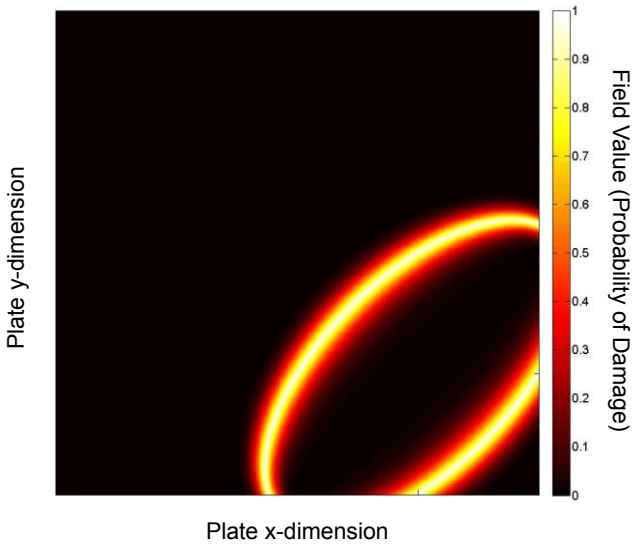

Fig. 4.18. A probability image established by a pitch-catch path using the ToF-based field value

Now, an active sensor network as shown in Fig. 4.17(a) offers three genres of information related to damage:

(i) Pulse-echo configuration offers ToF-based and signal energy intensity-based information for defining field value using Eq. 3.4;

(ii) Pitch-catch configuration offers correlation coefficient-based information for defining field value using Eq. 4.3; and

(iii) Pitch-catch configuration offers ToF-based and signal energy intensity-based information for defining field value using Eq. 3.4.

All the above information provided by the active sensor network is then amalgamated using a synthetic image fusion scheme as flowcharted in Fig. 4.19.

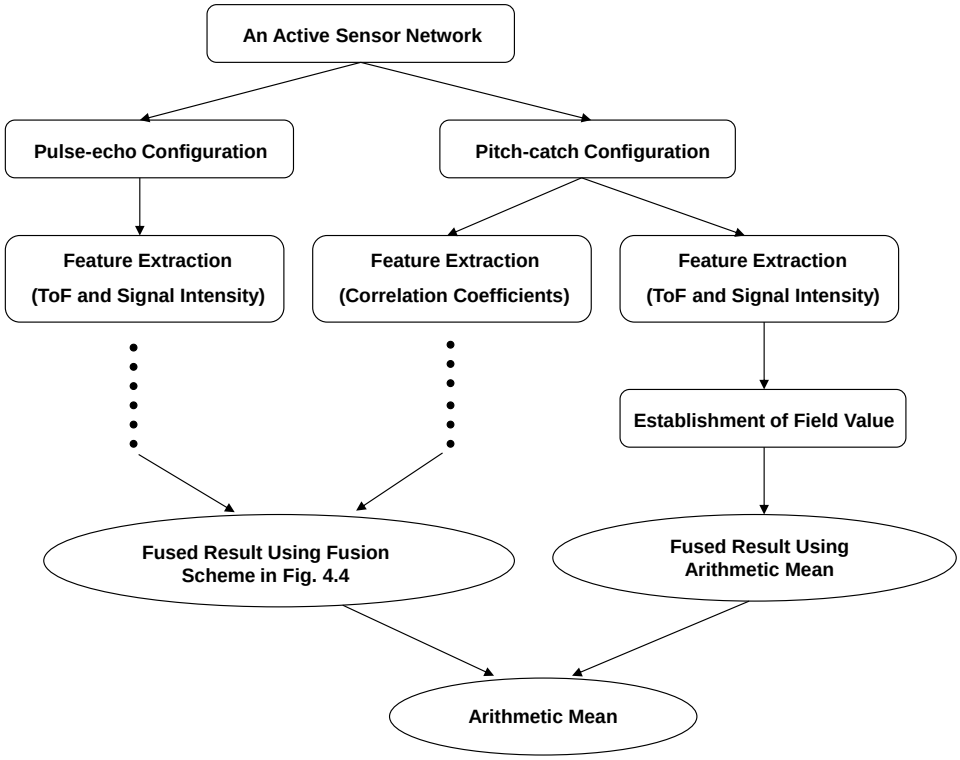

Fig. 4.19. Synthetic image fusion scheme

4.5.2 Application

To demonstrate the effectiveness of the enhanced PDI approach, the sensor network configuration in Fig. 4.15 was changed by abandoning four PZT wafers A_8, S_8, A_6 and S_6, as shown schematically in Fig. 4.20. In this way, a new specimen configuration with less sensors were formed.

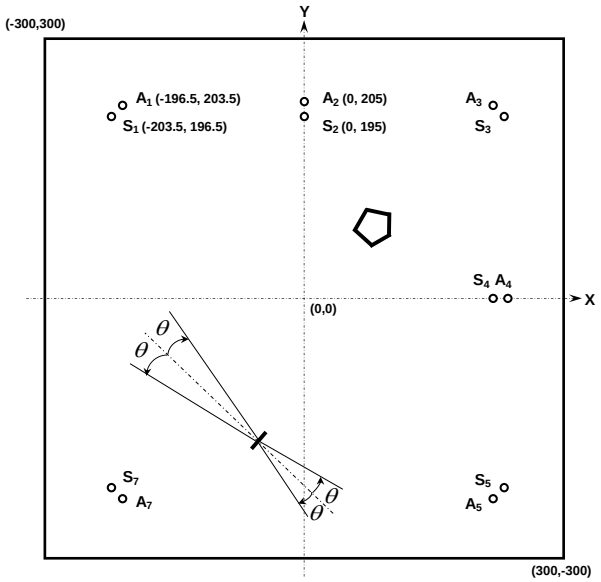

Fig. 4.20. Specimen configuration consisting of twelve PZT wafers

Ultimate diagnostic result using image fusion scheme introduced in Fig 4.4 is shown in Fig. 4.21. It can be seen that, the polygonal damage can still be clearly identified, but not the case for crack. This is due to the fact that no sensors are located in sensitive regions of the crack (indicated in Fig. 4.20), making determination of crack problematic.

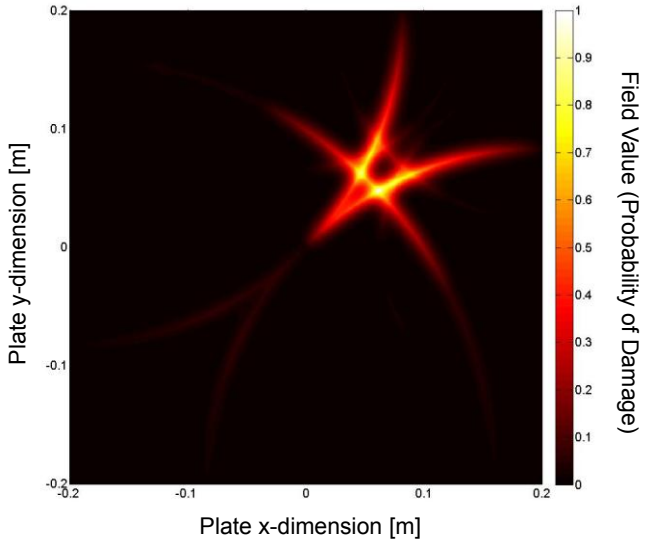

Fig. 4.21. Ultimate diagnostic result using image fusion scheme introduced in Fig. 4.4 (diagram showing inspection area only covered by the sensor network)

Ultimate diagnostic result using image fusion scheme introduced in Fig. 4.19 is shown in Fig. 4.22(a). Similar as Section 4.4.3, with a threshold (20% of the maximum field value in the image), both the polygonal damage and the crack can be seen in Fig. 4.22(b). The improved identification results, compared with those shown in Fig. 4.21 has demonstrated that an improvement in detection accuracy has been achieved using the enhanced PDI approach, without sacrificing the merits of PDI technique (using much less sensors compared with traditional imaging approach such as tomography). Actually in the above application, although fewer sensors were used, satisfactory identification has still been achieved.

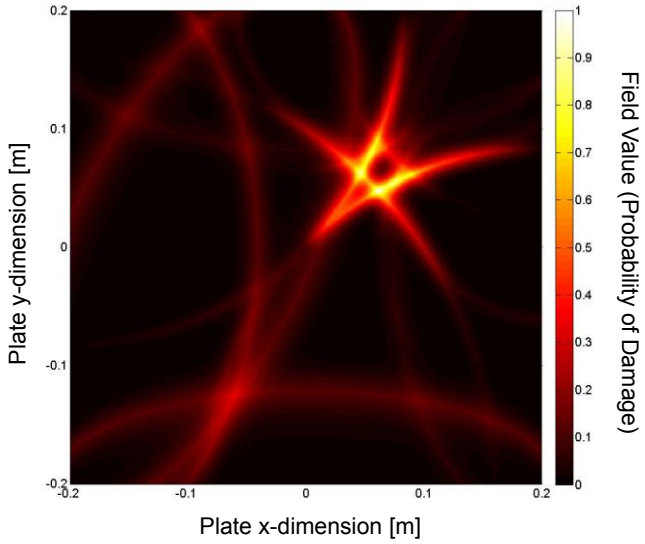

(a)

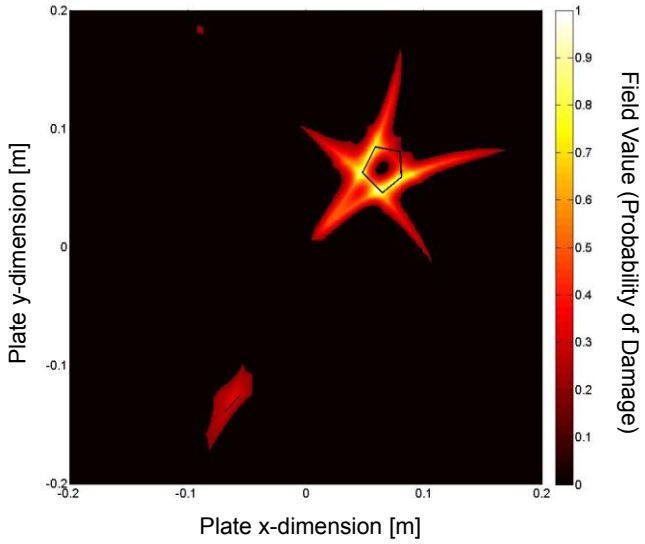

(b)

Fig. 4.22. (a) Ultimate diagnostic result using image fusion scheme introduced in Fig. 4.19; and (b) the image in (a) upon applying a threshold of 0.2 (diagram showing inspection area only covered by the sensor network; short black line: real edge of damage)

The improvement of the diagnostic result can be attributable to: a) more signal features (ToF and signal intensity of captured waves in pitch-catch configuration) were extracted to develop field value, therefore providing more information for damage identification; b) damage-scattered waves captured in pitch-catch configuration do not present strong orientation nature in terms of Figs. 2.6 and 2.11, therefore the crack can still be captured, despite that there is no any sensing paths passing through the sensitive region of the crack.

4.6 Concluding Remarks

In this chapter, hybrid signal features including ToF, intensity of signal energy and signal correlation were extracted from captured Lamb wave signals with the assistance of an active sensor network in line with both pulse-echo and pitch-catch configurations and a novel concept of '*virtual sensing*', which were then integrated to develop a retrofitted PDI approach. A hybrid image fusion scheme was developed, able to enhance the tolerance of the PDI approach to measurement noise and possible erroneous perceptions from individual sensing paths. Accurate identification results for three typical damage cases (L-shape through-thickness crack (strong orientation-specific damage), polygonal damage (multi-edge damage) and multi-damage in aluminium plates) have demonstrated the effectiveness of the developed PDI approach in quantitatively visualising structural damage, regardless of

its shape and number, by highlighting its individual edges in an easily interpretable binary image. Conclusions have also articulated that a judicious selection of fusion scheme is crucial for a PDI technique to deliver precise and accurate identification.

Improvement on the developed PDI approach by involving additional signal features extracted from pitch-catch configuration has demonstrated that rich information can facilitate the enhancement of the accuracy and precision of an imaging technique. This implies that it is of vital importance to take full advantage of a sensor network for signal feature extraction.

CHAPTER 5 Conclusions and Future Research Recommendations

5.1 Concluding Remarks

In recent years, diagnostic imaging-based NDE and SHM techniques in conjunction with the use of Lamb waves have attracted increasing attention because such techniques generate intuitional and easy interpretation 2D or 3D images, capable of intuitively indicating the structural damage details and even overall health state of the structure under inspection. But as envisaged, traditional diagnostic imaging techniques such as Lamb wave tomography are at the expense of a large number of sensors for image tomographic reconstruction, fairly narrowing their potentials towards automated online SHM. This deficiency has entailed rapid development of novel imaging techniques using less sensors and quicker image reconstruction algorithms, and of particular interest is the probability-based diagnostic imaging (PDI). However, most existing PDI approaches solely explore changes in signal characteristics of ToFs extracted from captured Lamb wave signals, which are actually insensitive to the variation of damage shape/size. As a result, these approaches are unwieldy to estimate

the damage shape and size quantitatively. On the other hand, the orientation-specific or sharp-angled damage such as a crack or a notch poses a challenging issue to Lamb-wave-based damage identification. Different from damages with relatively smooth edges such as through-holes and delamination, orientation of damage with sizable length in a particular dimension may exert significant influence on the incident Lamb waves. Quantitatively examining such damage is still problematic.

Bearing in mind the aforementioned challenges, a PDI technique with the assist of active sensor network and imaging reconstruction algorithm was developed in this thesis, to revamp traditional SHM approaches.

The general philosophy of the PDI is illustrated in Fig. 5.1, from which signal features including ToF, signal intensity and correlation coefficients were appropriately fused with the assistance of a synthetic image fusion scheme. In terms of the correlations between a) ToF and damage location, (b) intensity of signal energy and damage orientation/shape, and c) signal correlation and damage location, the developed PDI approach is expected to be able to quantitatively depict damage status including location, shape and even size.

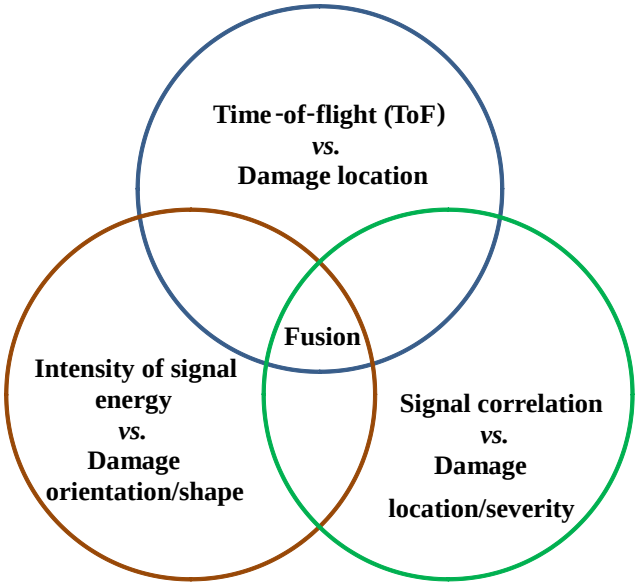

Fig. 5.1. Illustration of the philosophy to develop PDI

Prior to proceeding to details of approach development, three fundamental studies were accomplished:

(1) Effect of the orientation of damage with sizable length in a particular dimension (orientation-specific damage) on Lamb wave propagation;

(2) attenuation of Lamb waves and appropriate compensation, and

(3) influential area of damage on a particular actuator-sensor path for capturing Lamb wave signals.

It was observed that:

(1) Crack orientation has a prominent influence on Lamb wave propagation, in which strongest reflection is captured with normal incidence. With the increase of angle of wave incidence, the intensity of crack-reflected signal energy quickly

decreases. Thus, the intensity of damage-reflected wave energy can be a sensitive indicator to damage orientation;

(2) Lamb waves in a thin aluminium plate attenuate at a rate that is approximately proportional to the inverse square root of the propagation distance;

(3) The influential area of a damaged zone on a particular sensing path is comparable to the wavelength of the wave propagating along this sensing path.

Based on the above fundamental studies, two PDI methods were developed. The first method relies on the established relationship between (i) temporal information and damage location, and ii) intensity of signal energy and damage orientation/shape, with the assistance of an active sensor network in line with sole pulse-echo configuration; while the second method relies on the established relationship between (i) temporal information and damage location, (ii) intensity of signal energy and damage orientation/shape, and (iii) signal correlation and damage location/severity, with the assistance of an active sensor network in conformity to hybrid pulse-echo and pitch-catch configurations, supplemented with a concept of '*virtual sensing*'.

Using the first method, damage location, orientation of individual edges of damage can be estimated, facilitating quantitative description of damage shape. To enhance the robustness and tolerance to measurement noise/uncertainties and avoid possible erroneous perceptions from particular sensing paths, a two-level synthetic image fusion

scheme was developed. The effectiveness of this approach was demonstrated by predicting orientation-specific damage including a triangular through-thickness hole (through FE simulation) and a through-thickness crack (through experiment) in aluminium plates. The results, highlighted in intuitional and easily interpretable images, have shown satisfactory accuracy of the developed approach for identifying orientation-specific damage.

However, when dealing with some orientation-specific damage such as L-shape crack, measurement noise may overwhelm damage-related information, impairing detection accuracy and prevision. To circumvent such deficiency, the second PDI method was developed, in which hybrid signal features including ToF, intensity of signal energy and signal correlation were extracted from captured Lamb wave signals with the assistance of an active sensor network in line with both pulse-echo and pitch-catch configurations. A novel concept of '*virtual sensing*' was then integrated to enrich sensing information. A hybrid image fusion scheme was developed, able to enhance the tolerance of the PDI approach to measurement noise and possible erroneous perceptions from individual sensing paths. Accurate identification results for three typical damage cases (L-shape through-thickness crack (strong orientation-specific damage), polygonal damage (multi-edge damage) and multi-damage in aluminium plates) have demonstrated the effectiveness of the developed PDI approach in quantitatively visualising structural damage, regardless of

its shape and number, by highlighting its individual edges in an easily interpretable binary image. It was also observed that a judicious selection of fusion scheme is crucial for a PDI technique to ensure precise and accurate identifications.

Integrating (i) temporal information (subject to location of damage) with (ii) intensity of damage-reflected wave signal (serving as a sensitive indicator to damage orientation), the developed PDI approach using pulse-echo configuration (the first method) is endowed with an enhanced capacity to portray damage quantitatively including orientation of its edges, whereby damage shape can further be ascertained if the damage is deemed as a continuum of a series of cracks. But, orientation-specific damage possesses a sensitive region in which the angle of wave incidence is sufficiently small so as to ensure the damage-reflected wave energy to be captured efficiently. In other words, if there were no any sensor located in the sensitive regions, the damage may not be identified. To overcome such deficiency, pitch-catch configuration was also included to form hybrid pulse-echo and pitch-catch configurations, and more signal features including correlation coefficients are extracted for damage identification. Though with the same sensor density, the enhanced PDI approach using hybrid pulse-echo and pitch-catch configurations (the second method) offers more satisfactory identification results than the PDI approach using sole pulse-echo configuration.

5.2 Research Recommendations

Although promising results have been achieved using the developed PDI approaches, there are still many challenging issues to be explored in future work:

First, in this study, major attention was directed to develop diagnostic imaging methods. In the next step, the developed diagnostic imaging methods will be applied to detect more types of real world damage (surface crack, corrosion, delamination *etc.*). No matter what type of damage it is, it will cause variations in acoustic impedance. Variations in acoustic impedance will cause wave scattering phenomena such as reflection, transmission, diffraction, and mode conversion *etc.* It is just these features that are used in the thesis to detect damage.

Second, major attention was directed to the detection of linear macroscopic damage in the thesis, *e.g.* a notch, an L-shape through-thickness crack. It is based on the linear wave scattering phenomena (*e.g.*, wave reflection, transmission, mode conversion). However real damage in engineering structures initiates from microscopic damage, *i.e.* fatigue crack under cyclic loading, presenting highly nonlinear features. Such type of damage may not be detected efficiently using traditional approaches based on linear wave scattering. It is of great significance but a great challenge to identify fatigue cracks in engineering structures in an early stage. The future work will be focused on nonlinear fatigue crack in metallic structures. In recognition of the fact that nonlinear

phenomena caused by fatigue crack under cyclic loading can be best reflected by nonlinear characteristics of dynamic signals, a NDE and SHM technique can be developed with the particular capacity of identifying orientation-specific fatigue cracks, by combining results arising from this study and nonlinearities of higher-order acousto-ultrasonic (AU) waves. Two major approaches are recommended: (i) modulation of higher-order AU waves (high-frequency and weak in energy) by spontaneous or inherent structural vibration (low-frequency and high energy); and (ii) higher-order harmonic wave generation which is sensitive to the accumulation of fatigue damage. The developed PDI methods in this thesis will be integrated with the recommended techniques as above to detect fatigue crack, which is expected to be able to visualize damage in a quantitative (including location, orientation, and severity of fatigue crack), rapid and automatic manner.

Third, the developed PDI methods in the thesis are based on comparing current signals captured from the structure under inspection with baseline signals from intact counterpart. In practice, measurement conditions other than damage itself that may change captured Lamb wave signals should be considered. The most common environmental change is ambient temperature, which affects Lamb wave propagation by changing magnitude and ToF of captured Lamb wave signals. From the pioneer studies [102-104], there is no need to compensate for a small change in ambient temperature in normal applications; however, the influence of temperature cannot be

ignored if sensors work in an environment of elevated temperature. To increase the accuracy of damage identification in an environment with temperature variation, appropriate temperature compensation will be applied.

Fourth, the best way to overcome the problem mentioned above (environmental change) is to minimise the dependence of identification on baseline signals. In this aspect, two methods are recommended for future work: a) time-reversal is one solution towards this aspect [25, 105]. The keystone of this method is that, if damage exists in or near a particular wave acquisition path, time reversibility of wave signal captured via this path is broken down; otherwise, a captured wave signal can be time-reversed by changing the roles of actuator and sensor as if time are going backwards. b) another solution refers to a vibration modulation technique [106], *i.e.* using low-frequency, high amplitude vibration of the structure under inspection to modulate high-frequency Lamb wave signals. The subtraction is then made between different parts of an externally applied low-frequency vibration when it reaches its maximum and minimum in amplitude, which potentially overcomes the dependence of a baseline signal. In addition, a novel baseline-free method was recently reported [52]. In this method, mode conversion due to the interaction of Lamb wave with damage was extracted and employed to detect the damage.

Fifth, the developed PDI was used to inspect isotropic materials in the thesis. When Lamb waves travel in isotropic media, they propagate with the same velocity omnidirectionally and the wave front forms a circle. Nevertheless, this is not the case in anisotropic materials such as fibre-reinforced composites, in which the wave velocity is subject to the direction of propagation, making determination of damage location problematic. To enhance the capability of developed PDI approach towards real engineering applications, the effects of anisotropy of medium on propagation characteristics of Lamb waves will be studied and integrated into the PDI approach developed in the thesis. In addition, inspection of complex structures with additional features such as stiffeners is another challenging issue. More wave reflection may overwhelm damage-scattered wave therefore complicating signal interpretation. These issues will be investigated in future study.

In addition, to strengthen the uniqueness to the study, apart from numerical simulation and experimental study, theoretical study will be included to investigate influence of crack orientation on Lamb wave propagation.

REFERENCE

[1] J. L. Rose, "A baseline and vision of ultrasonic guided wave inspection potential," *Journal of Pressure Vessel Technology,* vol. 124, pp. 273-282, 2002.

[2] F. L. Degertekin and B. T. Khuri-Yakub, "Lamb wave excitation by Hertzian contacts with applications in NDE," *IEEE Transactions on Ultrasonics, Ferroelectrics and Frequency Control,* vol. 44, pp. 769-779, 1997.

[3] J. S. Popovics and J. L. Rose, "A survey of developments in ultrasonic NDE of concrete," *IEEE Transactions on Ultrasonics, Ferroelectrics and Frequency Control,* vol. 41, pp. 140-143, Jan 1994.

[4] H. Sakai, A. Minamisawa, and K. Takagi, "Effect of moisture content on ultrasonic velocity and attenuation in woods," *Ultrasonics,* vol. 28, pp. 382-385, Nov 1990.

[5] R. D. Shaffer, "Eddy current testing, today and tomorrow," *Materials Evaluation,* vol. 52, pp. 28-32, Jan 1994.

[6] S. Mukherjee, M. A. Morjaria, and F. C. Moon, "Eddy current flows around cracks in thin plates for nondestructive testing," *Journal of Applied Mechanics-Transactions of the Asme,* vol. 49, pp. 389-395, 1982.

[7] N. Ida, R. Palanisamy, and W. Lord, "Eddy current probe design using finite element analysis," *Materials Evaluation,* vol. 41, pp. 1389-1394, 1983.

[8] R. Zorgati, B. Duchene, D. Lesselier, and F. Pons, "Eddy current testing of anomalies in conductive materials, Part I: Qualitative imaging via diffraction tomography techniques," *IEEE Transactions on Magnetics,* vol. 27, pp. 4416-4437, Nov 1991.

[9] L. O. Goldberg, "Eddy current testing, an emerging NDT method for ferritic weld inspection," *Materials Evaluation,* vol. 56, pp. 149-152, Feb 1998.

[10] J. Gray and G.-R. Tillack, "X-ray imaging methods over the last 25 years-new advances and capabilities," *AIP Conference Proceedings,* vol. 557, pp. 16-32, 2001.

[11] D. R. Black, H. E. Burdette, R. C. Dobbyn, R. D. Spal, and M. Kuriyama, "Advanced X-ray imaging methods for ceramics," *American Ceramic Society Bulletin,* vol. 70, pp. 1004-1009, Jun 1991.

[12] R. P. Parker, "Medical applications of X-ray and gamma-ray imaging methods," *Nuclear Instruments & Methods in Physics Research Section a-Accelerators Spectrometers Detectors and Associated Equipment,* vol. 221, pp. 221-225, 1984.

[13] T. E. Gureyev, A. W. Stevenson, D. Paganin, S. C. Mayo, A. Pogany, D. Gao, and S. W. Wilkins, "Quantitative methods in phase-contrast X-ray imaging," *Journal of Digital Imaging,* vol. 13, pp. 121-126, May 2000.

[14] K. S. Hermanson and B. I. Sandor, "Corrosion fatigue modeling via differential infrared thermography," *Experimental Techniques,* vol. 22, pp. 19-21, May-Jun 1998.

[15] E. Grinzato, V. Vavilov, P. G. Bison, and S. Marinetti, "Hidden corrosion detection in thick metallic components by transient IR thermography," *Infrared Physics & Technology,* vol. 49, pp. 234-238, Jan 2007.

[16] J. Tyson, "Laser shearography for rapid nondestructive inspection," *Materials World,* vol. 4, pp. 521-522, Sep 1996.

[17] W. S. Burkle and B. K. Fraser, "The effect of mechanical paint removal on the detectability of cracks by visual, magnetic particle, and liquid dye penetrant testing," *Materials Evaluation,* vol. 45, pp. 874-875, Aug 1987.

[18] Y. Gao, R. Sandhu, G. Fichtinger, and A. R. Tannenbaum, "A coupled global registration and segmentation framework with application to magnetic resonance prostate imagery," *IEEE Transactions on Medical Imaging,* vol. 29, pp. 1781-1794, Oct 2010.

[19] P. D. Teal and M. A. Poletti, "Adaptive phase calibration of a microphone array for acoustic holography," *Journal of the Acoustical Society of America,* vol. 127, pp. 2368-2376, Apr 2010.

[20] M. Castaings and P. Cawley, "The generation, propagation, and detection of Lamb waves in plates using air-coupled ultrasonic transducers," *Journal of the Acoustical Society of America,* vol. 100, pp. 3070-3077, 1996.

[21] Z. Guo, J. D. Achenbach, and S. Krishnaswamy, "EMAT generation and laser detection of single Lamb wave modes," *Ultrasonics,* vol. 35, pp. 423-429, 1997.

[22] M. Z. Silva, R. Gouyon, and F. Lepoutre, "Hidden corrosion detection in aircraft aluminum structures using laser ultrasonics and wavelet transform signal analysis," *Ultrasonics,* vol. 41, pp. 301-305, Jun 2003.

[23] J.-B. Ihn and F.-K. Chang, "Detection and monitoring of hidden fatigue crack growth using a built-in piezoelectric sensor/actuator network: I. Diagnostics," *Smart Materials and Structures,* vol. 13, pp. 609-620, 2004.

[24] V. Giurgiutiu, A. Zagrai, and J. Jing Bao, "Piezoelectric wafer embedded active sensors for aging aircraft structural health monitoring," *Structural Health Monitoring,* vol. 1, pp. 41-61, 2002.

[25] H. Sohn, H. W. Park, K. H. Law, and C. R. Farrar, "Combination of a time reversal process and a consecutive outlier analysis for baseline-free damage diagnosis," *Journal of Intelligent Material Systems and Structures,* vol. 18, pp. 335-346, 2007.

[26] E. Robeson and B. Thompson, "Tools for the 21st century: MH-47E SUMS," in *Proceedings of the 2nd International Workshop on Structural Health Monitoring* Stanford, CA., USA, 1999, pp. 179-189.

[27] M. J. Iglesias and A. Palomino, "SHMS, a good chance to gain experience to optimise the aircraft structural capability," in *European COST F3 Conference on System Identification and Structural Health Monitoring* Madrid, Spain, 2000,

pp. 753-771.

[28] K.-y. Wong, C. K. Lau, and A. R. Flint, "Planning and implementation of the structural health monitoring system for cable-supported bridges in Hong Kong," in *Nondestructive Evaluation of Highways, Utilities, and Pipelines IV*, Newport Beach, CA, USA, 2000, pp. 266-275.

[29] V. Giurgiutiu and A. Cuc, "Embedded non-destructive evaluation for structural health monitoring, damage detection, and failure prevention," *The Shock and Vibration Digest,* vol. 37, pp. 83-105, 2005.

[30] G. Zhou and L. M. Sim, "Damage detection and assessment in fibre-reinforced composite structures with embedded fibre optic sensors-review," *Smart Materials and Structures,* vol. 11, pp. 925-939, 2002.

[31] K. S. C. Kuang, M. Maalej, and S. T. Quek, "An application of a plastic optical fiber sensor and genetic algorithm for structural health monitoring," *Journal of Intelligent Material Systems and Structures,* vol. 17, pp. 361-379, 2006.

[32] L. P. Kollar and R. J. Van Steenkiste, "Calculation of the stresses and strains in embedded fiber optic sensors," *Journal of Composite Materials,* vol. 32, pp. 1647-1679, 1998.

[33] P. J. Ellerbrock, "DC-XA structural health-monitoring fiber optic-based strain measurement system," in *Smart Structures and Materials 1997: Industrial and Commercial Applications of Smart Structures Technologies,* San Diego, CA, USA, 1997, pp. 207-218.

[34] O. S. Salawu, "Detection of structural damage through changes in frequency: a review," *Engineering Structures,* vol. 19, pp. 718-723, Sep 1997.

[35] Y. Zou, L. Tong, and G. P. Steven, "Vibration-based model-dependent damage (delamination) identification and health monitoring for composite structures - a review," *Journal of Sound and Vibration,* vol. 230, pp. 357-378, Feb 17 2000.

[36] Z. Su, L. Ye, and Y. Lu, "Guided Lamb waves for identification of damage in composite structures: a review," *Journal of Sound and Vibration,* vol. 295, pp. 753-780, 2006.

[37] T. Kundu, S. Das, and K. V. Jata, "Health monitoring of a thermal protection system using Lamb waves," *Structural Health Monitoring-an International Journal,* vol. 8, pp. 29-45, Jan 2009.

[38] Y. J. Yan, L. Cheng, Z. Y. Wu, and L. H. Yam, "Development in vibration-based structural damage detection technique," *Mechanical Systems and Signal Processing,* vol. 21, pp. 2198-2211, Jul 2007.

[39] A. Raghavan and C. E. S. Cesnik, "Review of guided-wave structural health monitoring," *The Shock and Vibration Digest,* vol. 39, pp. 91-114, 2007.

[40] P. Fromme, P. D. Wilcox, M. J. S. Lowe, and P. Cawley, "On the development and testing of a guided ultrasonic wave array for structural integrity monitoring," *IEEE Transactions on Ultrasonics, Ferroelectrics and Frequency Control,* vol. 53, pp. 777-785, Apr 2006.

[41] J. L. Rose, *Ultrasonic Waves in Solid Media*. New York: Cambridge University

Press, 1999.

[42] H. Lamb, "On waves in an elastic plate," *Proceedings of the Royal Society of London. Series A, Containing Papers of a Mathematical and Physical Character,* vol. 93, pp. 114-128, 1917.

[43] R. D. Mindlin and M. A. Medick, "Extensional vibrations of elastic plates," *Journal of Applied Mechanics,* vol. 26, pp. 561-569, 1959.

[44] D. C. Gazis, "Exact analysis of the plane-strain vibrations of thick-walled hollow cylinders," *Journal of the Acoustical Society of America,* vol. 30, pp. 786-794, 1958.

[45] D. C. Worlton, "Experimental confirmation of Lamb waves at megacycle frequencies," *Journal of Applied Physics,* vol. 32, pp. 967-971, 1961.

[46] I. A. Viktorov, *Rayleigh and Lamb Wave-Physical Theory and Applications*. New York: Plenum, 1967.

[47] W. Ostachowicz, P. Kudela, P. Malinowski, and T. Wandowski, "Damage localisation in plate-like structures based on PZT sensors," *Mechanical Systems and Signal Processing,* vol. 23, pp. 1805-1829, Aug 2009.

[48] R. S. C. Monkhouse, P. Wilcox, and P. Cawley, "Flexible interdigital PVDF transducers for the generation of Lamb waves in structures," *Ultrasonics,* vol. 35, pp. 489-498, 1997.

[49] S. Park, C.-B. Yun, Y. Roh, and J.-J. Lee, "PZT-based active damage detection techniques for steel bridge components," *Smart Materials and Structures,* vol. 15, pp. 957-966, 2006.

[50] S. S. Kessler, S. M. Spearing, and C. Soutis, "Damage detection in composite materials using Lamb wave methods," *Smart Materials and Structures,* vol. 11, pp. 269-278, 2002.

[51] S. Ha and F. K. Chang, "Optimizing a spectral element for modeling PZT-induced Lamb wave propagation in thin plates," *Smart Materials and Structures,* vol. 19, Jan 2010.

[52] S. B. Kim and H. Sohn, "Instantaneous reference-free crack detection based on polarization characteristics of piezoelectric materials," *Smart Materials and Structures,* vol. 16, pp. 2375-2387, 2007.

[53] S. Ha, K. Lonkar, A. Mittal, and F. K. Chang, "Adhesive layer effects on PZT-induced Lamb waves at elevated temperatures," *Structural Health Monitoring-an International Journal,* vol. 9, pp. 247-256, May 2010.

[54] H. Sohn and S. J. Lee, "Lamb wave tuning curve calibration for surface-bonded piezoelectric transducers," *Smart Materials and Structures,* vol. 19, Jan 2010.

[55] I. C. Smith and S. V. Hoa, "Utilization of PVDF sensors to determine impact damage in graphite/epoxy plates by acousto-ultrasonic technique," *Journal of Reinforced Plastics and Composites,* vol. 13, pp. 111-127, 1994.

[56] B. Lin and V. Giurgiutiu, "Modeling and testing of PZT and PVDF piezoelectric wafer active sensors," *Smart Materials and Structures,* vol. 15, pp. 1085-1093, 2006.

[57] I. G. Kim, H. Y. Lee, and J. W. Kim, "Impact damage detection in composite laminates using PVDF and PZT sensor signals," *Journal of Intelligent Material Systems and Structures,* vol. 16, pp. 1007-1013, Nov-Dec 2005.

[58] R. A. Badcock and E. A. Birt, "The use of 0-3 piezocomposite embedded Lamb wave sensors for detection of damage in advanced fibre composites," *Smart Materials and Structures,* vol. 9, pp. 291-297, Jun 2000.

[59] W. K. Wilkie, R. G. Bryant, J. W. High, R. L. Fox, R. F. Hellbaum, J. A. Jalink, B. D. Little, and P. H. Mirick, "Low-cost piezocomposite actuator for structural control applications," in *Smart Structures and Materials 2000: Industrial and Commercial Applications of Smart Structures Technologies,* Newport Beach, CA, USA, 2000, pp. 323-334.

[60] F. L. D. Scalea, H. Matt, I. Bartoli, S. Coccia, G. Park, and C. Farrar, "Health monitoring of UAV wing skin-to-spar joints using guided waves and macro fiber composite transducers," *Journal of Intelligent Material Systems and Structures,* vol. 18, pp. 373-388, 2007.

[61] B. Culshaw, S. G. Pierce, and W. J. Staszekski, "Condition monitoring in composite materials: an integrated systems approach," *Proceedings of the Institution of Mechanical Engineers, Part I: Journal of Systems and Control Engineering,* vol. 212, pp. 189–202, 1998.

[62] N. Takeda, Y. Okabe, J. Kuwahara, S. Kojima, and T. Ogisu, "Development of smart composite structures with small-diameter fiber Bragg grating sensors for damage detection: Quantitative evaluation of delamination length in CFRP laminates using Lamb wave sensing," *Composites Science and Technology,* vol. 65, pp. 2575-2587, 2005.

[63] D. C. Betz, G. Thursby, B. Culshaw, and W. J. Staszewski, "Structural damage location with fiber Bragg grating rosettes and Lamb waves," *Structural Health Monitoring: An International Journal,* vol. 6, pp. 299-308, 2007.

[64] D. C. Betz, G. Thursby, B. Culshaw, and W. J. Staszewski, "Acousto-ultrasonic sensing using fiber Bragg gratings," *Smart Materials and Structures.,* vol. 12, pp. 122-128, 2003.

[65] Z. Su and L. Ye, "An intelligent signal processing and pattern recognition technique for defect identification using an active sensor network," *Smart Materials and Structures,* vol. 13, pp. 957-969, 2004.

[66] X. P. Qing, S. J. Beard, A. Kumar, T. K. Ooi, and F.-K. Chang, "Built-in sensor network for structural health monitoring of composite structure," *Journal of Intelligent Material Systems and Structures,* vol. 18, pp. 39-49, 2007.

[67] M. Lin and F.-K. Chang, "The manufacture of composite structures with a built-in network of piezoceramics," *Composites Science and Technology,* vol. 62, pp. 919-939, 2002.

[68] X. Qing, A. Kumar, C. Zhang, I. F. Gonzalez, G. Guo, and F.-K. Chang, "A hybrid piezoelectric/fiber optic diagnostic system for structural health monitoring," *Smart Materials and Structures,* vol. 14, pp. 98-103, 2005.

[69] Z. Wu, X. P. Qing, K. Ghosh, V. Karbhar, and F.-K. Chang, "Health monitoring of bonded composite repair in bridge rehabilitation," *Smart Materials and Structures,* vol. 17, 2008.

[70] Z. Su, X. Wang, Z. Chen, L. Ye, and D. Wang, "A built-in active sensor network for health monitoring of composite structures," *Smart Materials and Structures,* vol. 15, pp. 1939-1949, 2006.

[71] P. T. Coverley and W. J. Staszewski, "Impact damage location in composite structures using optimized sensor triangulation procedure," *Smart Materials and Structures,* vol. 12, pp. 795-803, 2003.

[72] H. G. Chen, Y. J. Yan, W. H. Chen, J. S. Jiang, L. Yu, and Z. Y. Wu, "Early damage detection in composite wingbox structures using Hilbert-Huang transform and genetic algorithm," *Structural Health Monitoring-an International Journal,* vol. 6, pp. 281-297, 2007.

[73] N. E. Huang, Z. Shen, S. R. Long, M. L. C. Wu, H. H. Shih, Q. N. Zheng, N. C. Yen, C. C. Tung, and H. H. Liu, "The empirical mode decomposition and the Hilbert spectrum for nonlinear and non-stationary time series analysis," *Proceedings of the Royal Society of London Series a-Mathematical Physical and Engineering Sciences,* vol. 454, pp. 903-995, Mar 8 1998.

[74] B. Boashash, *Time-Frequency Signal Analysis, Methods and Applications*. Melbourne: Longman Cheshire Press, 1992.

[75] J.-B. Ihn and F.-K. Chang, "Pitch-catch active sensing methods in structural health monitoring for aircraft structures," *Structural Health Monitoring-an International Journal,* vol. 7, pp. 5-19, 2008.

[76] C. K. Chui, *Wavelets: a Mathematical Tool for Signal Processing*. Philadelphia: Society for Industrial and Applied Mathematics, 1997.

[77] Z. Su, L. Ye, and X. Bu, "A damage identification technique for CF/EP composite laminates using distributed piezoelectric transducers," *Composite Structures,* vol. 57, pp. 465-471, 2002.

[78] H. Sohn, G. Park, J. R. Wait, N. P. Limback, and C. R. Farrar, "Wavelet-based active sensing for delamination detection in composite structures," *Smart Materials and Structures,* vol. 13, pp. 153-160, Feb 2004.

[79] C. A. Paget, S. Grondel, K. Levin, and C. Delebarre, "Damage assessment in composites by Lamb waves and wavelet coefficients," *Smart Materials and Structures,* vol. 12, pp. 393-402, 2003.

[80] J. C. P. McKeon and M. K. Hinders, "Parallel projection and crosshole Lamb wave contact scanning tomography," *Journal of the Acoustical Society of America,* vol. 106, pp. 2568-2577, 1999.

[81] E. V. Malyarenko and M. K. Hinders, "Fan beam and double crosshole Lamb wave tomography for mapping flaws in aging aircraft structures," *Journal of the Acoustical Society of America,* vol. 108, pp. 1631-1639, Oct 2000.

[82] K. R. Leonard, E. V. Malyarenko, and M. K. Hinders, "Ultrasonic Lamb wave tomography," *Inverse Problems,* vol. 18, pp. 1795-1808, 2002.

[83] J. E. Michaels, "Detection, localization and characterization of damage in plates with an in situ array of spatially distributed ultrasonic sensors," *Smart Materials and Structures,* vol. 17, Jun 2008.

[84] J. E. Michaels and T. E. Michaels, "Guided wave signal processing and image fusion for in situ damage localization in plates," *Wave Motion,* vol. 44, pp. 482-492, 2007.

[85] C. H. Wang, J. T. Rose, and F.-K. Chang, "A synthetic time-reversal imaging method for structural health monitoring," *Smart Materials and Structures,* vol. 13, pp. 415-423, 2004.

[86] G. Konstantinidis, B. W. Drinkwater, and P. D. Wilcox, "The temperature stability of guided wave structural health monitoring systems," *Smart Materials and Structures,* vol. 15, pp. 967-976, 2006.

[87] Z. Q. Su, X. M. Wang, L. Cheng, L. Yu, and Z. P. Chen, "On selection of data fusion schemes for structural damage evaluation," *Structural Health Monitoring-an International Journal,* vol. 8, pp. 223-241, May 2009.

[88] Z. Q. Su, L. Cheng, X. M. Wang, L. Yu, and C. Zhou, "Predicting delamination of composite laminates using an imaging approach," *Smart Materials and Structures,* vol. 18, Jul 2009.

[89] F. Yan, R. L. Royer, and J. L. Rose, "Ultrasonic guided wave imaging techniques in structural health monitoring," *Journal of Intelligent Material Systems and Structures,* vol. 21, pp. 377-384, Feb 2010.

[90] X. L. Zhao, H. D. Gao, G. F. Zhang, B. Ayhan, F. Yan, C. Kwan, and J. L. Rose, "Active health monitoring of an aircraft wing with embedded piezoelectric sensor/actuator network: I. Defect detection, localization and growth monitoring," *Smart Materials and Structures,* vol. 16, pp. 1208-1217, Aug 2007.

[91] T. R. Hay, R. L. Royer, H. Gao, X. Zhao, and J. L. Rose, "A comparison of embedded sensor Lamb wave ultrasonic tomography approaches for material loss detection," *Smart Materials and Structures,* vol. 15, pp. 946-951, 2006.

[92] D. Wang, L. Ye, Y. Lu, and Z. Q. Su, "Probability of the presence of damage estimated from an active sensor network in a composite panel of multiple stiffeners," *Composites Science and Technology,* vol. 69, pp. 2054-2063, Oct 2009.

[93] V. Giurgiutiu and J. Bao, "Embedded-ultrasonics structural radar for in situ structural health monitoring of thin-wall structures," *Structural Health Monitoring-an International Journal,* vol. 3, pp. 121-140, 2004.

[94] S. Sundararaman, D. E. Adams, and E. J. Rigas, "Structural damage identification in homogeneous and heterogeneous structures using beamforming," *Structural Health Monitoring-an International Journal,* vol. 4, pp. 171-190, 2005.

[95] V. Giurgiutiu, J. Bao, and W. Zhao, "Piezoelectric wafer active sensor embedded ultrasonics in beams and plates," *Experimental Mechanics,* vol. 43,

pp. 428-449, 2003.

[96] C.-H. Nguyen, S. Pietrzko, and R. Buetikofer, "The influence of temperature and bonding thickness on the actuation of a cantilever beam by PZT patches," *Smart Materials and Structures,* vol. 13, pp. 851-860, 2004.

[97] M. J. S. Lowe, P. Cawley, J. Y. Kao, and O. Diligent, "The low frequency reflection characteristics of the fundamental antisymmetric Lamb wave A_0 from a rectangular notch in a plate," *Journal of the Acoustical Society of America,* vol. 112, pp. 2612-2622, Dec 2002.

[98] M. J. S. Lowe and O. Diligent, "Low-frequency reflection characteristics of the S_0 Lamb wave from a rectangular notch in a plate," *Journal of the Acoustical Society of America,* vol. 111, pp. 64-74, 2002.

[99] P. S. Tua, S. T. Quek, and Q. Wang, "Detection of cracks in plates using piezo-actuated Lamb waves," *Smart Materials and Structures,* vol. 13, pp. 643-660, 2004.

[100] Y. Lu, L. Ye, Z. Su, and N. Huang, "Quantitative evaluation of crack orientation in aluminium plates based on Lamb waves," *Smart Materials and Structures,* vol. 16, pp. 1907-1914, 2007.

[101] Z. Su and L. Ye, "Lamb wave propagation-based damage identification for quasi-isotropic CF/EP composite laminates using artificial neural algorithm, Part II: implementation and validation," *Journal of Intelligent Material Systems and Structures,* vol. 16, pp. 113-125, 2005.

[102] D. J. Inman, C. R. Farrar, V. L. Junior, and V. S. Junior, *Damage Prognosis: for Aerospace, Civil and Mechanical Systems* Chichester: John Wiley & Sons, 2005.

[103] Z. Su and L. Ye, *Identification of Damage Using Lamb Waves: From Fundamentals to Applications*. London: Springer-Verlag GmbH & Co., 2009.

[104] A. Raghavan and C. E. S. Cesnik, "Effects of elevated temperature on guided-wave structural health monitoring," *Journal of Intelligent Material Systems and Structures,* vol. 19, pp. 1383-1398, Dec 2008.

[105] H. W. Park, H. Sohn, K. H. Law, and C. R. Farrar, "Time reversal active sensing for health monitoring of a composite plate," *Journal of Sound and Vibration,* vol. 302, pp. 50-66, 2007.

[106] J. P. Jiao, B. W. Drinkwater, S. A. Neild, and P. D. Wilcox, "Low-frequency vibration modulation of guided waves to image nonlinear scatterers for structural health monitoring," *Smart Materials and Structures,* vol. 18, Jun 2009.